FERMI SURFACE STUDIES OF ALUMINUM AND DILUTE ALUMINUM-MAGNESIUM ALLOYS USING THE MAGNETOTHERMAL OSCILLATION TECHNIQUE

Thesis for the Degree of Ph. D. MICHIGAN STATE UNIVERSITY JOHN C. ABELE 1968 in**£619**

This is to certify that the

thesis entitled

FERMI SURFACE STUDIES OF ALUMINUM

AND DILUTE ALUMINUM - MAGNESIUM ALLOYS

USING THE MAGNETOTHERMAL OSCILLATION TECHNIQUE

presented by

John C. Abele

has been accepted towards fulfillment of the requirements for

Ph.D. degree in Physics

Van. 1 / Aller

Date ______/ 14,__ /

O-169

ABSTRACT

FERMI SURFACE STUDIES OF ALUMINUM AND DILUTE ALUMINUM - MAGNESIUM ALLOYS USING THE MAGNETOTHERMAL OSCILLATION TECHNIQUE

by John C. Abele

The third zone Fermi surface of aluminum and dilute aluminum - magnesium alloys has been measured using the magnetothermal oscillation (MTO) technique. Measurements for pure aluminum are found to be in good agreement with the results of Gunnerson, Gordon, Bohm and Vol'skii. These results can all be interpreted on the basis of a pseudopotential model due to Ashcroft.

For aluminum alloys with up to 0.4 at.% magnesium the extremal cross-sectional areas of the Fermi surface were found to decrease by as much as 10%. This effect can be accounted for by a simple rigid band valence model.

The so-called Dingle temperatures, which represent the collision broadening of the Landau levels, have also been measured for the alloys. A comparison is made of the lifetimes calculated from the Dingle temperatures (via A.D. Brailsford's theory) with those obtained from the electrical resistivity.

FERMI SURFACE STUDIES OF ALUMINUM AND DILUTE ALUMINUM - MAGNESIUM ALLOYS USING THE MAGNETOTHERMAL OSCILLATION TECHNIQUE

Ву

John C. Abele

A THESIS

Submitted to
Michigan State University
in partial fulfillment of the requirements
for the degree of

DOCTOR OF PHILOSOPHY

Department of Physics

G 51414

ACKNOWLEDGMENTS

I am indebted to Professor Frank J. Blatt who provided both guidance and encouragement during the course of this research.

Support from the National Science Foundation, the National Aeronautics and Space Administration, and the Michigan Institute of Science and Technology is also gratefully acknowledged.

TABLE OF CONTENTS

	F	age
ACKNOWLEDG	MENTS	ii
LIST OF TA	BLES	v
LIST OF FI	GURES	vi
LIST OF AP	PENDICES	ix
CHAPTER I	INTRODUCTION TO FERMI SURFACE STUDIES	1
	1.1 Introduction	1
	1.2 The Worth of Fermi Surface Measurements	1
	1.3 Experimental Fermi Surface Studies .	2
	1.4 Theoretical Methods for Determining the Fermi Surface	6
	1.5 Comparison of Theory and Experiment	8
CHAPTER II	THE THEORY OF OSCILLATORY QUANTUM EFFECTS	10
	2.1 Introduction	10
	2.2 History of Landau Diamagnetism	10
	2.3 Lifshitz - Onsager Theory	12
	2.4 The General Result	15
CHAPTER II	I THERMODYNAMIC ANALYSIS OF THE MAGNETO- THERMAL EXPERIMENT	19
	3.1 Introduction and Working Hypothesis.	19
	3.2 Thermodynamic Calculation	20

CUADTED	T17	THE EVDEDIMENTAL ADDANGEMENT LICED	Page
CHAPTER	10	THE EXPERIMENTAL ARRANGEMENT USED TO STUDY MTO	28
		4.1 Introduction	28
		4.2 The Experimental Cryostat	28
		4.3 The Measurements of Small Diff- erential Temperatures	33
		4.4 Magnetic Field Measurement	40
		4.5 Field Sweep Techniques	41
		4.6 Data Acquisition and Reduction.	47
CHAPTER	V	SAMPLE PREPARATION	58
		5.1 Introduction	58
		5.2 Necessary Precautions	58
		5.3 Crystal Growth	59
		5.4 Resultant Crystals	65
CHAPTER	VI	THE FERMI SURFACE OF PURE ALUMINUM.	69
		6.1 Introduction	69
		6.2 Existing Fermi Surface Models and Data	69
CHAPTER	VII	EXPERIMENTAL RESULTS FOR AL-MG ALLOYS	75
		7.1 Introduction	7 5
		7.2 Changes in the Aluminum Fermi Surface Induced by Alloying	76
		7.3 Amplitude Dependence	81
		7.4 Amplitude Comparisons	94
CHAPTER	VIII	GENERAL CONCLUSIONS	98
BIBLIOGR	APHY		102

LIST OF TABLES

Table	Page
5.1 Sample Information	68
7.1 Dingle Temperature Results	87
7.2 Scattering Results	92
7.3 Amplitude Comparison	98

LIST OF FIGURES

Figu	re	Page
2.1	Landau Levels and the Fermi Surface	14
3.1	Thermodynamic System	19
4.1	Vacuum System	29
4.2	Rotatable Sample Holder	32
4.3	Temperature Dependence of Resistance of Carbon Resistors	35
4.4	Thermal Bridge and Associated Electronics	37
4.5	D.C. Equivalent Circuit	39
4.6	Single Amplifier Sweep Control	42
4.7	Manual Integrator Sweep Control	42
4.8	Automated Sweep Control	44
4.9	Dependence of $\mathcal{T}_{\mathbf{Q}}$ upon Magnetic Field	50
4.10	Hyperbolic Dependence of MTO and dHvA Amplitudes upon T/H	52
4.11	Steady Field Rotational Techniques	55
4.12	Field Modulation Electronics	57
5.1	Aluminum-Magnesium Phase Diagram	61
5.2	Magnesium Concentration after Single Pass Zone Refining	64
5.3	Sample Mounting	66
6.1	Nearly Free Electron Construction for Aluminum	71

Figu:	re	Page
6.2	Ashcroft's Model for the Third Zone Surface of Aluminum	73
6.3	Comparison of Data with Ashcroft's Model in {110} Plane	74
7.1	Angular Variation of /3 Orbit near (110) in [100] Plane	77
7.2	Variation of β Orbit Area along $\langle 110 \rangle$ with Mg Concentration	7 9
7.3	Variation in \$\beta\$ Orbit Area along \$\langle 100 \rangle\$ with Mg Concentration	80
7.4A	Angular Variation of & Orbits near (110) in the {110} Plane	82
7.4B	Variation in ↑ Orbit Area along ⟨110⟩ with Mg Concentration	83
7.5	Angular Variation of Y Orbits in {100} Plane .	84
7.6	Amplitude Dependence in the {100} Plane	85
7.7	Dingle Plots along (110)	87
7.8	Results of Brailsford's Scattering Calculation	90
7.9	Temperature Dependence of the MTO Amplitude	93
A.1	Extraneous Heating Effects	107
B.1	Crush-Type Lead O-Ring Seal	110
C.1	Differential Thermal Bridge Schematic	112
D.1	Magneto-resistance Probe	114
E.1	Harvey-Wells Electromagnet Field Characteristics	115
F.1	Squaring Circuit for $\frac{1}{H}$ Sweep	117

viii

Figu	re	Page
G.1	Least Squares Program for Finding Frequencies	119
G.2	Least Squares Program for Finding Frequencies, cont	120
G.3	Least Squares Program for Finding Frequencies: Typical Output	121
н.1	Filter Circuits	122
н.2	Example of Application of Narrow Band Filter using 1/H Sweep	123
н.3	Low Frequency Data	124
н.4	High Frequency Data	125

LIST OF APPENDICES

Ap	pendix	Page
A	Heat Input via the Rotating Gear Mechanism .	107
В	Crush-Type Lead O-Ring Seals	110
С	Differential Thermal Bridge Schematic	112
D	Magneto-resistance Probe	113
	Harvey-Wells Electromagnet Field Characteristics	115
F	Squaring Circuit for $\frac{1}{H}$ Sweep	116
G	Least Squares Program for Finding Frequencies	119
Н	Filter Circuits	122

CHAPTER I

INTRODUCTION TO FERMI SURFACE STUDIES

1.1 Introduction

Over the last ten years an enormous amount of effort by both experimental and theoretical solid state physicists has been directed toward the determination of the Fermi surface of a large number of metal and alloy systems. The purpose of this first chapter is to relate some of the reasons for such an extensive study of Fermi surfaces and to summarize the progress, both experimental and theoretical, that has been made. As the nature of Fermi surface measurements is unraveled it will become apparent that the techniques have become diversified as well sophisticated. This is to say that many various types of measurements utilizing different physical phenomena can be used to probe the Fermi surface. On the theoretical side there have been some new ideas but much of the work has been the adaptation of the earlier methods to high speed computer calculations.

1.2 The Worth of Fermi Surface Measurements

The response of metallic elements as well as many other solids to their environment depends in many interesting

cases on the nature of the electron distribution. One way to characterize the distribution is by plotting surfaces of constant energy in a wave number or \underline{k} space. Many of the important properties of the carriers can be related to such surfaces.

(e.g.
$$m_c * = \frac{\hbar^2}{2\pi} \frac{\partial A}{\partial \mathcal{E}}$$
, $v = \frac{1}{\hbar} (\frac{\partial \mathcal{E}}{\partial k}) \dots$)

As the temperature of a Fermi Dirac system is reduced, the low-lying energy states become filled up to some fixed energy $\mathbf{E}_{\mathbf{f}}$ and higher energy states are unfilled. A well known but very important property of such a system is that the usual excitations which result in the transport of energy are largely limited to those states whose energy is very near $\mathbf{E}_{\mathbf{f}}$. Thus the contours of energy in $\underline{\mathbf{k}}$ space having energy near $\mathbf{E}_{\mathbf{f}}$ are of extreme importance to the understanding of electronic processes in solids. The physically interesting parameters such as $\mathbf{m}_{\mathbf{c}}^{\star}$, \mathbf{v} , etc. previously mentioned are to be evaluated at $\mathbf{E}_{\mathbf{f}}$. This then is briefly the motivation for studying the Fermi surface of metals.

1.3 Experimental Fermi Surface Studies

There are many methods for determining Fermi surface parameters. Some of the methods currently in use will be briefly surveyed here and references to much more complete descriptions given.

First, there are the oscillatory effects due to the Landau diamagnetism. These effects fall roughly into two categories: those related to equilibrium phenomena and those which require some kind of additional excitation mechanism (e.g. electric field, thermal gradient, etc.) and are thus non-equilibrium phenomena. Examples of the first type are the deHaas-van Alphen 1-7 magnetothermal oscillations $^{8-10}$. The deHaas-van Alphen measurement, which is perhaps the most common of all the Fermi surface measurements, has undergone quite a series of improvements from the old "point by point" susceptibility balance to the field modulation (i.e. derivative) technique of the present. Those included in the second category are oscillatory electrical resistivity^{11,12} (Shubnikov-deHaas effect), oscillatory thermal resistance, and oscillatory thermopower 13,14. The frequency of the oscillations observed in all of these experiments is proportional to the extremal crosssectional areas of Fermi surface in a plane perpendicular to the applied field H. From the temperature and field dependence of the amplitude of these oscillations one should be able to obtain information about the scattering of the carriers as well as their effective masses. The amplitude measurements are probably more difficult to

interpret in the nonequilibrium phenomena because the amplitude of the one set of oscillations is not independent of other parts of the Fermi surface.

Another important class of experiments is the caliper type measurements using geometric resonances. Among them are the Gantmakher r.f. size effect 16 and ultrasonic attenuation 17-20. Both of the experiments measure the caliper or extremal diameters of the Fermi surface in a plane perpendicular to the applied field H. Since r.f. size effect resonances are produced by the relation between the diameter of the carriers orbits and the width of the sample, the preparation of smooth plane samples is critical. It should in principle be possible to deduce some information about the boundary scattering using this experiment.

Yet another important type of measurement is the cyclotron resonance experiment 21. This is a temporal resonance effect in which conduction electrons pursuing helical paths under the influence of a magnetic field H applied parallel to the surface are intermittently brought into the skin depth of a metal where they are acted upon by the microwave electric field. A resonance can occur when the component of the microwave electric field in the plane of the surface undergoes an integral number of

cycles during the time it takes a carrier to make one orbit. This experiment gives the average value of the effective mass over the electron orbit.

The last class of Fermi surface measurements to be mentioned is magnetoresistance^{22,23}. At low fields it is difficult to separate Fermi surface anisotropies from relaxation time anisotropies. In the high field region the behavior of the magnetoresistance is largely dependent upon existence or non-existence of open orbits. Thus the method can be used as a topological check of proposed Fermi surfaces or to choose between alternative models.

There are other techniques which can be used to shed light on the Fermi surface of a particular material but these are the ones most commonly being used.

In addition to the relatively straight-forward experiments on pure materials, one can try to alter either the band structure or the Fermi energy. The alterations are made in the nature of perturbations of the usual Fermi surface. One possible alteration is to introduce an impurity which can affect the scattering, the electron concentration, or the lattice structure 24,25. Another way to manipulate the surface would be to apply hydrostatic pressure 26,27. One would hope that changes due

to such effects could be accounted for within the framework of the current theories, although sometimes this process is muddled because of the limited amount of knowledge available about the physical changes that accompany alloying.

Much effort (both experimental and theoretical) has been focused on the problem of magnetic breakdown in the last few years 28-30. Magnetic breakdown can give information about the nature of the band gaps in various directions and is an interesting effect on its own but it has not been used as a general tool to probe the Fermi surface.

1.4 Theoretical Methods for Determining the Fermi Surface

At present there exist several methods by which one may calculate the band structure and hence infer the Fermi surface for a given material. The applicability of a given method depends largely upon the type of electronic states the valence electrons occupy. The methods most commonly used are the tight binding method, the cellular method, the augmented plane wave (APW) method, the orthogonalized plane wave (OPW) method, the pseudopotential method and the Green's function method.

The applications of these methods are described very briefly below and references to much more complete

expositions are given.

The tight binding method is best applied to core states and localized outer electrons such as one finds in the transition metals. The cellular method dates back to the work of E. P. Wigner and F. Seitz. The APW method is based upon the cellular method, which assumes a spherical potential inside non-overlapping spheres centered on each lattice point and a constant one outside the spheres^{31,32}. If there is directional bonding the simple APW method will provide unsatisfactory results. There are many materials whose energy bands can be classified as nearly free electron (NFE). Among these materials are the alkali and alkali-earth metals; the simple polyvalent metals Al, Cd, Zn, Mg, etc., as well as semi-metals and semiconductors. For many of these materials a tolerably good approximation to the actual Fermi surface can be obtained by the one OPW or NFE construction of Harrison³³. The accuracy is increased when more OPW's are included, especially near the zone boundaries. The pseudopotential method is based on the OPW method, although it could be based on an APW-type calculation. The OPW method requires that electrons be classified as either core or itinerant electrons. Consequently for materials containing partially-filled d

bands the OPW or OPW-based pseudopotantial cannot be expected to yield a good description. The Green's function method is, like the APW, based on the muffintin crystal potential model³⁴. In the Green's function method the coefficients in the reciprocal lattice vector expansion are specified and coefficients in the atomic orbital expansion are determined variationally, This is just the reverse of the APW method and is useful in that the secular equation is usually much smaller than in the APW method. The similarity between these two methods has been explored by Ziman³⁵. Relativistic corrections become important as the atomic number becomes greater than about 55 to 70.

1.5. Comparison of Theory and Experiment

The Fermi surfaces for the simple metals have by this time been fairly well determined, both experimentally and theoretically. These are the metals whose outer shells contain only s and p type electrons and are thus amenable to OPW or OPW-based pseudopotential methods. Although these methods have a few variable parameters which are adjusted to fit the experimental data the agreement of the angular variation of the extremal cross-sectional areas is remarkable.

The experimental results on the noble metals are

well accounted for by the APW calculations.

The transition metals are of current interest. The problem of obtaining good samples is rapidly being overcome. The computer APW calculations (some relativistic) which can be easily adapted for different materials are producing models which agree well with experiment for both these elements and associated intermetallic compounds.

The rare earths are still relatively unexplored because of their complicated metallurgy 36

In addition to completing measurements of Fermi surfaces the next few years will witness the measurement of the parameters \mathcal{T} and m* and their anisotropy over the Fermi surface. As will be shown later these quantities can be determined from studies of the amplitude variation with temperature and field using the techniques presently available. Such values are not averaged over pieces of Fermi surface but are averaged over only the extremal orbit causing the oscillations. The effect of impurities upon these quantities and upon the Fermi surface itself will also involve much study.

CHAPTER II

THE THEORY OF OSCILLATORY QUANTUM EFFECTS

2.1 Introduction

In this chapter a short historical sketch of Landau diamagnetism is given. This is followed by a brief derivation of the Onsager - Lifshitz relation and a presentation of the formal result of Lifshitz and Kosevitch for the oscillatory free energy. The extensions of this theory as well as some interesting side effects are presented.

2.2 History of Landau Diamagnetism

The oscillatory effects which are periodic in reciprocal applied field have a common historical origin. In Leiden in 1930 W. J. deHaas and P. M. van Alphen^{37,1} first observed the oscillatory behavior of the magnetic susceptibility of a single crystal of bismuth. This effect, which bears their names and will hereafter be referred to as the dHvA effect, was at first thought to be a particular property of bismuth. It had been shown by Bohr³⁸ in 1911 that the diamagnetic susceptibility of a classical free electron gas is zero. Landau³⁹ in 1930 showed that Bohr's result is not valid when one

applies quantum mechanics to the motion of the electrons. By 1939 the early work of D. Shoenberg⁴⁰ had shown that the dHvA effect could provide detailed information about the electron energy spectrum near maxima or minima in the energy bands as well as the number in each part. In a supplement to this article Landau, using the effective mass approximation, enumerated the eigenvalues and eigenfunctions for electrons in a magnetic field which obey a quadratic dispersion relation. Apart from the region around a band edge there is little justification for the use of a quadratic dispersion relation.

By the time that Onsager⁴¹ had related the 1/H periodicity of the dHvA oscillations to the extremal cross-sections of Fermi surface normal to the field direction, the effect had been seen in many materials: Bi, Sb, Mg, Hg, Cd, Zn, Be, C, Ga, In, Sn, Tl, and Al. The central result of the Onsager relation is that even though the energy may be quantized in a complicated manner the orbital areas of the charge carriers in momentum space can be quantized in a simple way. Shortly thereafter, I.M. Lifshitz and A.M. Kosevitch⁴² used the quasiclassical Bohr-Sommerfeld quantization condition to quantize the areas and obtained the grand canonical potential for charged quasi-particles obeying a general

dispersion law $\mathcal{E} = \mathcal{E}(k_x, k_y, k_z)$. This result forms the basis of the presently accepted result.

2.3 Lifshitz - Onsager Theory

Consider the motion of a charged quasi-particle in the state k under the arbitrary dispersion relation

$$\mathcal{E} = \mathcal{E} (k_x, k_y, k_z)$$
 (2.1)

From the Lorentz equation,

$$\frac{\dot{\mathbf{k}}}{\dot{\mathbf{k}}} = \frac{\mathbf{e}}{\dot{\mathbf{h}}} \mathbf{c} \, \underline{\mathbf{v}} \, \mathbf{x} \, \underline{\mathbf{H}} \tag{2.2}$$

it is easily seen that since changes in \underline{k} are normal to \underline{H} , the quasi-particle's k-space trajectory remains in a plane normal to \underline{H} . Since \underline{v} is normal to surfaces of constant energy ($\underline{v} = \frac{1}{h} \nabla_{\underline{k}} \mathcal{E}$) we see that the quasi-particle trajectory in k-space is along the surface of constant energy in a plane normal to \underline{H} . It follows from Eqn. (2.2) that the projection of the real space orbit has the same shape as the k-space orbit though it is scaled by the factor $\frac{ch}{eH}$ and rotated by $\pi/2$.

In a magnetic field the momentum is generalized to

$$\underline{P} = \hbar \underline{k} + \frac{e}{c} \underline{A}$$

It is convenient to direct the magnetic field along the z axis and use the vector potential $\underline{A} = (0, Hx, 0)$.

In this case the Bohr-Sommerfeld quantization relation

$$\oint \underline{P} \cdot \underline{dQ} = (n + \gamma) h, \qquad n = 0, 1, \dots,$$

becomes

$$\frac{\pi^2 c}{eH} \oint k_x dk_y = (n + y)h ,$$

so that the k-space orbit along a line of constant energy encloses an area A normal to the field H and quantized by

$$A(E, k_z) = \frac{2\pi eH}{\pi c} (n + \%) , n = 0,1,2,... (2.3)$$

This is the Onsager result.

Eqn. (2.3) can be inverted to yield $\mathbf{\mathcal{E}} = \mathbf{\mathcal{E}}_n(k_z, H)$. As a simple example consider an ellipsoidal Fermi surface. Cylinders with the allowed cross-sectional area are shown in Fig. (2.1)A. Fig. (2.1)B shows that E is not a constant for a given Landau tube but varies with k_z .

At T=0 the occupied states are those with energy equal to or below the Fermi energy, but the quasiparticles are restricted to orbits with enclosed area given by Eqn. (2.3), the Onsager relation. Thus as H is increased the number of quasi-particles on the outermost cylinder with k \langle k_f must decrease as its area

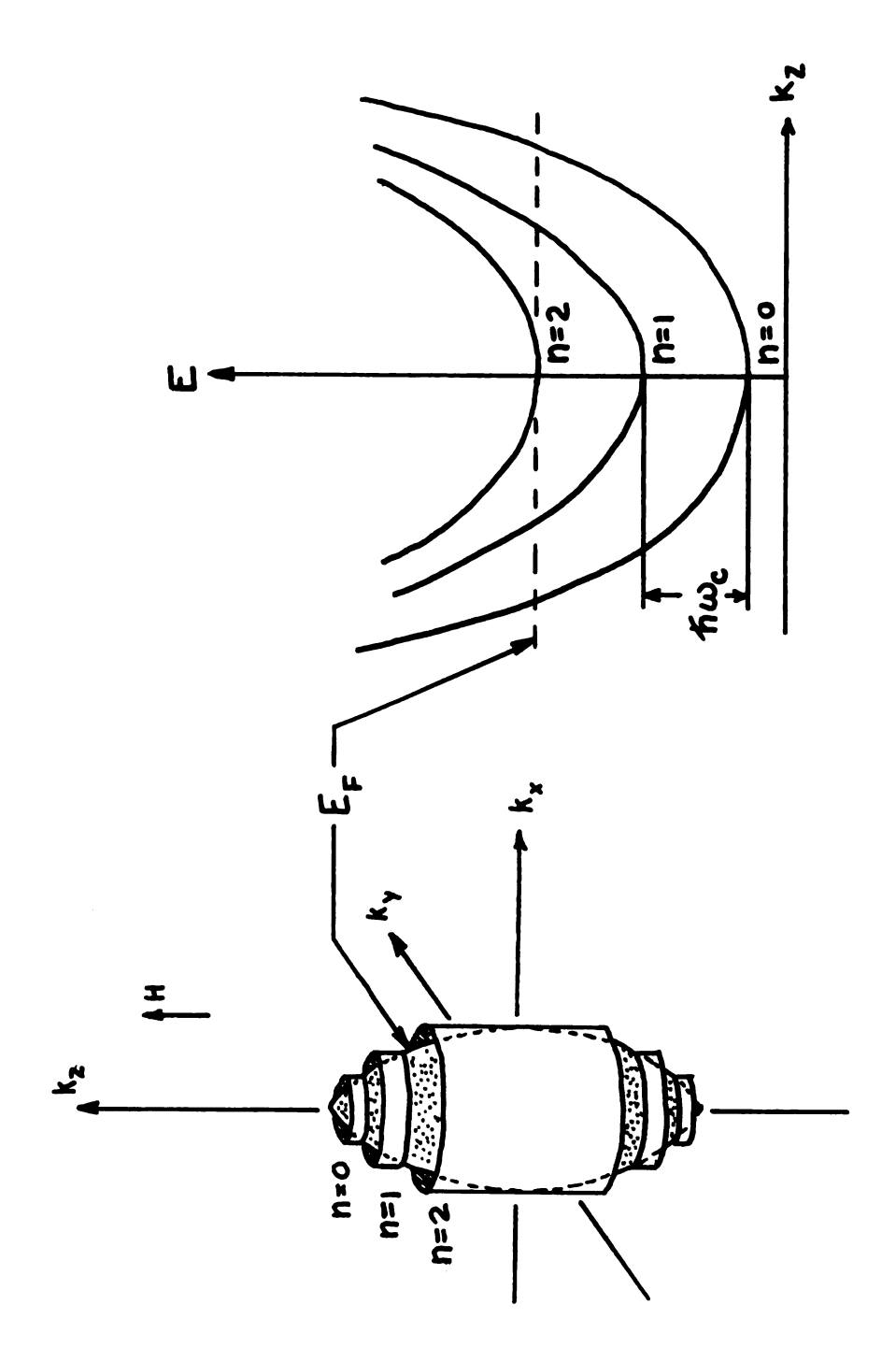


Fig. (2.1) Landau Levels and the Fermi Surface

surpasses that of the Fermi sphere. The degeneracy of the Landau tubes is very high and the density is proportional to the field H. The Fermi energy does depend upon the field but this is a second order effect and of little importance unless one is in a region where only a few quantum levels are left inside the Fermi surface (i.e. the quantum limit). In addition to substantiating these assertions the theory of Lifshitz and Kosevitch shows that by far the major contribution to the oscillatory free energy comes from an extremum in the cross-sectional area of the Fermi surface. One would expect this since in this region a large number of particles must simultaneously make the transition to lower levels.

From Eqn. (2.3) we can infer the frequency of the oscillations. We will bring the j th level up to the Fermi level when H is such that

$$\frac{A_F \hbar c}{2\pi e H} = j + \Upsilon .$$

The oscillations are thus periodic in 1/H with frequency

2.4 The General Result

The result of Lifshitz and Kosevitch for the oscill-

atory part of the free energy is:

$$F_{osc} = \frac{2VkT(\frac{eH}{hc})^{3/2}}{\left|\frac{\partial^{2}A(E_{F},k_{z})}{\partial k_{z}^{2}}\right|^{2/2}} = \frac{1/2}{k=1} \frac{\cos\left(\frac{khc}{eH} A_{ext}(E_{F}) - 2\pi lr - \frac{\pi}{4}\right)}{k^{3/2} \sinh^{2}\frac{\pi^{2}lkT}{\hbar \omega_{c}^{2}}} \times \frac{1}{k^{3/2} \sinh^{2}\frac{\pi^{2}lkT}{\hbar \omega_{c}^{2}}}$$

$$\frac{\ell \pi \, gm_c^*}{2m_c} \quad e^{-\frac{\pi \ell}{w_c^* \tau}} \tag{2.4}$$

where V = volume

k = Boltzmann's constant

T = absolute temperature in OK

m*= cyclotron effective mass =
$$\frac{\hbar^2}{2\pi} \frac{\partial A}{\partial \xi} \Big|_{E_{f},ext}$$

$$\omega_c *= \frac{eH}{m^*c}$$

phase constant, = 1/2 for quadratic dispersion relation

g = spectroscopic spin splitting factor

 τ = lifetime of a state on the extremal crosssection of Fermi surface following Brailsford (τ = 2 $\tau_{\rm Dingle}$) For Eqn. (2.4) to be valid it is sufficient that $\omega_c * h \ \ \, \&E_F, \ \, kT \ \, \&E_F, \ \, and \ \, f/H \ \, >> \ \, 1.$

The e^{- π l/ ω c* τ} term in Eqn. (2.4) accounts for collision broadening and was derived for lifetime independent of energy and k_z , for particles having quadratic dispersion relation by Dingle⁴³. This calculation has since been generalized by Williamson⁴⁴ for an arbitrary dispersion relation and by Brailsford⁴⁵ for arbitrary Landau level line shape.

The $\cos\frac{\ell\pi\,\mathrm{gm}_{c}^{\star}}{2m_{o}}$ term⁴⁶, modified for arbitrary g value⁴⁷, is due to the spin of the particles. From this term we can see that when $\mathrm{gm}_{c}^{\star}/\mathrm{m}_{o}=1,3,5...$, the amplitude of the fundamental frequency will be zero. Since $\mathrm{m}_{c}^{\star}/\mathrm{m}_{o}$ can be determined from the temperature dependence of the amplitude, anisotropic values of g can be determined. Several workers have noted departures from g = 2 of as much as 30% ⁴⁸.

The effective mass m_c* used in the Lifshitz and Kosevitch calculation has been shown to be enhanced by the electron-phonon and electron-electron interactions $^{49-51}$. A calculation of such an enhancement has been discussed by Harrison in the pseudopotential formalism 33 .

Eqn. (2.4) does not take account of magnetic breakdown effects since they are greatly dependent upon the band structure of a given material. The result also does not include the additional harmonic dependence seen in the so-called B-H effect. This effect has been discussed at length by Pippard⁵², Shoenberg⁵³, and Condon⁵⁴.

CHAPTER III

THERMODYNAMIC ANALYSIS OF THE MAGNETOTHERMAL EXPERIMENT

3.1 Introduction and Working Hypothesis

In this chapter the formal result of Lifshitz and Kosevitch for the oscillatory free energy is used to gain an expression for the oscillatory temperature of a single crystal. The calculation is made for the simplified but practical system seen in Fig. (3.1).

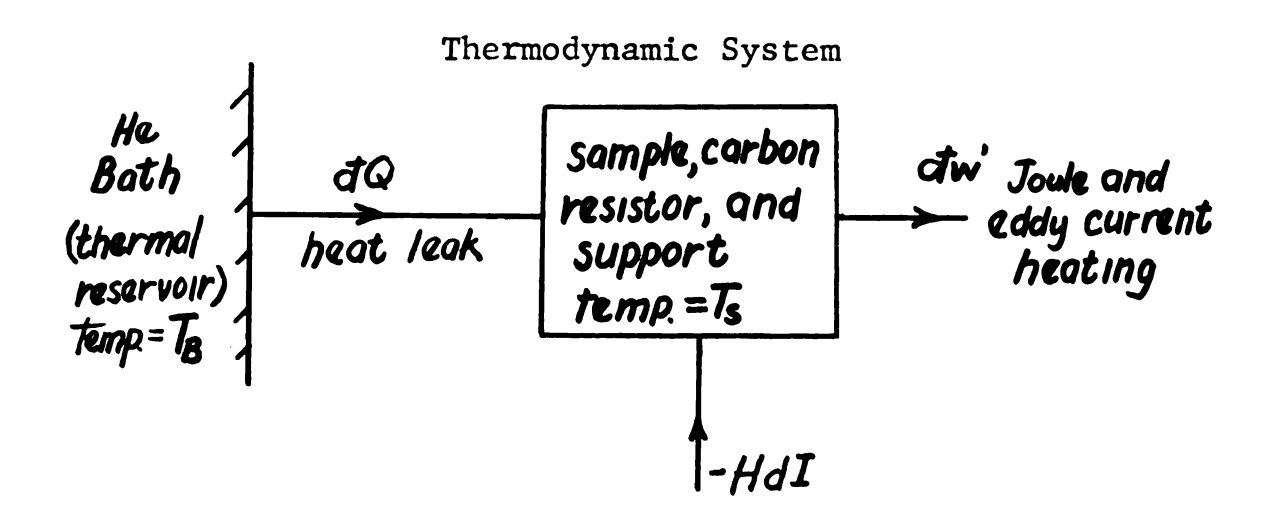


Fig. (3.1)

In this calculation the specific heat of the carbon resistor mounted on the sample, together with that of the associated wire and graphite support, is added to the specific heat of the sample. It is also assumed that

changes in the sample temperature are small relative to the average sample temperature.

Due to the power dissipation in the sample resistor and eddy current heating arising from changing the magnetic field strength, the temperature of an adiabatically isolated sample will gradually increase without bound. A thermal contact or heat leak with conductivity K and exponential time constant $\tau_{\rm e} = \frac{\rm C_{HL}}{\rm K~A}$ is thus necessary to maintain the average sample temperature constant. The effect of this heat leak has also been included in the analysis.

3.2 Thermodynamic Calculation

For a magnetic system the first law of thermodynamics

$$dQ = dU + dW$$

becomes

$$dQ = dU + dW' - HdI$$
 (3.1)

By analogy with the chemical system one replaces P by -H, and V by I.

Considering U = U(H,T) and I = I(U,T) we have $dU = \frac{\partial U}{\partial H} \Big|_{T} dH + \frac{\partial U}{\partial T} \Big|_{H} dT$

and

$$dI = \frac{\partial I}{\partial T})_{H} dT + \frac{\partial I}{\partial H})_{T} dH \qquad (3.2)$$

For this system the "energy equation"

$$\left(\frac{\partial V}{\partial U}\right)^{T} = T \left(\frac{\partial T}{\partial P}\right)^{\Lambda} - B$$

becomes

$$\frac{\partial \mathbf{I}}{\partial \mathbf{U}})^{\mathbf{I}} = -\mathbf{I} \frac{\partial \mathbf{I}}{\partial \mathbf{H}})^{\mathbf{I}} + \mathbf{H}$$

Multiplying both sides by $\frac{\partial I}{\partial H}$)_T we have

$$\frac{\partial \mathbf{I}}{\partial \mathbf{I}})_{\mathbf{T}} \frac{\partial \mathbf{I}}{\partial \mathbf{H}})_{\mathbf{T}} = -\mathbf{T} \frac{\mathbf{J}}{\partial \mathbf{H}})_{\mathbf{I}} \frac{\partial \mathbf{I}}{\partial \mathbf{H}})_{\mathbf{T}} + \mathbf{H} \frac{\partial \mathbf{I}}{\partial \mathbf{H}})_{\mathbf{T}}$$
(3.3)

Applying

$$\frac{\partial X}{\partial X})_{Z} \frac{\partial Z}{\partial Y})_{X} \frac{\partial Z}{\partial Z})_{Y} = -1$$

to the first term on the right side of (3.3) we have

$$\frac{\partial U}{\partial H})_{T} = +T \frac{\partial I}{\partial T})_{H} + H \frac{\partial I}{\partial H})_{T}$$
 (3.4)

Upon substitution of Eqns. (3.2) into (3.1) we find,

$$dQ - dW' = \left[\frac{\partial U}{\partial T}\right]_{H} - H \left[\frac{\partial I}{\partial T}\right]_{H} dT + \left[\frac{\partial U}{\partial H}\right]_{T} - H \left[\frac{\partial I}{\partial H}\right]_{T} dH \quad (3.5)$$

From the modified energy equation, Eqn. (3.4), the second term on the right side of Eqn. (3.5) is obviously

 $T \frac{3I}{H}$, Now

$$C_{P} = \frac{9}{1} \frac{1}{2} C_{P} + P \frac{9}{1} \frac{1}{2} C_{P}$$

so that in this system

$$C_{H} = \frac{\partial U}{\partial I})_{H} - H \frac{\partial I}{\partial I})_{H}$$

With these definitions Eqn. (3.5) becomes

$$dQ-dW' = C_H dT + T \frac{\partial I}{\partial T})_H dH$$

where

đQ is positive for heat flow into the system

dW' is positive for work done by the system dW' has been reserved for joule heating of the carbon resistors, eddy current heating due to sweeping the field or mechanical vibration of the sample relative to the field as indicated in Fig. (3.1). The sources of the temperature difference between the sample and the bath $T_S - T_B$ are the dissipative effects dW' and the Landau diamagnetism.

Now the rate at which heat flows between the bath and the sample is

$$\frac{dQ}{dt} = \dot{Q} = - (T_S - T_B) = - \Delta T = C_H \frac{dT_S}{dt} + T_S \frac{\lambda I}{\lambda T} \frac{dH}{dt} + \frac{dW'}{dt} (3.6)$$
where $\mathcal{K} = \frac{KA}{L}$, and $\Delta T = T_S - T_B$.

In order to continue this calculation one needs an

expression for $\frac{\mathbf{\lambda}I}{\mathbf{\delta}T}$)_H . Using $I = \frac{1}{V} \frac{\mathbf{\delta}F}{\mathbf{\delta}H}$)_T , Eqn. (2.4) is

rewritten in the form,

$$F_{\text{osc}} = VA_{A}TH^{3/2} \frac{\cos(\frac{2\pi f_{A}}{H} + \gamma_{A}) e^{\frac{-b_{A}X_{D}}{H}}}{\sinh b_{A}T/H}$$
(3.7)

where
$$F_{osc} = \sum_{f=1}^{e} F_{osc}^{f}$$

$$A_{f} = \frac{2K(\frac{e}{hc})^{3/2} \cos f \frac{\pi gmc^{*}}{2m_{o}}}{\left|\frac{\partial^{2}A}{\partial Kc^{2}}(E_{F},K_{Z})\right|^{\frac{1}{2}}} \int_{0}^{2\pi} \frac{3}{2} dt$$

$$b_1 = 1.47 \times 10^5 \text{ gauss/}^{\circ} \text{K}$$

$$\varphi = -2\pi l r - \pi/4$$

$$X_D = \pi/2\pi \kappa \tau$$

$$f_{\ell} = \ell \frac{\hbar c}{e} A_{ext}(E_F) = \ell f$$

Thus

$$I_{osc} = \frac{1}{V} \frac{\partial F_{osc}}{\partial H} \Big|_{T} = -\frac{1}{V} \sum_{\theta} \frac{\partial F_{osc}}{\partial H} \Big|_{T} = \sum_{\theta} I_{osc}^{\ell}$$

$$I_{\text{osc}}^{2} = -A_{\ell}T \frac{\partial}{\partial H} \left[\frac{H^{3/2}\cos\left(\frac{2\pi f_{\ell}}{H} + \psi_{\ell}\right) e^{-\frac{bX_{D}}{H}}}{\sinh b_{\ell}T/H} \right].$$

This result may be simplified since for all cases discussed here $\frac{2\pi f_0}{H}$ >>> $b_{\chi}T/H$ and $b_{\chi}X_{\chi}/H$. Thus in taking derivatives the slowly changing exponential can be ignored relative to the trigonometric terms.

Thus

$$I_{\text{OSC}}^{\ell} = -A_{\ell} T \frac{2\pi f_{\ell}}{H^{\frac{1}{2}}} \qquad \frac{\sin(\frac{2\pi f_{\ell}}{H} + \psi_{\ell}) e^{-b_{\ell} X_{\text{D}}/H}}{\sinh b_{\ell} T/H}$$

so that

$$\frac{\partial I_{OS}^{\ell}}{\partial T})_{H} = \frac{-A_{\ell} 2\pi f_{\ell}}{H^{\frac{1}{2}}} \sin(\frac{2\pi f_{\ell}}{H} + f_{\ell}^{0}) e^{-b_{\ell} X_{D}/H}$$
 x

$$\left(\begin{array}{c} \frac{1-b_{f}T/H \operatorname{coth} b_{f}T/H}{\sinh b_{f}T/H} \end{array}\right) \tag{3.8}$$

Thus Eqn. (3.6) becomes

$$- \mathcal{K}\Delta T = C_{H} \frac{d\Delta T}{dt} + T_{S} \frac{\partial I_{osc}}{\partial T})_{H} \frac{dH}{dt} + \frac{dW'}{dt}$$
 (3.9)

where it is assumed that T_B = constant, so

$$\frac{dT_S}{dt} = \frac{d(T_S - T_B)}{dt} = \frac{d\Delta T}{dt} .$$

To solve Eqn. (3.9) in the general case is a difficult problem, but fortunately one can make some well-justified simplifying assumptions. The magnitude of the oscillations is a few millidegrees at most, and a heat leak is used to insure the equilibrium value. Thus $\Delta T/T_S \iff 1 \text{ so that } T_S \rightsquigarrow T_0, \text{ a constant. The separation in field between adjacent peaks at the fundamental (<math>1 = 1$) frequency is at most 5% of the field, so since the dominant terms in Eqn. (3.8) change very slightly

over a few cycles of oscillations, Eqn. (3.9) is solved with the parameter evaluated at some arbitrary field H_0 . One can make the following explicit assumptions for the oscillatory temperature evaluated at mean temperature T_0 and mean field H_0 .

$$H = H_0 + \ll t$$

 $C_{H} = constant$

$$\mathcal{K} = \frac{KA}{L} = constant$$

dw'
dt = -P, a constant and not necessarily zero
since we will use this later to calibrate
the heat leak

$$\frac{2\pi f_{\varrho}}{H} + \varphi_{\varrho}$$
 is expanded as

$$\left(\frac{2\pi f}{H_0(1+\frac{t}{H_0})} + \frac{\varphi}{\ell}\right) \simeq \left[\frac{2\pi f}{H_0} \left(1-\frac{At}{H_0}\right) + \frac{\varphi}{\ell}\right]$$
 (3.10)

(with error $\langle (\frac{\lambda t}{H_0})^2 \rangle$

$$= -(\frac{2\pi f_{\mathcal{I}}}{H_0^2} d_{\mathcal{I}} - \gamma_{\mathcal{I}}') = -(\omega_{\mathcal{I}} - \gamma_{\mathcal{I}}')$$

where

Thus Eqn. (3.9) can be written as

$$C_{H} \frac{d \Delta T}{dt} + \mathcal{K} \Delta T = -\frac{dW'}{dt} - \sum_{\ell=\ell}^{\infty} B_{\ell} \sin(\omega_{\ell} t - Y_{\ell}') \qquad (3.11)$$

where

$$B_{\ell} = \frac{4\pi K_{\ell} (\frac{e}{hc})^{3/2} \cos \frac{\ell \pi g m_{0} *}{2m_{0}}}{\left|\frac{\lambda^{2} A}{\lambda^{2} K_{Z}^{2}}\right|^{\frac{1}{2}} \int_{0}^{3/2} H_{0}^{\frac{1}{2}}} f_{\ell} \propto T_{0} e^{-b_{\ell} \frac{X}{H}}$$

$$(\frac{1-b_{\ell}T_{0}/H_{0} \quad coth \quad b_{\ell}T_{0}/H_{0}}{\sinh b_{\ell}T_{0}/H_{0}})$$

and the other symbols have their previous definitions.

The general solution of Eqn. (3.11) is

$$\Delta T = \frac{P}{R} + Ce^{-\frac{R}{C_H}} + \frac{1}{C_H} \sum_{\ell=1}^{\infty} \frac{B_{\ell}}{\sqrt{(\frac{R}{C_H})^2 + \omega_{\ell}^2}} \times \sin(\omega_{\ell}t - \psi' - \tan^{-1}\frac{C_H \omega_{\ell}}{R})$$

Thus the final expression for the oscillatory temperature dependence (including addenda due to thermal leaks) of a single crystal upon the magnetic field expanded about $T = T_0$ and $H = H_0$ is,

$$T_{S}-T_{B} = \Delta T = \Delta T_{osc}+\Delta T_{P} = -\frac{2K_{B}T_{0}H_{0}^{3/2}(\frac{e}{hc})^{3/2}}{\left|\frac{\lambda^{2}A(E_{F},K_{Z})}{\lambda K_{Z}^{2}}\right|_{ext}^{\frac{1}{2}}}C_{H}$$

$$\frac{\int_{-\infty}^{\infty} \frac{\sin\left[\frac{2\pi f_{\bullet}}{H} - 2\pi \ell r + \frac{\pi}{4} - \tan^{-1}\left(\frac{2\pi T_{\bullet}}{T_{\text{osc}}}\right)\right]}{\sqrt{1 + \left(T_{\text{osc}}/2\pi T_{e}\right)^{2}} \int_{-\infty}^{\infty} \frac{1}{2\pi I_{\bullet}} \cos\left(\frac{\ell r \operatorname{gm}_{e}^{*}}{2m_{o}}\right)}{\sqrt{1 + \left(T_{\text{osc}}/2\pi T_{e}\right)^{2}} \int_{-\infty}^{\infty} \frac{1}{2\pi I_{\bullet}} \cos\left(\frac{\ell r \operatorname{gm}_{e}^{*}}{2m_{o}}\right)}{\sqrt{1 + \left(T_{\text{osc}}/2\pi T_{e}\right)^{2}}} \int_{-\infty}^{\infty} \frac{1}{2\pi I_{\bullet}} \cos\left(\frac{\ell r \operatorname{gm}_{e}^{*}}{2m_{o}}\right)}{\sqrt{1 + \left(T_{\text{osc}}/2\pi T_{e}\right)^{2}}} \cos\left(\frac{\ell r \operatorname{gm}_{e}^{*}}{2m_{o}}\right) \right) \times e^{-it}$$

$$e^{\frac{-b_{\ell}X_{b}}{H}} \left(\frac{1-b_{\ell}T_{0}/H_{0} \coth b_{\ell}T_{0}/H_{0}}{\sinh b_{\ell}T_{0}/H_{0}} \right) + \frac{P}{R} + Ce^{\frac{t}{T_{0}}}$$
(3.12)

where

K_R = Boltzmann's constant

$$f_{\ell} = \int \frac{\hbar c}{e} A_{ext}(E_F)$$

$$b_{\ell} = \frac{2 \pi^2 K_{\rm R} m_{\rm c} * C}{e \hbar} \ell = 1.469 \times 10^5 \frac{m_{\rm c} *}{m_{\rm o}} \text{ gauss/oK}$$

 $au_{ extsf{osc}}$ = period of oscillations

 $\tau_{Q} = C_{H}L/KA = thermal time constant$

 $X_D = Dingle temperature = \pi/2 \pi K_B \tau$

T = lifetime of state on extremal cross-section
 of Fermi surface

 $\Delta T_{\rm osc}$ = oscillatory temperature change due to the Landau diamagnetism

 ΔT_P = temperature change of the sample due to dissipative heating effects

CHAPTER IV

THE EXPERIMENTAL ARRANGEMENT USED TO STUDY MTO

4.1 Introduction

In this chapter the design and operation of the low temperature cryostat used in the present MTO studies is presented and discussed. The techniques necessary for the measurement of small differential temperatures are given. Various methods of data acquisition and the subsequent data reduction techniques for each method are also discussed. The chapter closes with a discussion of some new methods that were tried and suggests further improvements.

4.2 The Experimental Cryostat

There were actually two cryostats designed and built for this study. The second design includes all of the features found in the original cryostat; hence only it will be discussed in any detail.

A schematic of this cryostat and pumping facilities is shown in Fig. (4.1).

The cryostat is a single He^4 bath type. A large mechanical pump, pumping on this bath, provides temperatures down to $1.1^{\circ}\mathrm{K}$. The pressure is regulated by

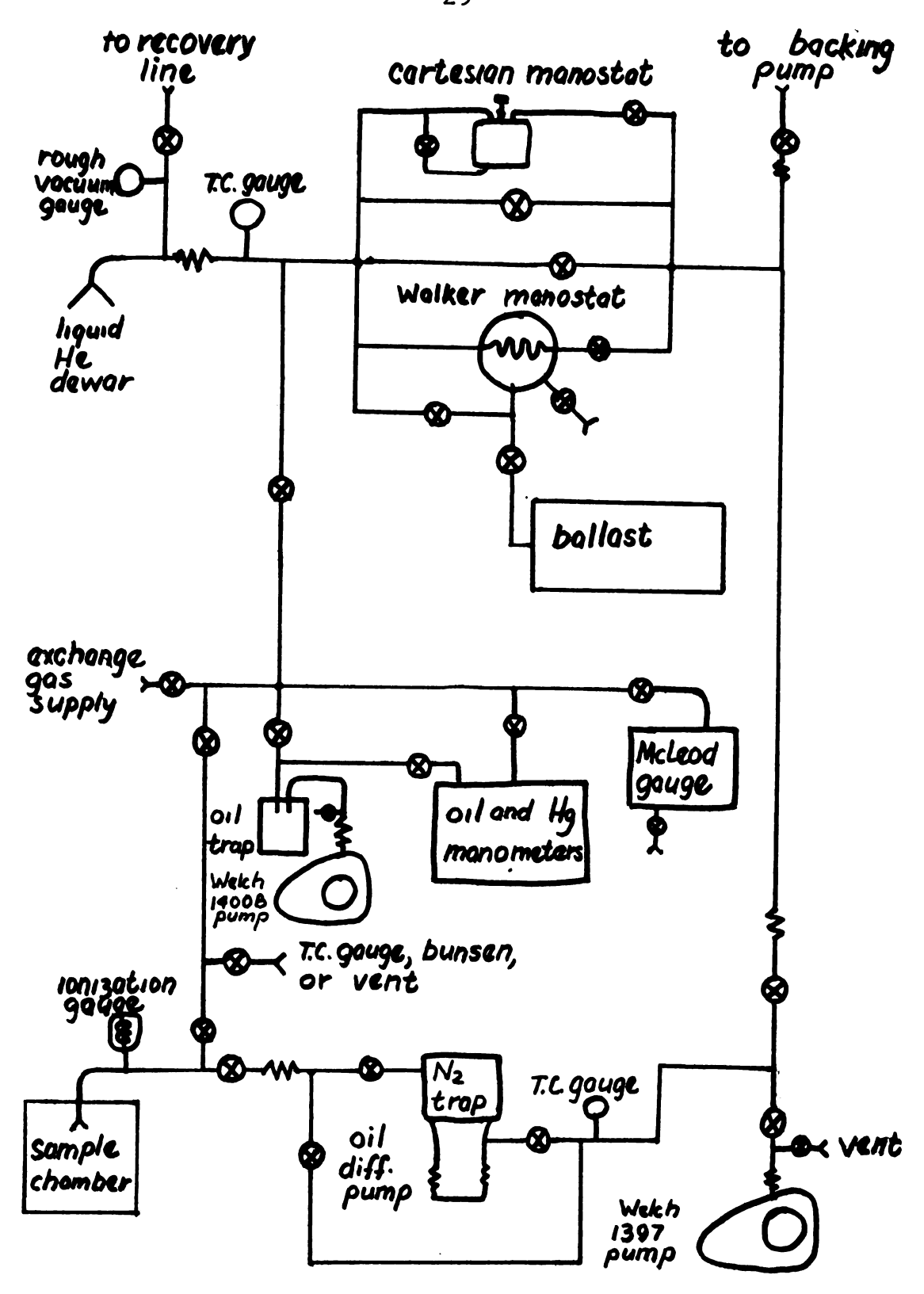


Fig. (4.1) Vacuum System

either a Walker-type condom manostat or a cartesian manostat. The bath pressure is measured by conventional methods using either mercury or oil manometers except for the lowest temperatures where it is determined using a Universal Todd type McLeod gauge. The pressure in this pumping line can also be conveniently read on a U.S. \pm 30 inch vacuum gauge and at low pressures monitored by a thermocouple gauge.

In order to observe the MTO effect it is necessary to have the sample thermally isolated. The degree of isolation necessary depends on the time period of the oscillations. In most cases this requires that the pressure as read on the ionization gauge in the sample vacuum line be $<5 \times 10^{-4} \mathrm{mm}$ Hg. Since fluctuations in this pressure would greatly influence amplitude measurements and are difficult to control, the sample chamber was evacuated to pressures of $<10^{-5}$ mm Hg. A watercooled oil diffusion pump provided this pressure, which was monitored by a Veeco ionization gauge. The watercooled pump was chosen since an air-cooled model was found to introduce vibrations in the cryostat via their common supports.

The second apparatus has a rotatable sample holder.

This holder is rotatable about two mutually perpen-

dicular axes and is pictured in Fig. (4.2).

Because it is difficult, if not impossible, to make a rotary vacuum seal which works reliably at He temperatures, the control rods pass up through the sample chamber vacuum line to a pair of rotary Veeco seals at room temperature. The control rods are made of 3/16 inch diameter stainless steel tubes having a wall thickness of 0.016 inches. Even so, enough heat passed down them to make the sample holder heat up to about 10°K in about a two hour period while the bath remained at 4.20K. The problem was really that these rods passed directly from room temperature to the sample holder which was fairly well isolated from the bath. This was overcome by wrapping a bare #22 Cu wire several times around each rod and bolting it to the brass O-ring flange. In addition, an approximately 8 inch section of Glastic rod is used in place of the stainless tubing near the room temperature flange because it has a much lower thermal conductivity near room temperature.

Because turning the gears in the rotating device produces frictional heating effects (calculation in Appendix A), it was also necessary to solder a pillbox of about 5 cm³ capacity onto the bottom of the sample holder. This is filled through a curled 1/16 inch dia-

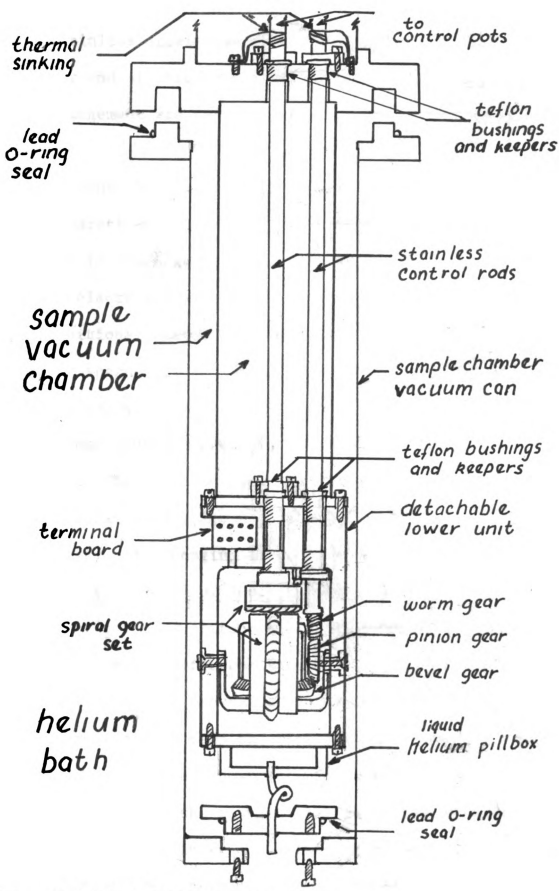


Fig. (4.2) Rotatable Sample Holder

meter stainless steel tube from the helium bath. Near the lower end of this tube a brass flange and lead 0-ring arrangement was used to maintain the sample chamber vacuum.

The general type of 0-ring seal used throughout these apparati was suggested by M. Garber and is briefly discussed in Appendix B.

The electrical leads for the carbon resistors and other additional probes were twisted in pairs, encased in teflon spaghetti, and routed down the sample vacuum line. The leads used are #36 Manganin wire with a nearly temperature independent resistance of about Ω/Ω . These leads, eight in number, are connected to a terminal board a few inches above the sample, facilitating easy changing of carbon resistors, etc.

4.3 The Measurements of Small Differential Temperatures

To study the MTO effect one needs a technique which is able to measure differential temperatures of about 10^{-5} oK relative to a background temperature of 1^{o} K to 4^{o} K. In order not to damp the oscillations, such a sensor must also have a heat capacity which is small relative to that of the sample. A differential thermal bridge utilizing ordinary carbon resistors which satisfies both these criterion is described below.

The use of carbon resistors as thermal sensors has become quite common since their introduction around 1950. The temperature dependence of their resistance is usually fairly well represented by the equations

$$\log_e R = \frac{A}{T} + B$$
 and $\frac{dR}{dT} = \frac{B'e^{A/T}}{T^2}$ (4.1)

Thus as the temperature is reduced the resistance as well as dR/dT increases quite markedly. Plots obtained for the various resistors used in this study are shown in Fig. (4.3). The choosing of resistors for use in a given temperature range will be discussed after the bridge circuit and its sensitivity considerations have been presented.

The resistors to be used are modified in the following fashion. A large number of resistors are glued to a flat metal block and lapped on fine emery paper.

After this is done to both sides of the resistors the metal leads are cut back as far as possible and twisted pairs of #31 Manganin wire are soldered to each resistor. Since two resistors are used in the differential technique it is worthwhile to attempt some matching procedure. In principle one should match the resistors for thermal and magneto-resistance characteristics; however, a simple matching of room temperature resis-

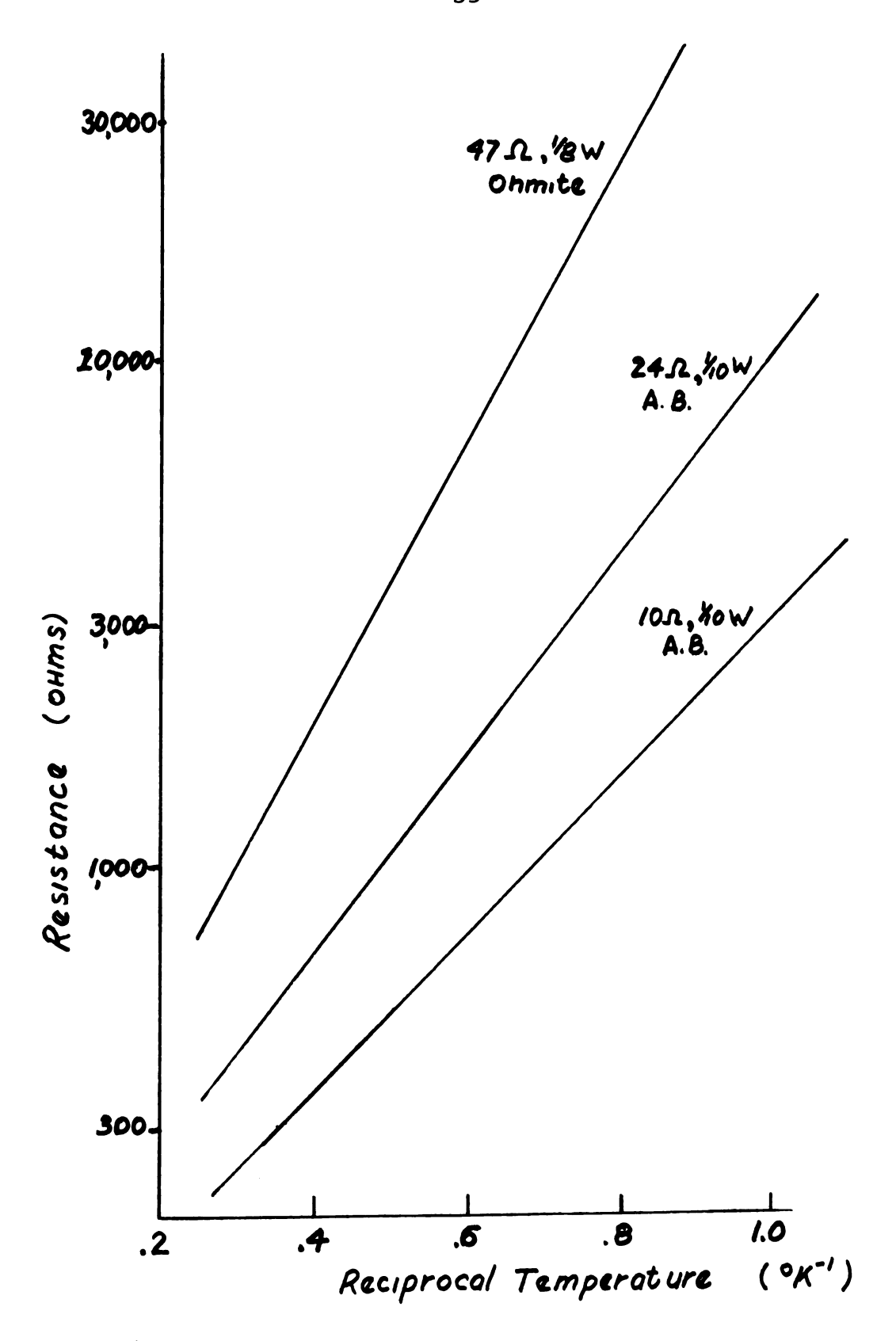


Fig. (4.3) Temperature Dependence of Resistance of Carbon Resistors

tances after grinding has proved satisfactory. Electrical insulation between the resistor and sample is provided by first gluing a small piece of cigarette paper to the sample and then gluing the resistor to this paper. The glue used is G.E. 7031 varnish. The resistors are placed so that they both have the same orientation relative to the magnetic field. After several (5-10) thermal cyclings between 4.2°K and room temperature the resistors tend to become noisy and are replaced. This is probably due to mechanical strains in the resistors as well as degradation of the glue bonds. In addition to having greater thermal conductivity than most glues the G.E. 7031 withstands thermal cycling far better than the more quick-drying varieties such as Duco Cement.

A block diagram of the electronics associated with the differential thermal bridge is shown in Fig. (4.4). The differential bridge with lock-in detection is essentially the same as the method developed by Garber and LePage⁵⁵. The a.c. method is used to reduce the effect of thermal emf's in the leads as well as enabling lock-in detection to be used. The low operating frequency (20 to 60 Hz) of the bridge is chosen so that the capacitive off-balance remains small and can either be balanced out in the bridge or neglected. The lock-

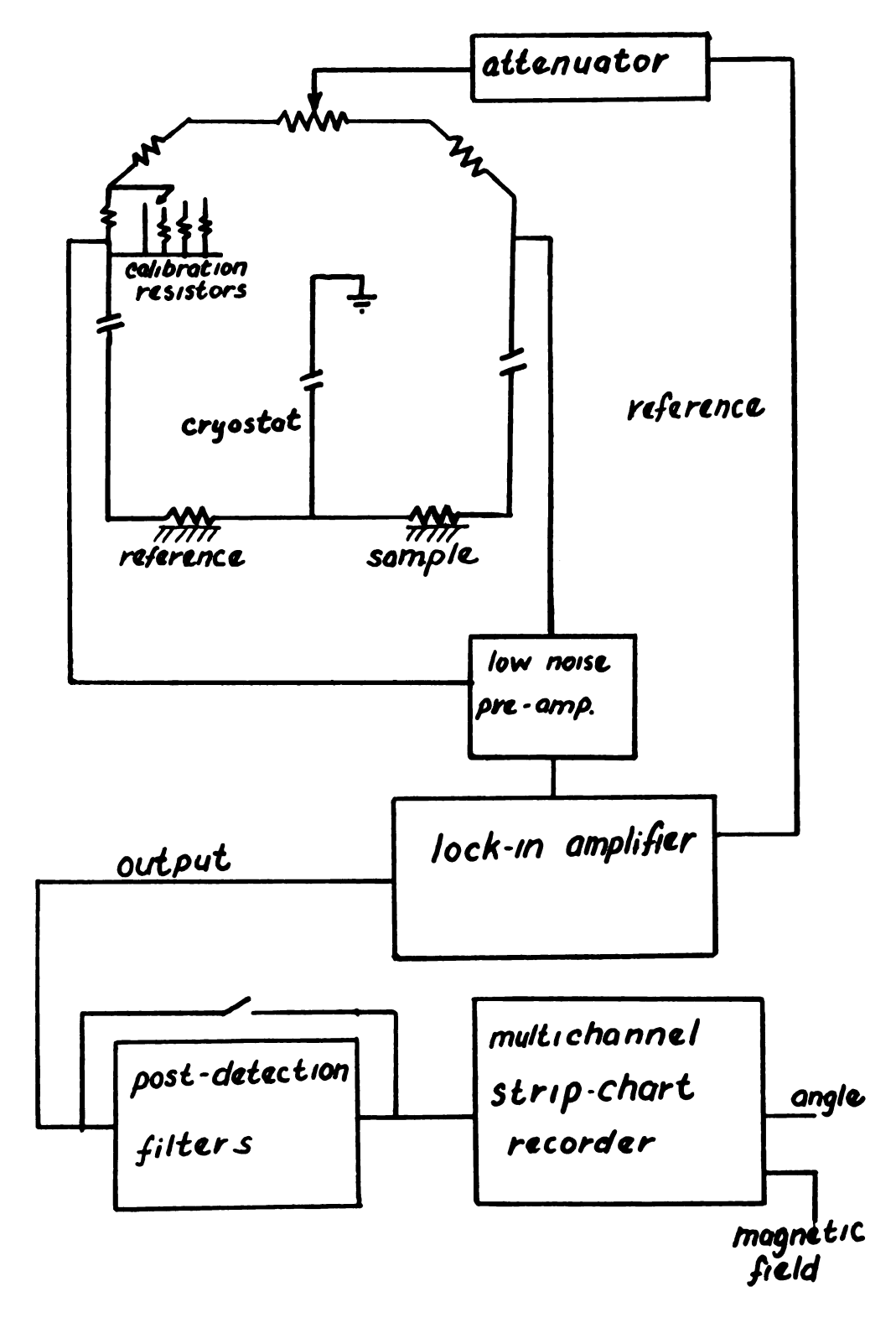


Fig. (4.4) Thermal Bridge and Associated Electronics

in detection scheme reduces both the electrical pickup and the effects of the sample vibrating in the magnetic field. Lock-in detection at the fundamental bridge frequency ω eliminates the I²R self-heating effects of the carbon resistors since these occur at 2ω .

A complete schematic of the bridge circuit itself is given in Appendix C. The simple d.c. equivalent circuit shown in Fig. (4.5) can be analyzed to yield the voltage across the detector input due to a small resistive change Δ . The result is

$$\sqrt{\text{detector}} = \frac{\Delta \mathcal{E} \rho}{\left[(2+\rho/R) r + \rho \right] \left[r + R + \Delta \right] + \Delta R}$$

However in practice $\Delta \langle \langle r, \rho \rangle$, R, so that

$$\Upsilon_{\text{detector}} \cong \frac{\Delta \mathcal{E} \rho}{\left[(2 + \rho/R) \, r + \rho \right] \left[r + R \right]}$$
 (4.2)

From Eqn. (4.1)

$$\Delta = \frac{Ar dT}{T^2}$$

Thus Eqn. (4.2) yields

$$\int_{\text{detector}} = \frac{A \mathcal{E} P r dT}{T^2 (2+P/R) r+P r+R}$$

$$= \frac{A \mathcal{E} P r dT}{T^2 (2+P/R) r+P r+R} (4.3)$$

Hence the voltage output of the detector is propor-

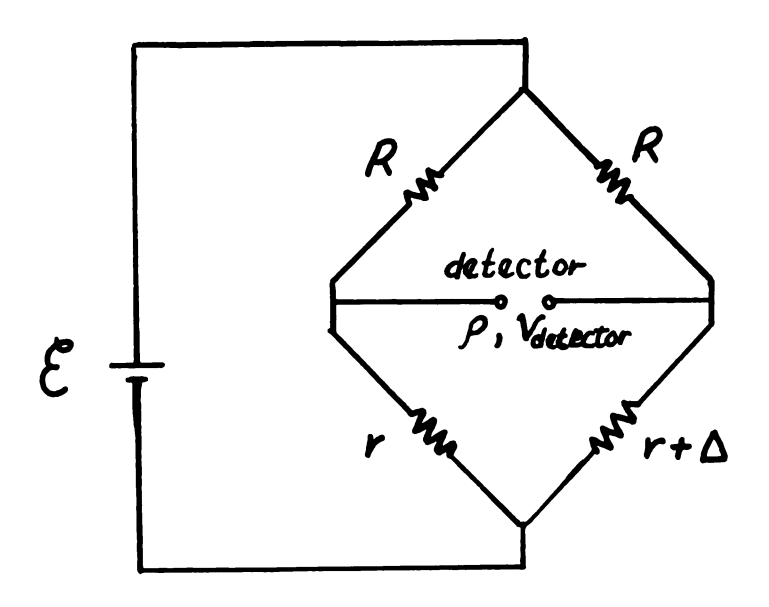


Fig. (4.5) D.C. Equivalent Circuit

tional to the temperature change of the sample. To determine the absolute temperature changes one must calibrate both the sample resistor to determine A and the electronics using the simple stepping calibration resistor which takes the place of Δ in Eqn. (4.2). The power dissipation in the sample resistor is typically around 10^{-11} watts. For the 33Ω , 1/8 watt resistors at 1.2^{0} K a temperature change of $1\mu^{0}$ K corresponds to a voltage input to the detector (with 50K input impedance) of $.005\mu$ V. This figure represents the practical lower limit of observation.

4.4 Magnetic Field Measurement

The accuracy with which one can determine the frequency of the MTO oscillations and hence the cross-sectional areas of the Fermi surface ultimately depends upon the measurement of the magnetic field. The magnetic field was measured by three methods in these studies. Initially a rotating coil gaussmeter (Rawson model 720) calibrated with an NMR probe was used. A magneto-resistance probe (American Aerospace Controls, Inc. model MRA-11) was also calibrated with the idea of using it in a high field solenoid. The resistance of the probe was found to be quite dependent on its orientation relative to the field. While this is not

		1

desirable for field calibration work it could be used for accurate orientation in a magnetic field. The effects of thermal cycling and temperature dependence in the 1° to 4°K range were less than .3%. A direct reading calibration circuit was designed for use with this probe and is presented together with the transverse calibration curve in Appendix D.

A digital hall probe gaussmeter (F.W. Bell Inc. model 660) was also used. The error of this device when used with the NMR factory calibration curve was reputed to be less than .2%.

The output of either of these devices was recorded concurrently with the thermal oscillations on either a 2 pen Varian or a 3 pen Texas Instruments (Servo/riterII) strip chart recorder.

4.5 Field Sweep Techniques

During the course of these measurements a very useful adaptation of the sweep unit originally designed by J. LePage was made⁵⁶. The LePage circuit shown in Fig. (4.6) is based on the fact that the Harvey-Wells electromagnet control will produce a current through the magnet proportional to an applied reference voltage. Since the H(I) curve for the iron electromagnet is not linear (Appendix E) one cannot simply make I=constant

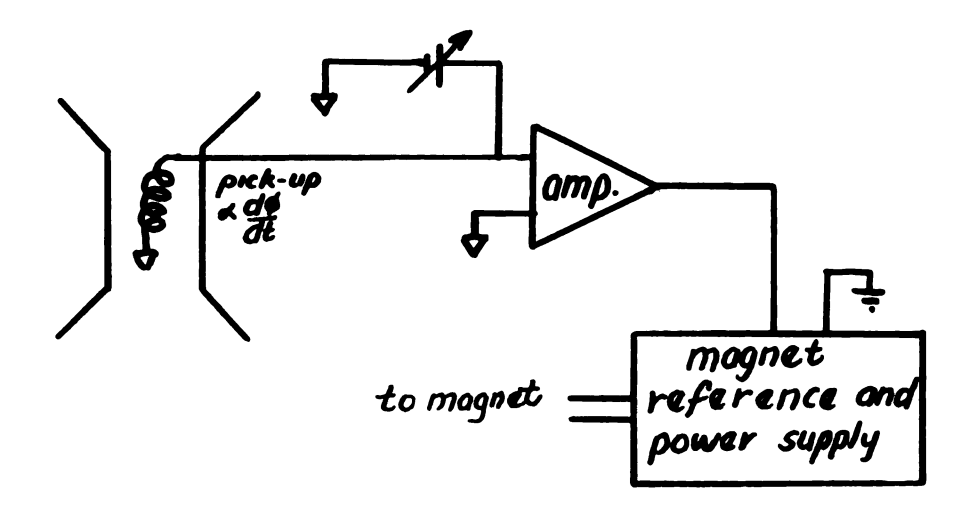


Fig. (4.6) Single Amplifier Sweep Control

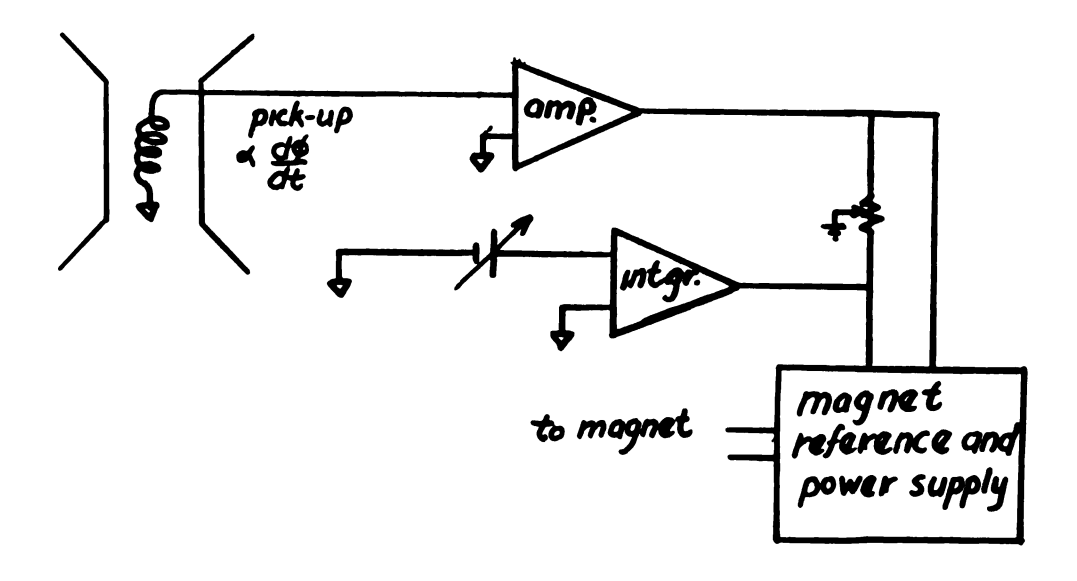


Fig. (4.7) Manual Integrator Sweep Control

to get a linear field sweep. In the LePage circuit d\$\omega\$/dt was compared with a constant voltage and the error signal used as a reference for the magnet control. In order to make a very linear device with one amplifier stage it was necessary to use very high gain (>10^4) for which the circuit would oscillate. In order to eliminate this problem the output of an operational integrator was also added to the magnet reference as shown in Fig. (4.7). The voltage which was integrated could be varied manually in such a manner as to keep the output of the error amplifier minimized.

This sweep unit was automated by simply using a part of the error signal to drive the integrator. One then has a quick responding error amplifier and a longer time constant electronic servo-integrator operating together in a closed loop. Since the loop is closed the accuracy of the control does not depend upon the linearity of the integrator and its rate of integration can be adjusted to minimize the output of the error amplifier. A modified sweep unit utilizing these principles has recently been constructed. A simplified schematic of this revised circuit is shown in Fig. (4.8).

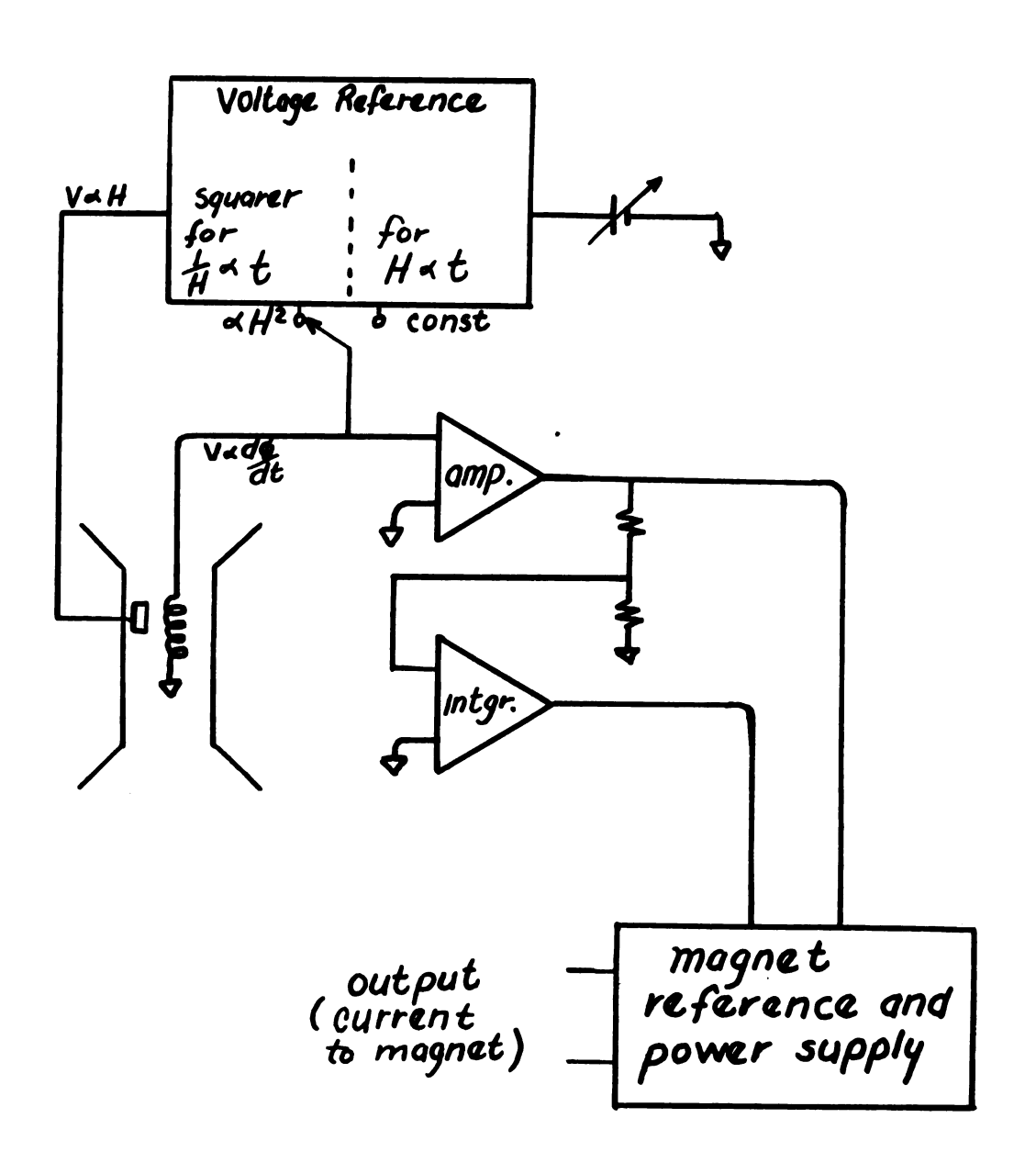


Fig. (4.8) Automated Sweep Control

The versatility of this sweep control becomes apparent when one considers the possibility of non-linear sweep modes. The voltage reference with which do /dt (or H) is compared by the error amplifier clearly determines the sweep mode.

For example, if V_{ref} =CH, then (CH-bH) is minimized so dH/H =(C/b) dt, which results in a sweep which is exponential in time.

In studying oscillatory effects which are periodic in 1/H (i.e. $\sin 2\pi f/H$) it would be very useful to have 1/H proportional to time.

Since the time separation of two adjacent oscillations is

$$(n+1) - (n) = f/H_1 - f/H_2 = (f/H_1H_2)(H_2-H_1)$$

thus

$$H_2 - H_1 = \Delta H = H_1 H_2 / f$$
 or $\Delta H \sim H^2 / f$

Thus for a sweep rate \dot{H} the time between successive peaks will be

$$\tau_{\text{osc}} = \Delta H/\dot{H} = H^2/f\dot{H}$$
 . (4.4)

So for time periodic oscillations we set

$$H^2/fH = A$$
 (a constant)

Thus for the above sweep control the reference with which H must be compared is simply proportional to ${\rm H}^2$.

Time-based 1/H sweeps have been described in the

literature 20,57 . The conditions necessary for their operation can be obtained from Eqn. (4.4).

$$dH/H^2 = dt/f \tau_{osc}$$

so that

$$1/H = -t/f \tau_{OSC} + C$$

or

$$H = f \tau_{osc} / [(f \tau_{osc}/H_0) - t]$$
.

But since

$$\tau_{\rm osc} = H_0^2/H_0f$$
 ,

$$H = H_0^2 / (H_0 - \dot{H}_0 t) \text{ or } \dot{H} = \frac{H_0^2 \dot{H}_0}{(H_0 - \dot{H}_0 t)^2} \text{ where } \dot{H}_0 = \dot{H})_{t=0}$$

Thus direct or differential comparison of the field with a time-based reference requires adjustment of the initial sweep rate \dot{H}_0 relative to H_0 . For this reason the time-based sweep, whether mechanically or electronically driven, is inherently more difficult to adjust initially for the 1/H characteristic. In the differential \dot{H} method described above the time between oscillations can be changed in the middle of the sweep by merely adjusting the amount of H^2 reference voltage which the error amplifier compares with \dot{H} .

It should be noted that this technique is not limited to electromagnets but is in fact more directly

applied to superconducting solenoids. The field in a solenoid is very nearly proportional to the current I. The voltage drop across a superconducting solenoid, being almost entirely inductive, is LI which is proportional to H - the correct pickup for the differential 1/H sweep. The reference with which to compare this can be obtained by squaring the current I.

In practice the magnetic field is sampled by the rotating coil gaussmeter and this signal is then squared. The squaring circuit first takes the log of H, then multiplies by 2, and then takes the antilog. As the accuracy of the log and antilog functions are crucial, a series of about thirty transistors were tested to determine which ones had the best logarithmic properties. Appendix F contains the relevant circuits and notes on operation. More accurate squaring and logarithmic devices with greater voltage range can be obtained from the George A. Philbrick Co. 58. Their units are heartily recommended for the construction of future sweep units.

4.6 Data Acquisition and Reduction

In this section the various conditions under which data is recorded are considered. Data analysis techniques are discussed concurrently with each method.

Additional methods that were tried as well as suggestions for modifications are also presented.

To obtain the frequency of a set of oscillations periodic in 1/H (i.e. \angle sin $2\pi f/H$) is in principle a simple task. One merely plots peak numbers versus 1/H and determines the frequency from the slope. A linear least squares program to do this has been written and is listed in Appendix G. A typical output complete with statistical parameters, errors for each peak and a 95% confidence interval for the period is also given there. The error intervals are to a large degree independent of linear errors in the magnetic field calibration and really reflect only the statistical uncertainty in locating oscillation maxima (or minima).

To seperate out simultaneously occurring frequencies, use can be made of the high pass filter characteristic which the thermal leak introduces. $(1/\sqrt{1+(\boldsymbol{t}_{\rm osc}/2\boldsymbol{\pi}\boldsymbol{t}_{\rm Q})^2})$ Examples of data taken using this technique are shown in Appendix H in Fig. (H.3) and Fig. (H.4). Two filters designed to be used with the 1/H sweep unit are also shown in Appendix H with an example of data output.

For the more dilute alloys the amplitude of the oscillations is large enough relative to the noise

and drift to permit analysis. Excluding geometric factors, spin splitting and simple power law dependence upon temperature and field, the amplitude is affected by four factors. From Eqn. (3.12) these four terms are

$$I_1 = \frac{1}{\sqrt{1 + (r_{osc}/2\pi r_Q)^2}}$$
, $I_2 = \frac{1 - b_{\ell} T/H \coth b_{\ell} T/H}{\sinh b_{\ell} T/H}$,

$$I_3 = e^{-b_{\mathcal{A}} X_{D}/H}$$
, $I_4 = \frac{1}{\left|\frac{\partial^2 A}{\partial K_Z^2}\right|_{ext}^{1/2}}$

where $b_{\ell} = 1.469 \times 10^5 \text{ m}_{c} */\text{m}_{o} \text{ } \text{ } \text{gauss}/\text{o}\text{K}$

 I_1 is the thermal damping due to the heat leak. For field sweeps linear in time, $\tau_{\rm osc}$ increases with increasing field and thus in order to quantitatively interpret amplitude effects one must measure $\tau_{\rm Q} = c_{\rm HL/KA}$.

 $\mathcal{T}_{\mathrm{osc}}$ is very simple to obtain from the strip chart records. A plot of $\mathcal{T}_{\mathbf{Q}}(\mathbf{H})$ which was measured at several temperatures for the .08 at.% sample is shown in Fig.(4.9). These measurements were made by noting the temperature change of the sample caused by a calibrated heater via the PL/KA term in Eqn. (3.12). With the 1/H sweep $\mathcal{T}_{\mathrm{osc}}$ is constant, so that \mathbf{I}_1 is solely a function of $\mathcal{T}_{\mathbf{Q}}$. From Fig. (4.9) $\frac{\Delta\mathcal{T}_{\mathbf{Q}}}{\mathcal{T}_{\mathbf{Q}}} \cong 7\%$ over the field range where the Dingle temperatures were determined. Since

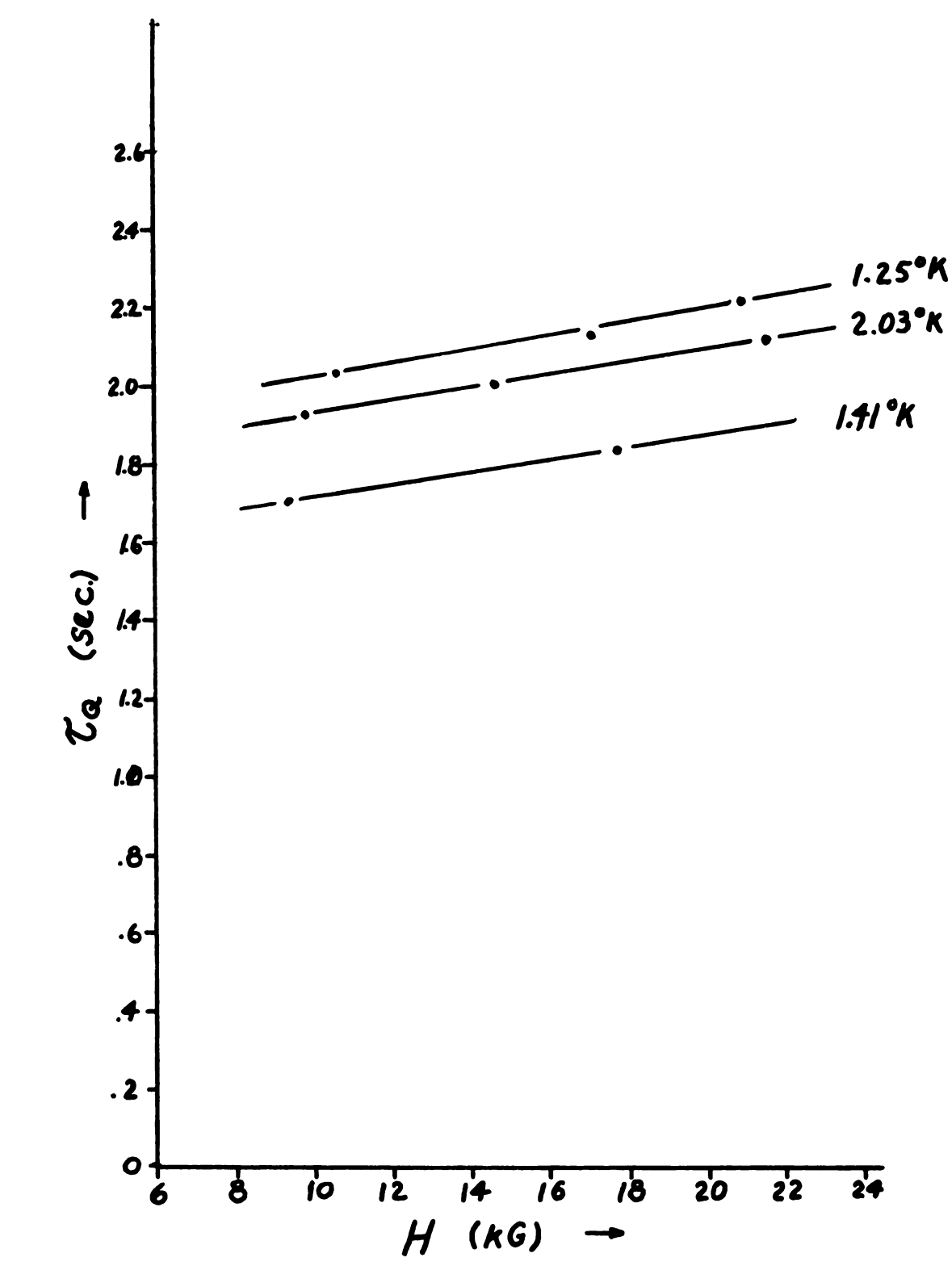


Fig. (4.9) Dependence of $7_{\mathbf{Q}}$ upon Magnetic Field

for most sweeps $au_{\rm osc} \simeq 2\pi au_{\rm Q}$ (the cutoff region). From Fig. (4.9) it follows that since the relative change in $au_{\rm Q}$ is only $\frac{1}{7}$ that of H

$$\frac{\mathrm{d}I_1}{I_1} = I_1^2 \left(\frac{\mathbf{\tau}_{\mathrm{osc}}}{2\pi \mathbf{\tau}_{\mathrm{Q}}}\right)^2 \frac{\mathrm{d}\mathbf{\tau}_{\mathrm{Q}}}{\mathbf{\tau}_{\mathrm{Q}}} = \frac{1}{2} \frac{\mathrm{d}\mathbf{\tau}_{\mathrm{Q}}}{\mathbf{\tau}_{\mathrm{Q}}} = \frac{1}{14} \frac{\mathrm{dH}}{\mathrm{H}}.$$

By recombining the Taylor series expansion of $I_1(H)$ about H_0 we have

$$I_1 = I_1$$
_{H₀} $e^{\frac{H^2 - H_0 H}{14 H_0}} / H$

Thus from the $ln(amplitude/H^{3/2})$ versus 1/H plot we do not measure X_D but

$$X_D - \frac{H^2 - H_0 H}{14 H_0 b_{\ell}} \simeq X_D - .04^{\circ} K$$

where m_c^*/m_o^*12 and H changes from 12 to 20 KG.

The term I_2 arises from thermal broadening of the Landau levels. In the dHvA effect the corresponding term is simply $1/\sinh(b_{\ell}T/H)$. A plot of both of these functions is given in Fig. (4.10) The cyclotron effective mass m_c^* (= $m_o b_{\ell}/1.469 \times 10^5$ G/OK) can be obtained by measuring the amplitude of the oscillations at a given field as a function of temperature. From Fig. (4.10) it is apparent that the dHvA amplitude is more sensitive to changes in b_{ℓ} T/H than is the MTO

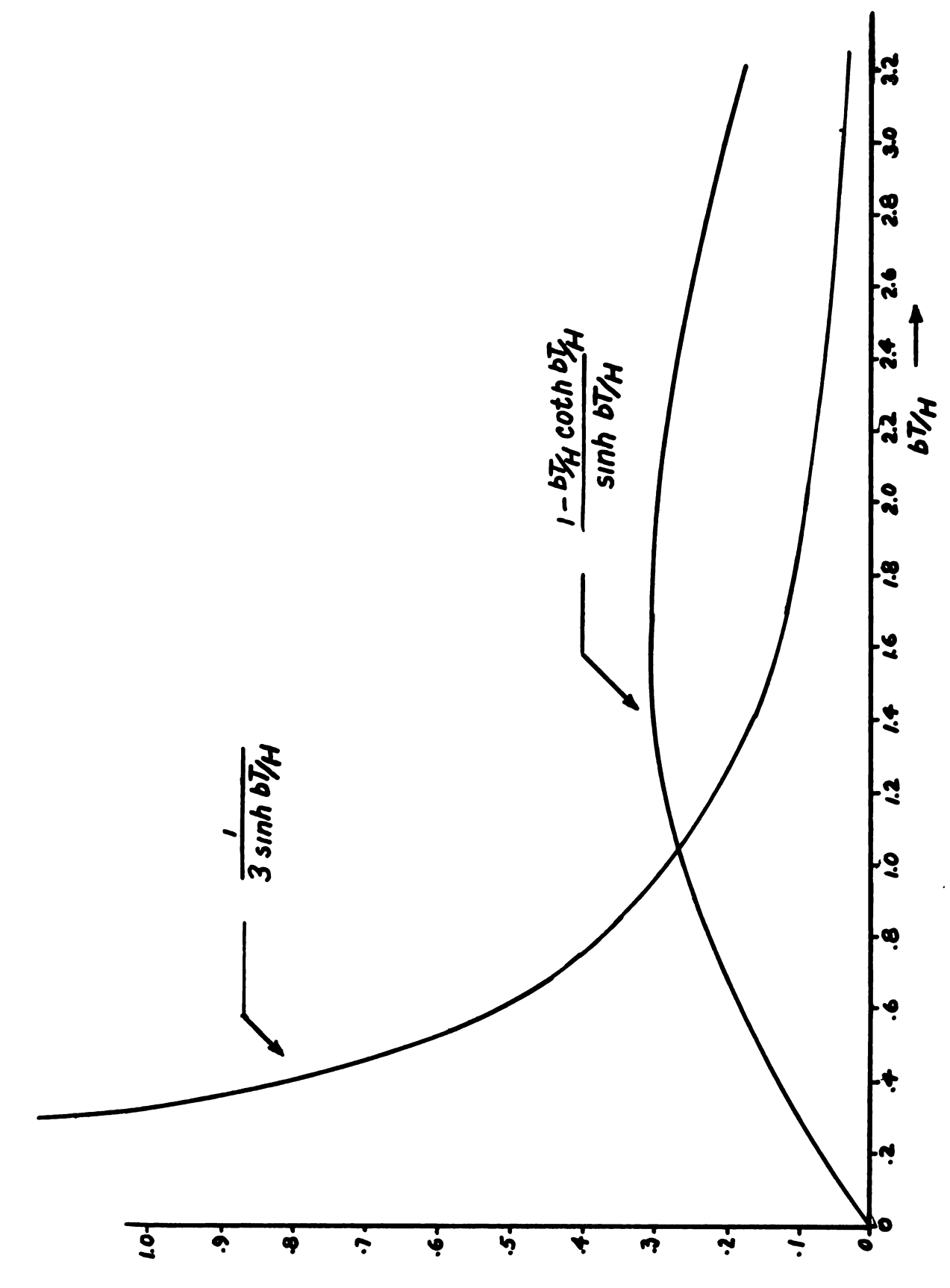


Fig. (4.10) Hyperbolic Dependence of MTO and dHvA Amplitudes upon T/H

effect, especially in the region where b_{ℓ} T/H ~1.6 . Thus m* can be determined more accurately with the dHvA effect than with MTO.

The term $I_3 = e^{-b_{\ell} X_D/H}$ represents the effects of collisions. The so-called Dingle factor X_D can be determined by measuring the field dependence of the amplitude at fixed temperature. Because the factor I_2 for MTO goes through maximum at $b_{\ell} T/H \sim 1.6$, for a given m* (and hence b_{ℓ}) one can fix T so that $I_2 = .31 \frac{+}{-} 2\%$ while H has been increased by a factor of ~ 1.6 . For the part of the aluminum Fermi surface studied here (3rd zone), m* $\simeq .12$ m₀ so that for fields between 13.5 and 22 KG, I_2 will be in this constant region if $T \simeq 1.5$ K. Although this makes the measurement of m* difficult it is very fortuitous for measurements of X_D . Thus for 1/H sweeps where $I_1 = \text{constant}$

$$\log \frac{Amp}{H^{3/2}} = -\frac{b X_D}{H} + C$$
 (4.5)

over a fairly wide field range and a simple log plot easily gives $b_{\mathbf{k}} X_{\mathbf{D}}$.

In addition to field sweeps another method of taking data was used. This consists of holding the magnitude of the field constant and rotating the sample relative to the field or vice versa. In practice since

the magnet was motor-driven and had a simple angular index it was most convenient to rotate the field. For a given field strength H the Landau level whose cross-sectional area is about equal to extremal area has quantum number

$$n = f/H$$

where f is proportional to the extremal cross-sectional area of the Fermi surface. At an angle Θ away from the first,

$$n(\Theta) = f(\Theta)/H .$$

Thus if one does some field sweeps to find $f(\Theta)$ in major symmetry directions and to get a qualitative idea of the angular variation of f, the steady field rotation method can be used as a very accurate interpolation scheme. Data taken using this method is shown in Fig. (4.11).

To deduce $f(\Theta)$ we count peaks through a monotonic region of Θ from a known f. Then

$$f(\Theta) = \frac{+}{n} H(n(\Theta)-n) + f .$$

Since the quantum numbers n = f/H are usually from 30 to 500 in most of these measurements the method can be quite accurate.

An interesting alternative technique which has not been tried would be to parallel field modulate over a

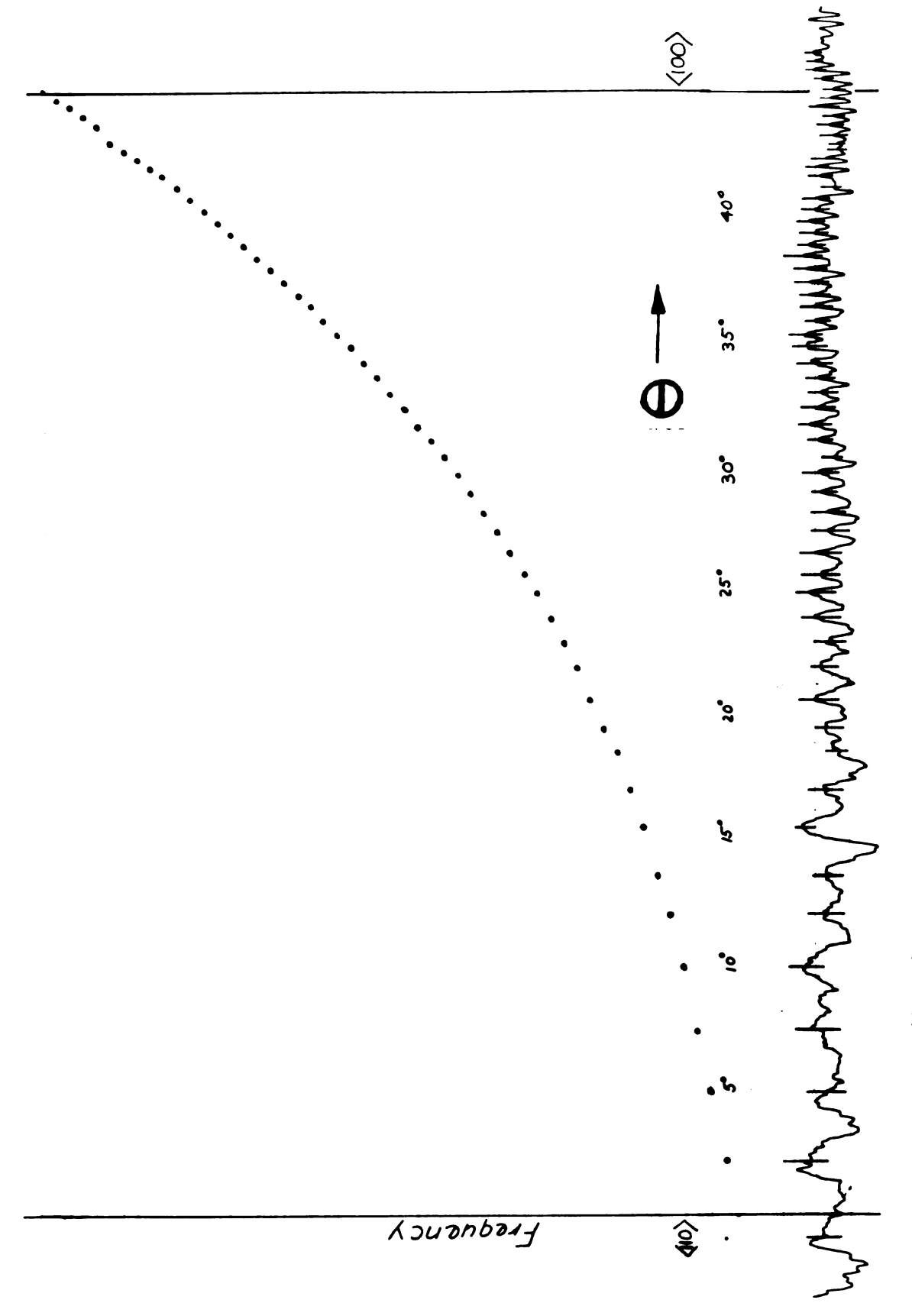


Fig. (4.11) Steady Field Rotational Techniques

given oscillation and "lock" onto this oscillation as the field rotates, adjusting the d.c. field to accomplish this locking in on a given oscillation.

Thus with the phase of the oscillations constant

f/H = constant or $f(\Theta) \ll H(\Theta)$. (4.6) Hence a record of the $H(\Theta)$ necessary to satisfy Eqn. (4.6) immediately gives $f(\Theta)$ to within a simple multiplicative constant.

In addition to the a.c. bridge and lock-in amplifier technique a field modulation method was also
tried. A block diagram of the electronics is shown in
Fig. (4.12). In this method the modulation signal via
PSD 2 could be compared with the standard a.c. bridge
technique via PSD 1. Although the signal to noise ratio
of the modulation technique could be increased by
increasing reference power to the bridge it was still
lower by a factor of about 5 than the standard technique.
This method was therefore not pursued.

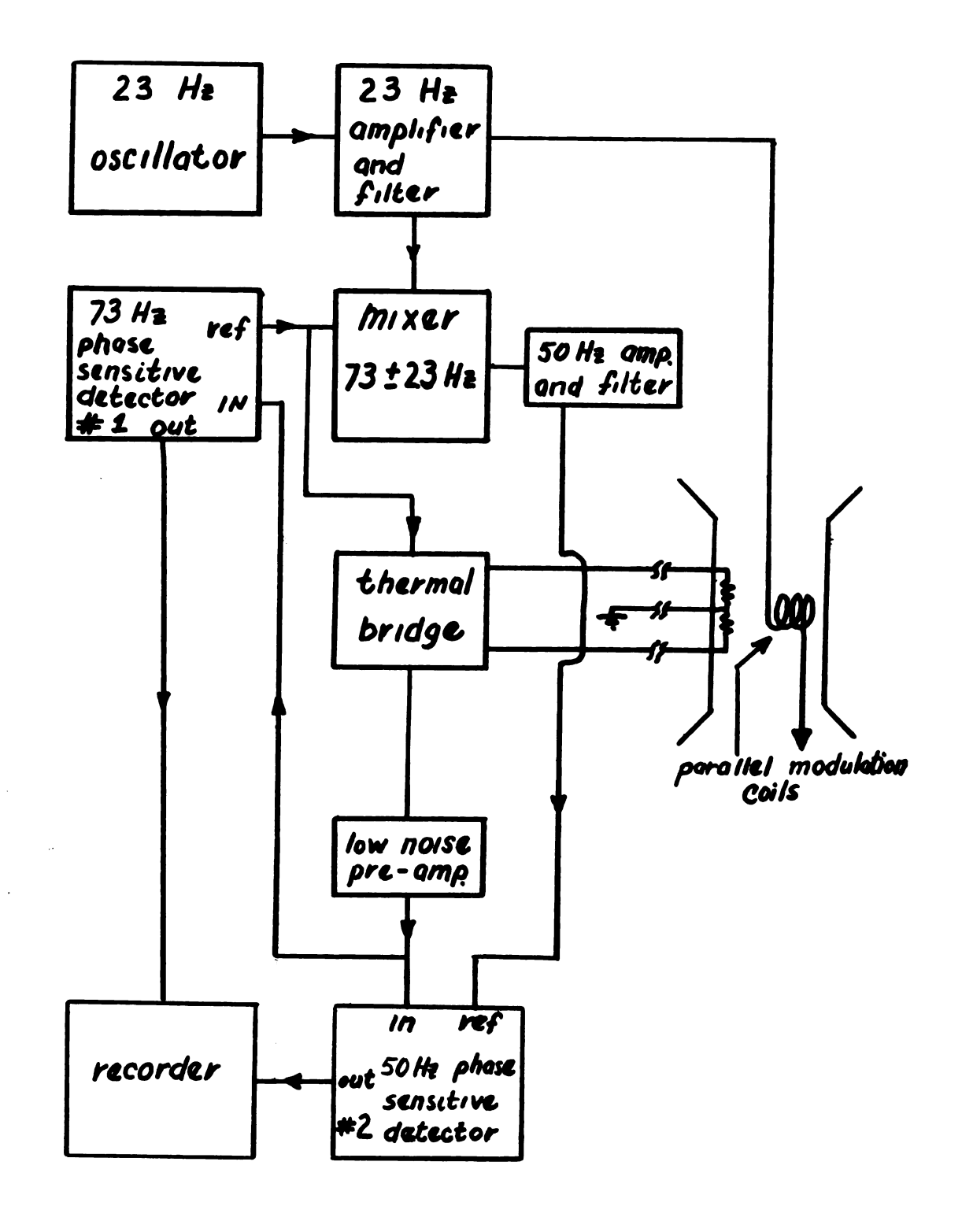


Fig. (4.12) Field Modulation Electronics

CHAPTER V

SAMPLE PREPARATION

5.1 Introduction

In this chapter the method used to grow the dilute alloy single crystals is discussed. The effects of non-uniformity in solute concentration and crystal structure are also considered. The techniques used to determine solute concentration and crystal imperfections are described. The chapter is concluded with a presentation of the results of such measurements on the present samples.

5.2 Necessary Precautions

It seems obvious from the start that if one wants to study the Fermi surface of a metal for different alloy concentrations at least two requirements must be met.

Since the solute concentration is expected to have some effect upon the size and shape of the Fermi surface, we require that the solute concentration for any given sample be as constant as possible. Spatial regions of the crystal where the Mg concentration differs greatly from the mean will lead to properties typical of that concentration. Thus an assembly of such regions should be expected to broaden the range of measured values for any

parameter whose value depends upon solute concentration. This effect will reduce the confidence in the values which one measures for carrier lifetimes at the Fermi energy. The effect will also produce a damping of the amplitude of the oscillations.

The second requirement is related to the single crystal nature of the sample. Since the Fermi surface for any polyvalent metal differs greatly from a sphere the extremal cross-sectional areas will depend upon the orientation of the magnetic field relative to the crystalgraphic axes. If the crystal orientation varies with position, the extremal cross-sections of Fermi surface and hence the frequency of the oscillations, will be a function of position. Thus the oscillations observed from such a sample will vary as $\sum_{i} \sin \frac{2\pi (f_0 + \Delta f_i)}{H}$. For low field or high frequency oscillations where f_0/H is very large Δf_i will have a much greater effect than in the high field region. Thus microstructure can lead to a field dependent damping which could be confused with a Dingle temperature (although it should have greater effect upon high than low frequency oscillations).

5.3 Crystal Growth

The theory and associated techniques which made possible the preparation of samples necessary for this

study are largely a product of the last fifteen years⁵⁹. Much of the stimulus for this development has been provided by the semiconductor industry. Since we are chiefly concerned in this study with the growth of alloy single crystals the following discussion will center on this problem.

It is convenient to begin the discussion with some assumptions and definitions. Suppose one begins with a slug of Mg - Al alloy of roughly uniform concentration. In our study such a slug was obtained by chill-casting a well mixed solution of the alloy in a reduced nitrogen atmosphere. The distribution coefficient, K_0 , is defined as the ratio of the solute concentration in the solid (C_8) to its concentration in the liquid (C_L) . This ratio depends upon the temperature at which the zone refining is done, but as seen in Fig. (5.1) the value for low concentration alloys of Mg - Al typically is about 0.3 .

The zone refining technique is to melt a small region of metal while the remaining material remains solid. The material is then slowly moved relative to the heat source so that a molten zone is gradually swept through the starting ingot. In the samples prepared for this study the zone was produced by a radiant

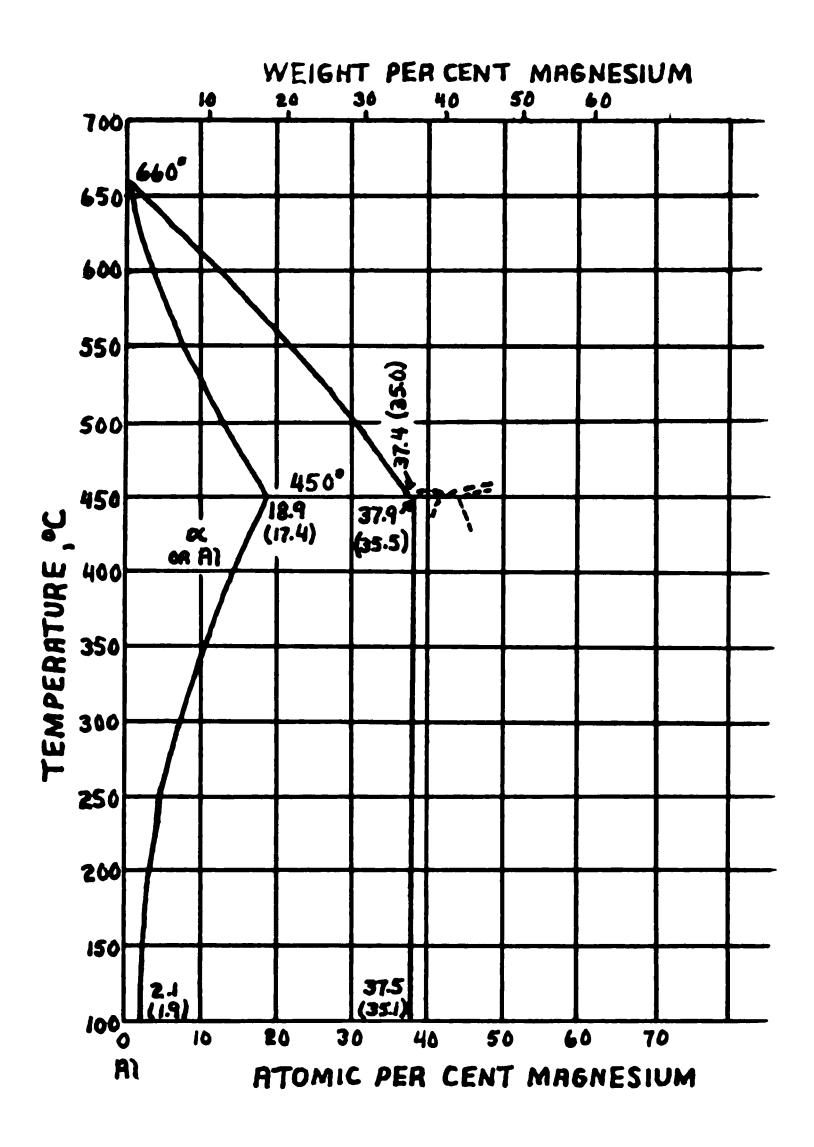


Fig. (5.1) Aluminum-Magnesium Phase Diagram

1
1
1
,
•
1

energy projection lamp obtained from the Materials Research Corp. In addition to the lamp and associated elliptical reflector an additional heater was used to raise the temperature of the remainder of the alloy to within about 300°C of its melting temperature. With this technique it was possible to maintain a molten zone of about 1/2 inch in length. The ingot is placed in a graphite boat which is then sealed off in a Vycor tube in a reduced atmosphere of nitrogen. At the working temperature the pressure of the nitrogen gas is very near atmospheric. This assembly is then placed under the lamp and a molten zone initiated at one end of the slug. The concentration of solute CI. (in this case Mg) is in this first zone just the initial equilibrium concentration C_{O} . As the zone moves on, some solidification begins at the end of the rod. The solute concentration of the solid initially frozen is

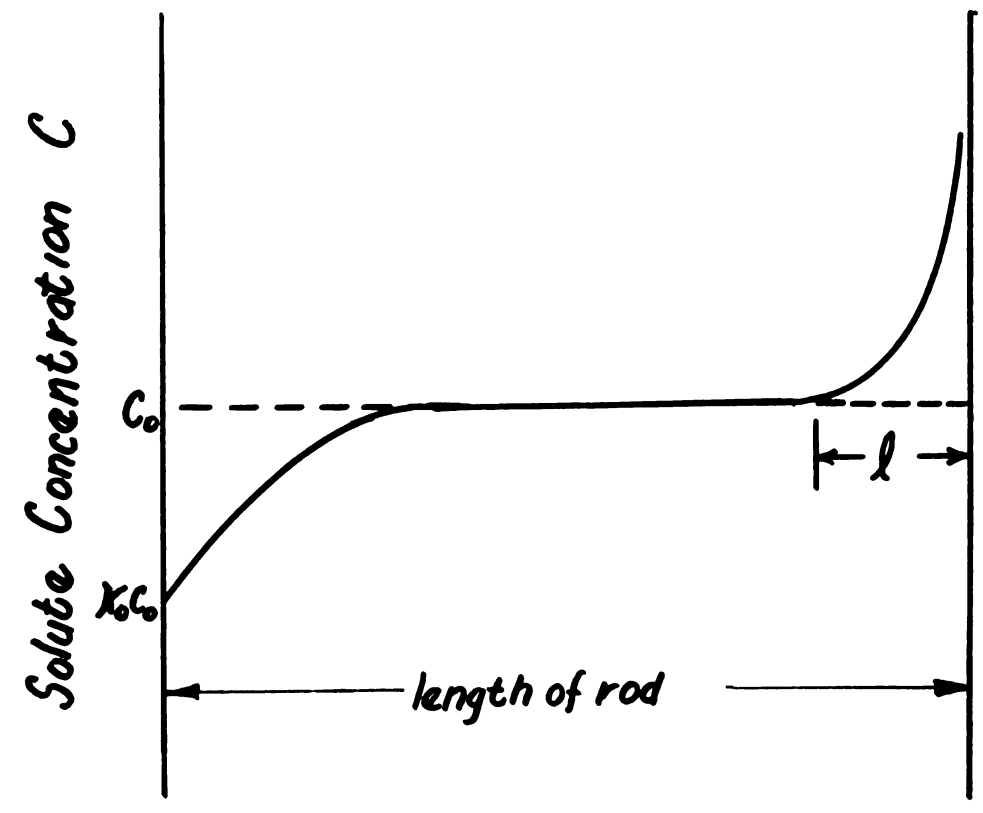
$$C_s = K_o C_o$$
 .

Since for Mg - Al this C_S is less than C_O , the amount of solute in the molten zone increases. The solute concentration keeps increasing until $C = C_O/K$. At this point the amount of solute being melted is equal to the amount freezing out. This situation continues until

the leading edge of the zone reaches the end of the slug. At the instant this happens the solute concentration C in the molten zone is $\mathrm{C}_{\mathrm{O}}/\mathrm{K}$, which is substantially larger than Co. Thus as the zone passes out through the last zone length of the crystal the concentration of solute in both the liquid and solid states increases in an exponential fashion. Fig. (5.2) shows what one expects for the solute concentration as a function of position after a single pass. By repeated unidirectional passes a very uniform gradient of solute concentration can be established. For low K it is possible to obtain impurity concentrations as low as one part in ten billion at the initial end. An important variation of this technique was used to grow the crystals used in this study.

The first pass was performed in essentially the above manner. The second pass was made in the opposite direction. Reversing the direction makes the first molten zone of the second pass have initial concentration, $C = C_0/K$, the concentration necessary to establish the region of constant solute. Thus after the second pass the crystal should have at least a middle region of very constant solute concentration.

An additional result is brought about by the zone



 $C_o = average solute concentration$ $K = \frac{C_{solid}}{C_{liquid}} = distribution coefficient$

Ko = aguilibrium distribution coefficient

L = length of zone

Fig. (5.2) Magnesium Concentration after Single Pass Zone Refining

•
,

refining method. The resulting crystal is found to be single over much of its length.

5.4 Resultant Crystals

Four samples with magnesium concentrations ranging from 0.1 to 0. 52 at.% were prepared in the above fashion. The resultant rods were examined using Laue back-reflection X-ray techniques. The photographs showed that most samples were single over at least the central three inches. (One of the intended samples showed that 5 crystals had been formed and that they persisted over this central length.) The samples to be used were cut from the central regions of their respective crystals using a Servo-met spark machine. These samples were then X-rayed, oriented with (100) axis along the X-ray beam axis using a convenient goniometer arrangement and a {100} face sparkplaned with the crystal still mounted in the goniometer. The samples were then glued by this {100} plane to an accurately machined graphite holder. (Fig. (5.3)) Using this method it was possible to estimate the initial sample orientation to within about 2 degrees about one axis and to within 4 degrees about a perpendicular one.

Samples prepared in the above fashion were weighed and their residual resistivity ratios (RRR) measured

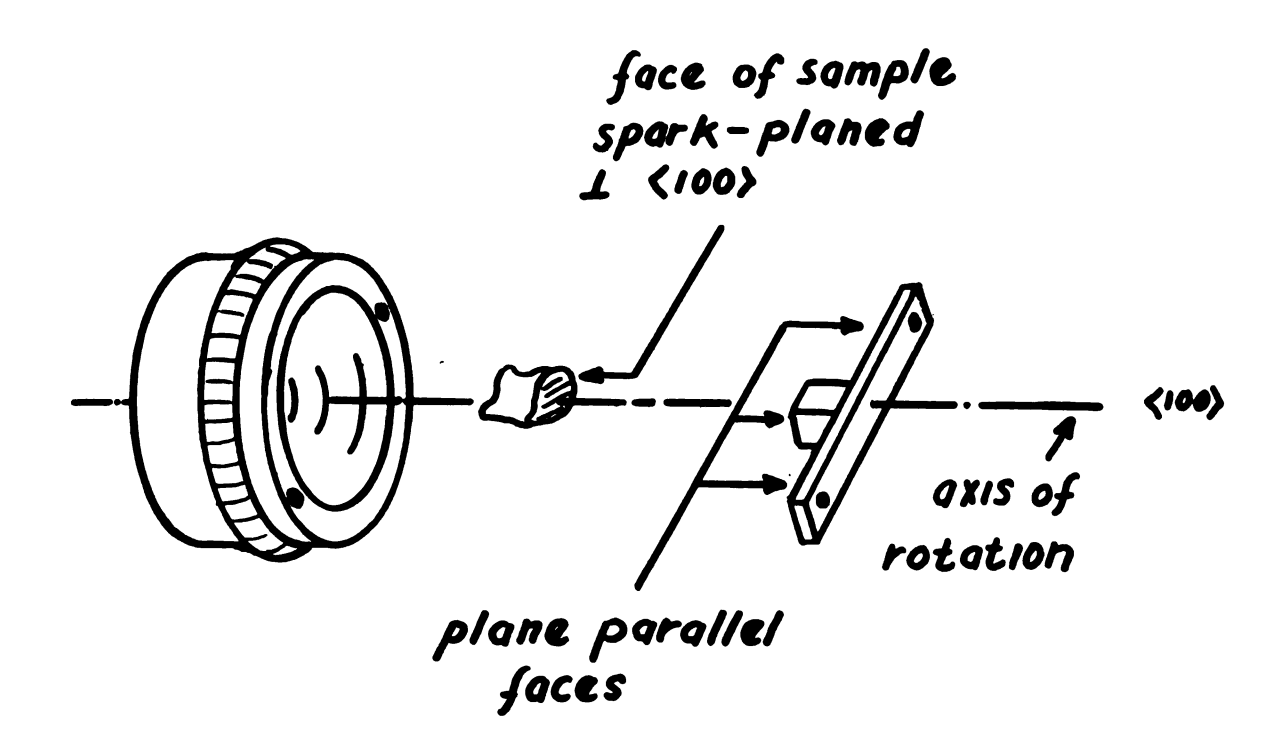


Fig. (5.3) Sample Mounting

between 4.2°K and room temperature. These data as well as the physical dimensions of the samples are given in Table (5.1).

Using the data of B. Serin⁶⁰ for the contribution to the resistivity due to impurity scattering as a function of magnesium concentration, one arrives at the calculated values of magnesium concentration as listed in the final column of Table (5.1). This calculation assumes that the low temperature resistivity is due to impurity scattering. The correlation between the impurity concentration before mixing and that calculated from the resistivity ratio is reassuring.

Table (5.1) Sample Information

sample number	at.% Mg before zone refining	Residual Resis-* tance Ratio(RRR)	at.% Mg from RRR	
1	.13	108	.08	
2	.40	22	.39	
7	.22	66	.13	
pure Al	6-9's oriented single crystal			

These samples including the pure A1 sample were roughly in the form of cubes; the masses ranged from .3 to .5 grams.

 $[*]_{RRR} = \rho_{3000K} / \rho_{4.20K}$

CHAPTER VI

THE FERMI SURFACE OF PURE ALUMINUM

6.1 Introduction

One of the reasons for undertaking a dilute alloy study in aluminum is that the Fermi surface has been relatively well established by a wide variety of techniques. In this chapter the agreement between the experimental data and various theoretical calculations is discussed and a presentation of the relevant data obtained in this study is also made.

6.2 Existing Fermi Surface Models and Data

The early work of Heine⁶¹ (1957) showed that the valence wave function in aluminum is well represented by a single orthogonalized plane wave (OPW) except near the Brillouin zone boundary. A nearly free electron (NFE) construction in which the contours of constant energy are spherical was first used by A. V. Gold⁶² to interpret his dHvA data in lead. In a magnetic field the effect of the lattice is to reflect the orbiting charge carriers at the Bragg reflection planes and to thus separate the carriers of one zone from those of another. By translating the corresponding

pieces of each zone back into the central zone Gold was able to form the Fermi surfaces corresponding to carriers of a given zone. The remarkable thing is that this naive model was able to explain the lead dHvA results. This reduced zone remapping procedure is especially tedious in three dimensions. In 1959 W. A. Harrison 63 greatly simplified the method when he realized that instead of considering only one sphere and the Bragg reflection planes, the same reduced surfaces could be obtained directly from the intersection of Fermi spheres centered on each lattice point. Thus since Heine's work had shown that aluminum is a good NFE metal it was selected by Harrison for the first trial of the method. The Harrison construction, Fig. (6.1), was quite successful in interpreting Gunnerson's preliminary results⁶⁴ for the third zone surface. More recently (1963) Ashcroft 65 has used an OPW pseudo-potential with coefficients adjusted to fit the third zone results of Gunnerson and also those of Gordon . Although Ashcroft's "final model" confirms the Harrison construction in general, it predicts a different connectivity near the W point of the zone. This is, of course, where one would expect the one OPW calculation to fail. The Ashcroft model showing the

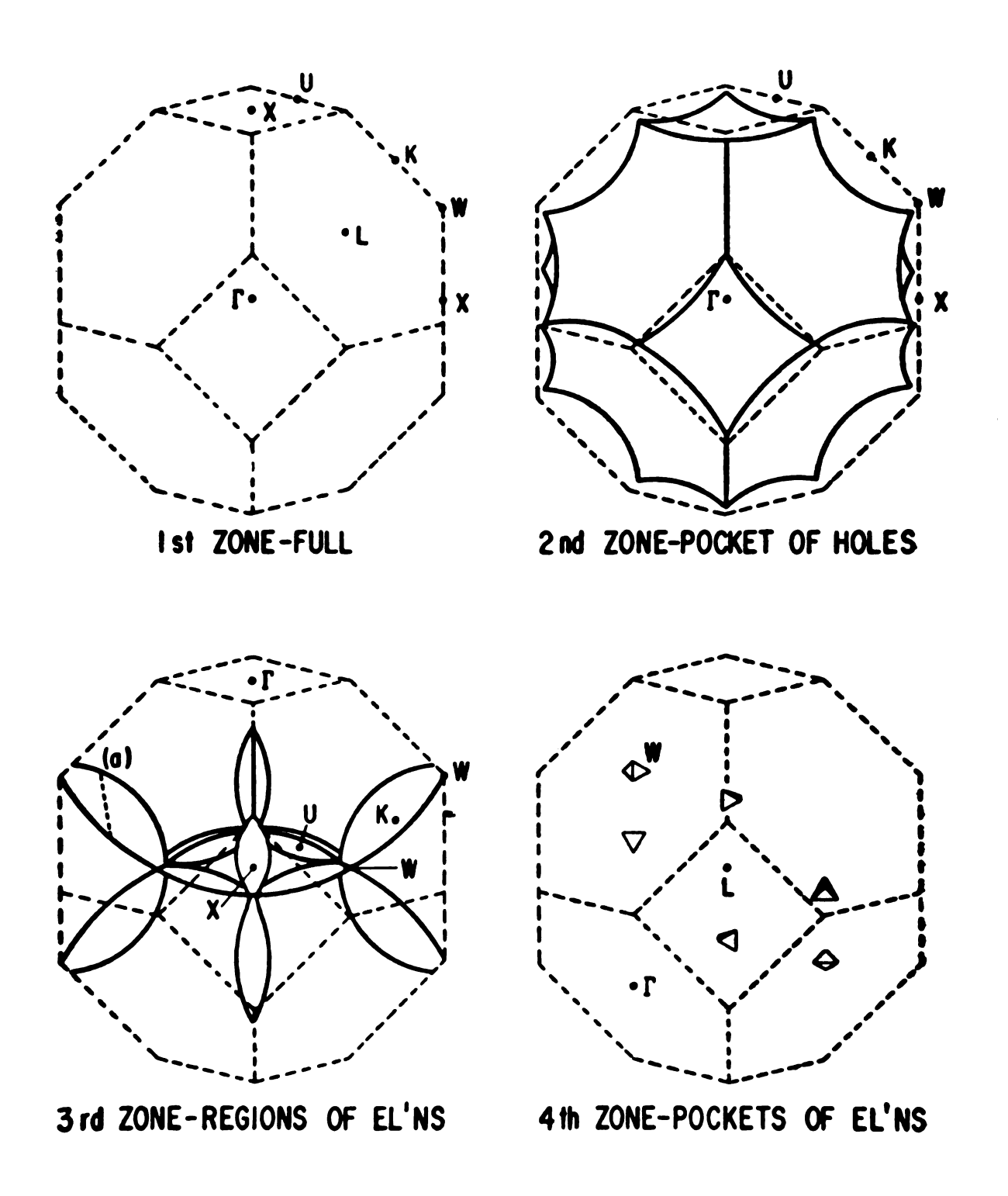


Fig. (6.1) Nearly Free Electron Construction for Aluminum

dismemberment of the third zone "monster" into "rings of four" is shown in Fig. (6.2).

The Ashcroft model which agrees quantitatively with Gordon's data is shown in Fig. (6.3). The pure aluminum data taken in the present study is also shown. These measurements are not intended to represent a Fermi surface determination but instead, a check of the experimental method being used. The anomalous skin effect results of Vol'skii⁶⁷ as well as the ultrasonic attenuation measurements of Kamm and Bohm⁶⁸ are in good agreement with this model. The existence of the β orbits is not consistent with Harrison's model but is predicted by Ashcroft's, thus confirming the latter model.

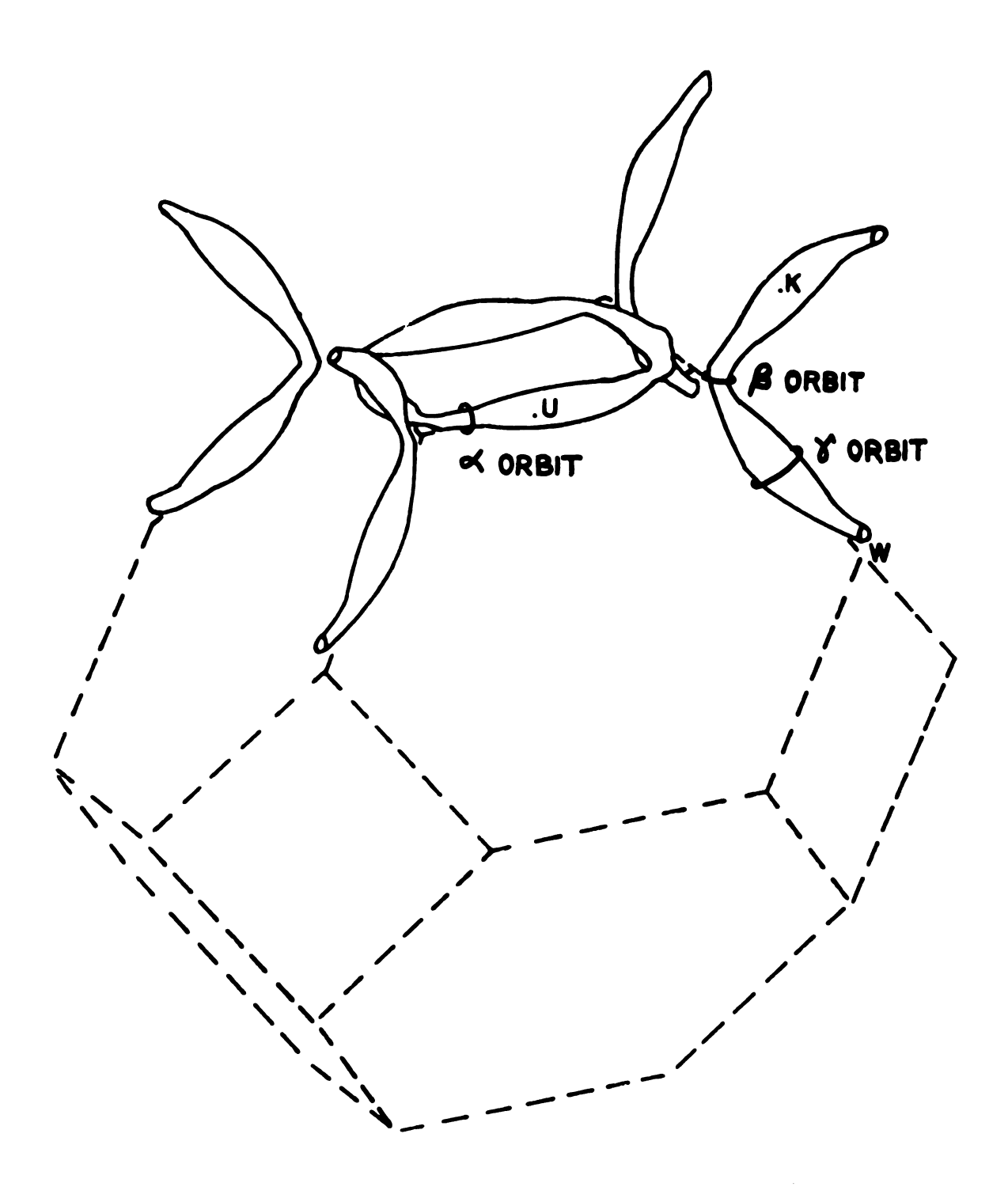


Fig. (6.2) Ashcroft's Model for the Third Zone Surface of Aluminum 66

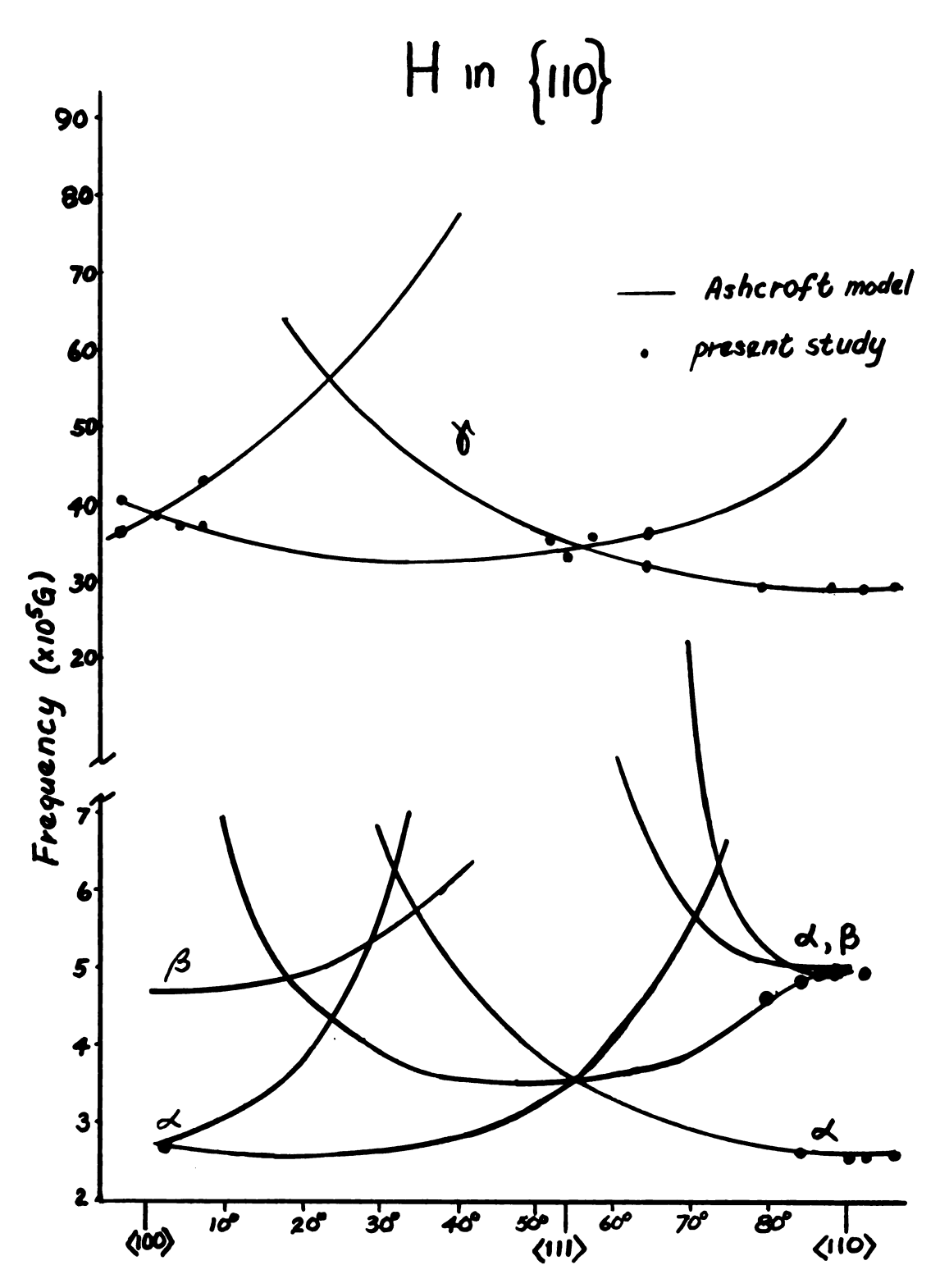


Fig. (6.3) Comparison of Data with Ashcroft's Model in {110} Plane

CHAPTER VII

EXPERIMENTAL RESULTS FOR AL-MG ALLOYS

7.1 Introduction

Experimental data has been taken with the intention of analyzing it to determine the shape and size changes of the Fermi surface caused by alloying. One might expect the effects to be small for dilute alloys with solute concentration less than 1/2 at.%. It is found, however, that changes in extremal cross-sections in the small third zone electron surface of Al can be as large as 10%.

The amplitude of the oscillations has also been studied as a function of temperature, field, and angle. From these measurements one can determine Dingle scattering factors.

When the magnetic field is rotated away from a symmetry direction the analysis becomes more difficult due to the larger number of frequencies present. This difficulty is especially apparent for the more concentrated alloys where the amplitude of the signal has been greatly reduced via the Dingle factor.

Throughout the following discussion the oscillations

are divided into high (%) and low (\checkmark and /3) frequency groups as indicated in Fig. (6.2). Rotation angles from $\langle 110 \rangle$ in a $\{100\}$ or a $\{110\}$ plane are denoted by /3 and /3 respectively.

7.2 Changes in the Aluminum Fermi Surface Induced by Alloying

The angular variation of the β orbit near $\langle 110 \rangle$ in a $\{100\}$ plane has been studied for pure A1 and three alloys. The results are shown in Fig. (7.1). A systematic decrease in extremal cross-sectional area with increasing Mg concentration is apparent. The theoretical prediction for the angular variation of frequency in a $\{100\}$ plane shows four frequencies converging toward a common value at $\langle 110 \rangle$. Because these branches could not be resolved near $\langle 110 \rangle$ in the most concentrated sample it is difficult to put much emphasis on changes in the structure of the angular variation curves.

Since the cross-sections of the third zone electron surface are decreasing as di-valent Mg replaces trivalent Al, one is tempted to try interpreting these changes in terms of a rigid valence band model. By analogy with the NFE Harrison construction, changing the electron concentration scales the radius of the Fermi sphere. Since the third zone surface is formed by an

overlap of such spheres it should be quite sensitive to changes in k_F . Consider a simple model which assumes that the Fermi surface cross-sections scale quadratically with the amount that the Fermi "radius" overlaps the zone boundary. Thus along $\langle 110 \rangle$

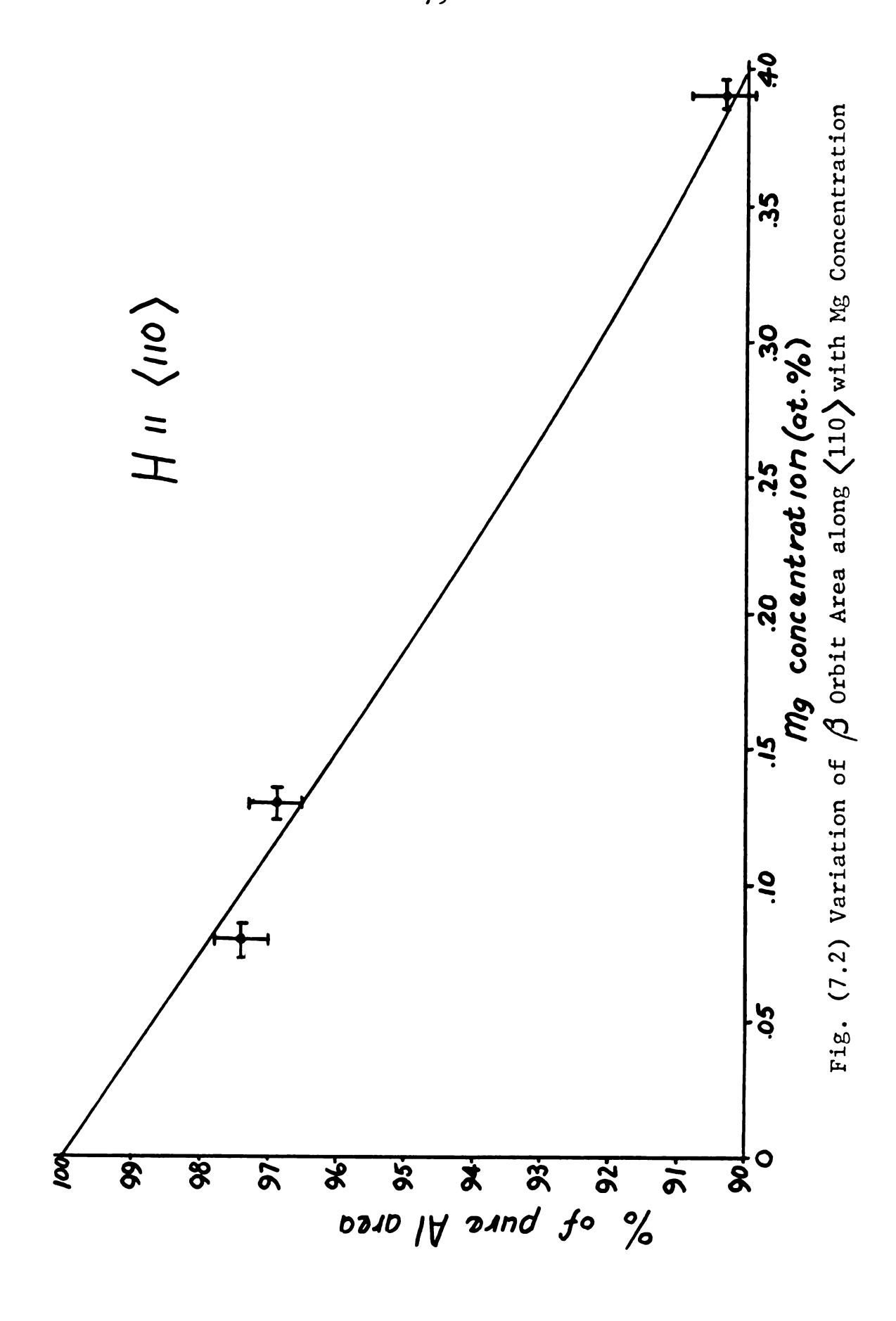
$$\frac{A}{A_0}$$
 = $(k_F - k_W)^2$ and $\frac{A}{A_0}$ = $(k_F - k_K)^2$

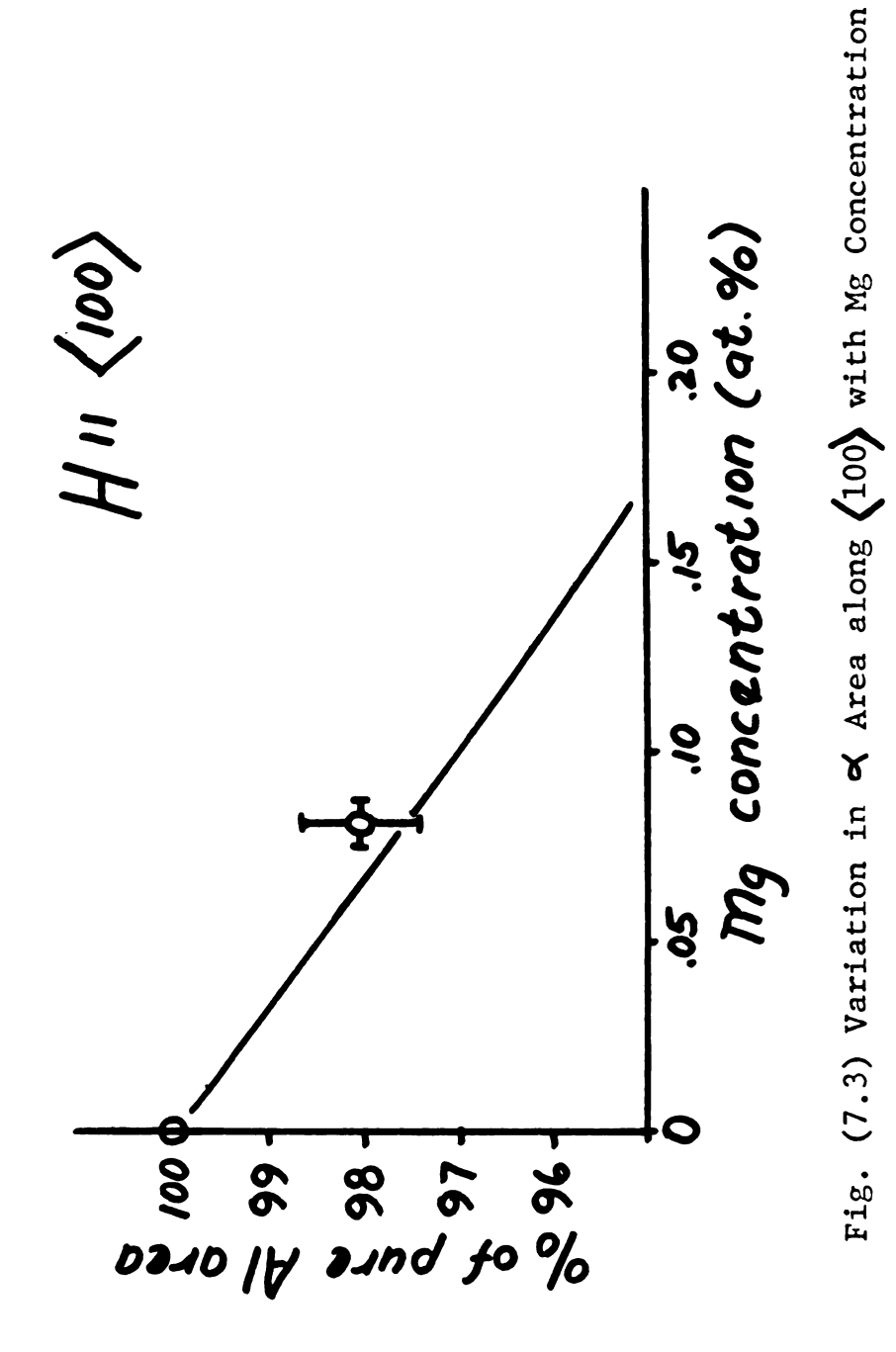
where $k_F \ll z^{1/3}$.

This model has been used successfully by Gordon et al 66 to interpret their Al-Zn alloy data. In Fig. (7.2) the 110 forbit data for Al-Mg is presented. The solid line corresponds to the above-mentioned calculation. This simple model agrees with the present data to within the experimental error although it is not applicable to all alloy systems. A similiar plot is shown in Fig. (7.3) for the .08 at.% alloy along 100.

The amplitude of the high frequency oscillations is only about 20% of that of the low frequency, and consequently their analysis presented difficulty. The only simplifying fact is that since the nearly cylindrical "arms" lie along $\langle 110 \rangle$ there is very little

Higgins and Marcus³⁰ found that in Zn alloys changes in the axial c/a ratio were at least equally as important as the valence effect described above.





beating of these Υ oscillations when the field is within 20° of this axis. The frequency of these oscillations near $\langle 110 \rangle$ in a $\{110\}$ plane for pure Al and the two most dilute alloys is shown in Fig. (7.4)A. In steady field rotations in a $\{100\}$ plane the oscillations come principally from the low frequency Υ oscillations.

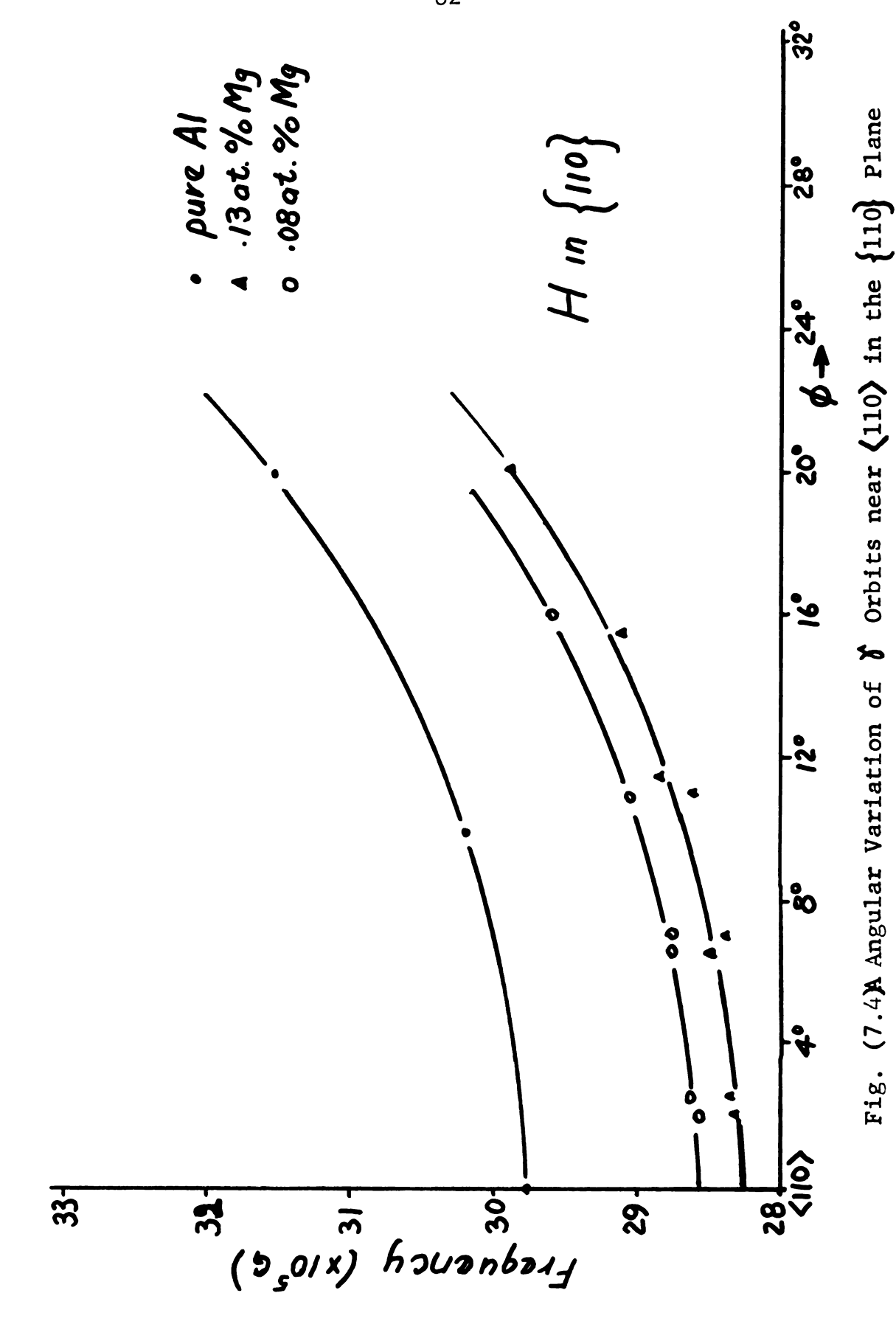
The variation of the *f frequency with magnesium concentration along (110) is shown in Fig. (7.4)B.

This frequency corresponds to the extremal cross-sectional area when the magnetic field is aligned with the axis of arms.

Steady field rotation plots, described in Section (4.6), were obtained for the two lowest concentration alloys. For the .08 at.% alloy it was possible to obtain good data throughout the $\{100\}$ plane. In the .13 at.% alloy the signal was smaller and its interpretation was difficult for Θ greater than about 15° . Plots of these frequencies versus Θ are compared with the pure Al data in Fig. (7.5).

7.3 Amplitude Dependence

As the field is rotated away from (110) the amplitude of both the high and low frequencies decreases. Rough measurements of this decrease were made for all of the samples studied and are shown in Fig. (7.6). As the



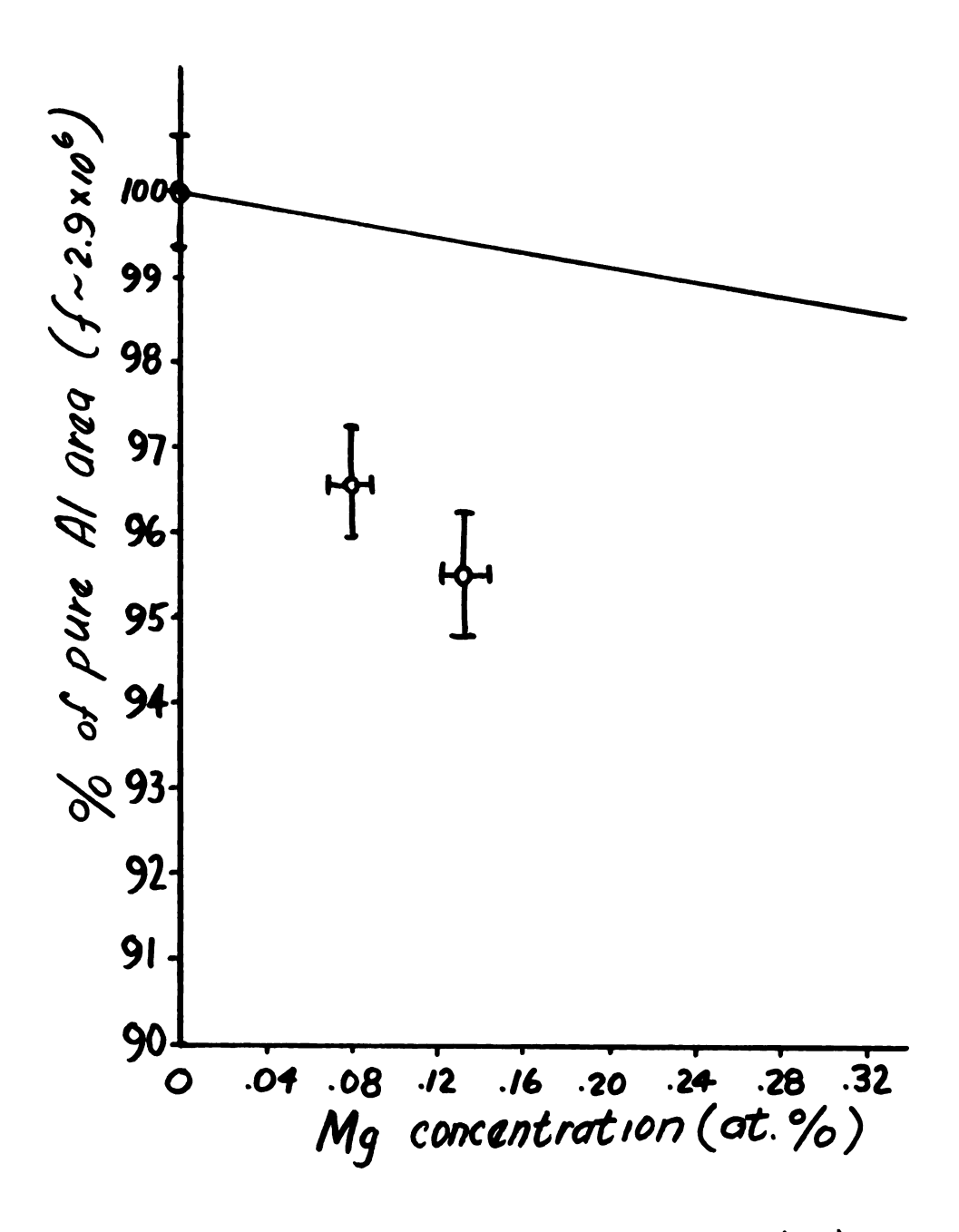


Fig. (7.4)B Variation in 7 Orbit Area along (110) with Mg Concentration

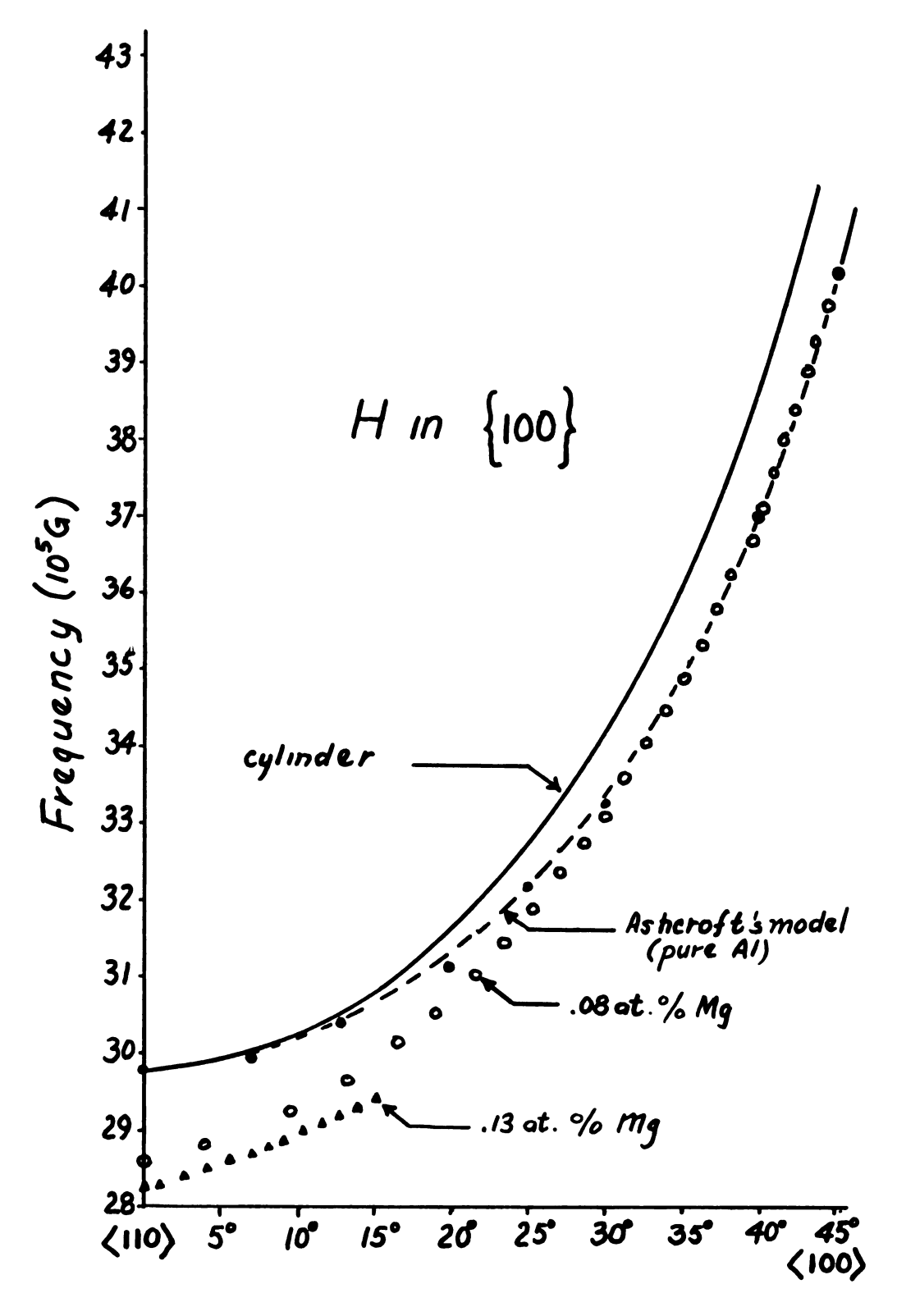


Fig. (7.5) Angular Variation of $\mbox{\em T}$ Orbits in $\{100\}$

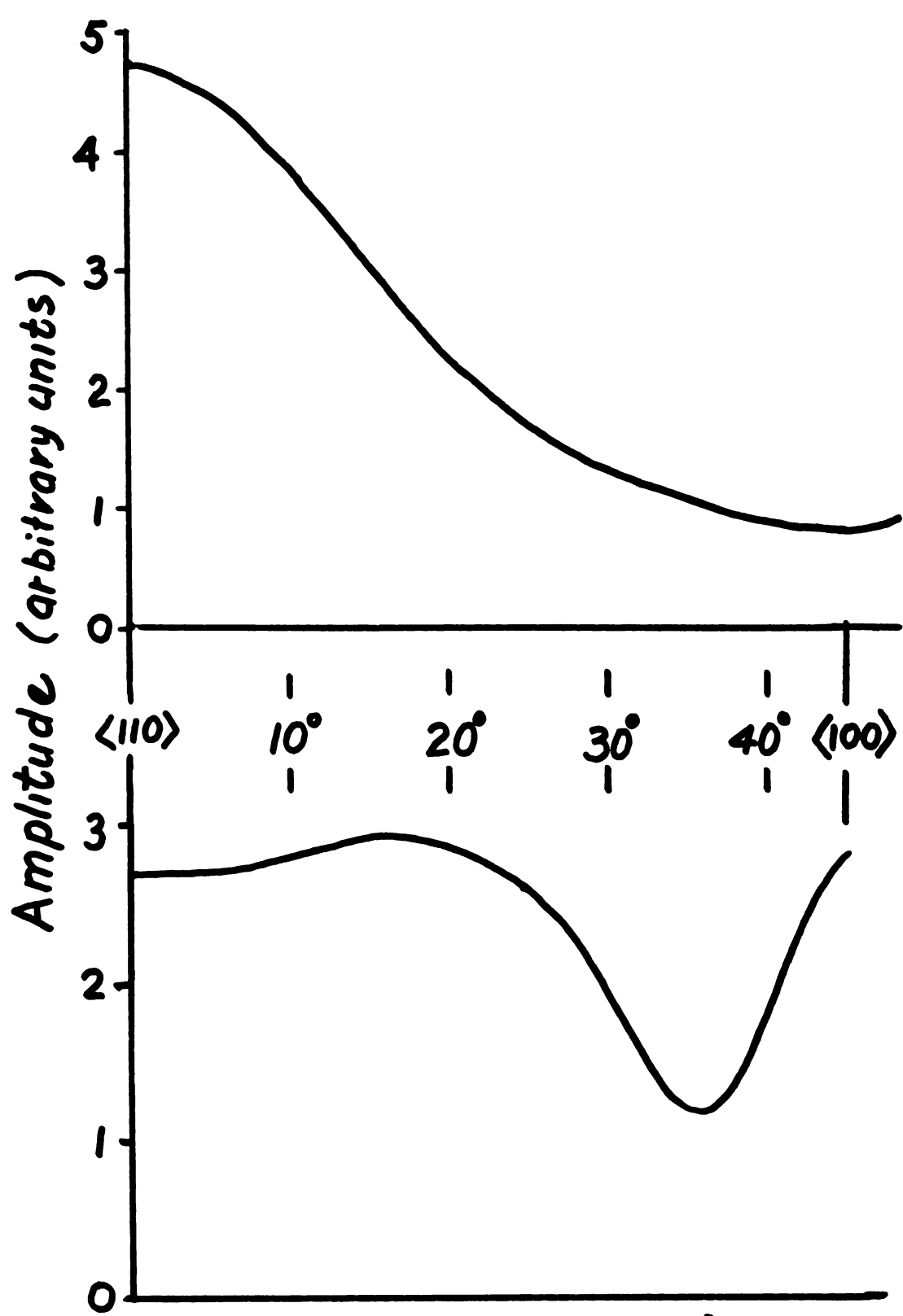


Fig. (7.6) Amplitude Dependence in the {100} Plane upper: High Frequency of Orbits lower: Low frequency of and of Orbits

angular dependence of the amplitude is due to anisotropies in g, m*, τ and I_4 , it could not be simply accounted for. In principle the effect of each of these parameters could be sorted out, though this would be a very difficult series of experiments to perform.

Field plots to obtain the Dingle temperatures as described in Section (4.6) were made for both the β and γ oscillations near $\langle 110 \rangle$. For some of the samples the Dingle temperature was determined at a series of temperatures between 1 and 2° K. Examples of the Dingle plots for high and low frequencies are shown in Fig. (7.7). The beating of the γ oscillations by the higher amplitude β ones is manifest in Fig. (7.7)A. The effect of the 2:1 beating of the γ by the γ oscillations is apparent in Fig. (7.7)B. Since in both cases the oscillations were followed over several cycles of the beat pattern this should have little effect upon the value of γ 0, which was measured. The results of the Dingle temperature measurements are shown in Table (7.1).

The measured Dingle temperature can be related to the lifetime $oldsymbol{\mathcal{T}}$ via

$$X_{D} = \pi/2\pi K_{B} \tau . \qquad (7.1)$$

The $\mathcal T$ as determined from Eqn. (7.1) is really very specific. It is the lifetime of a state corresponding

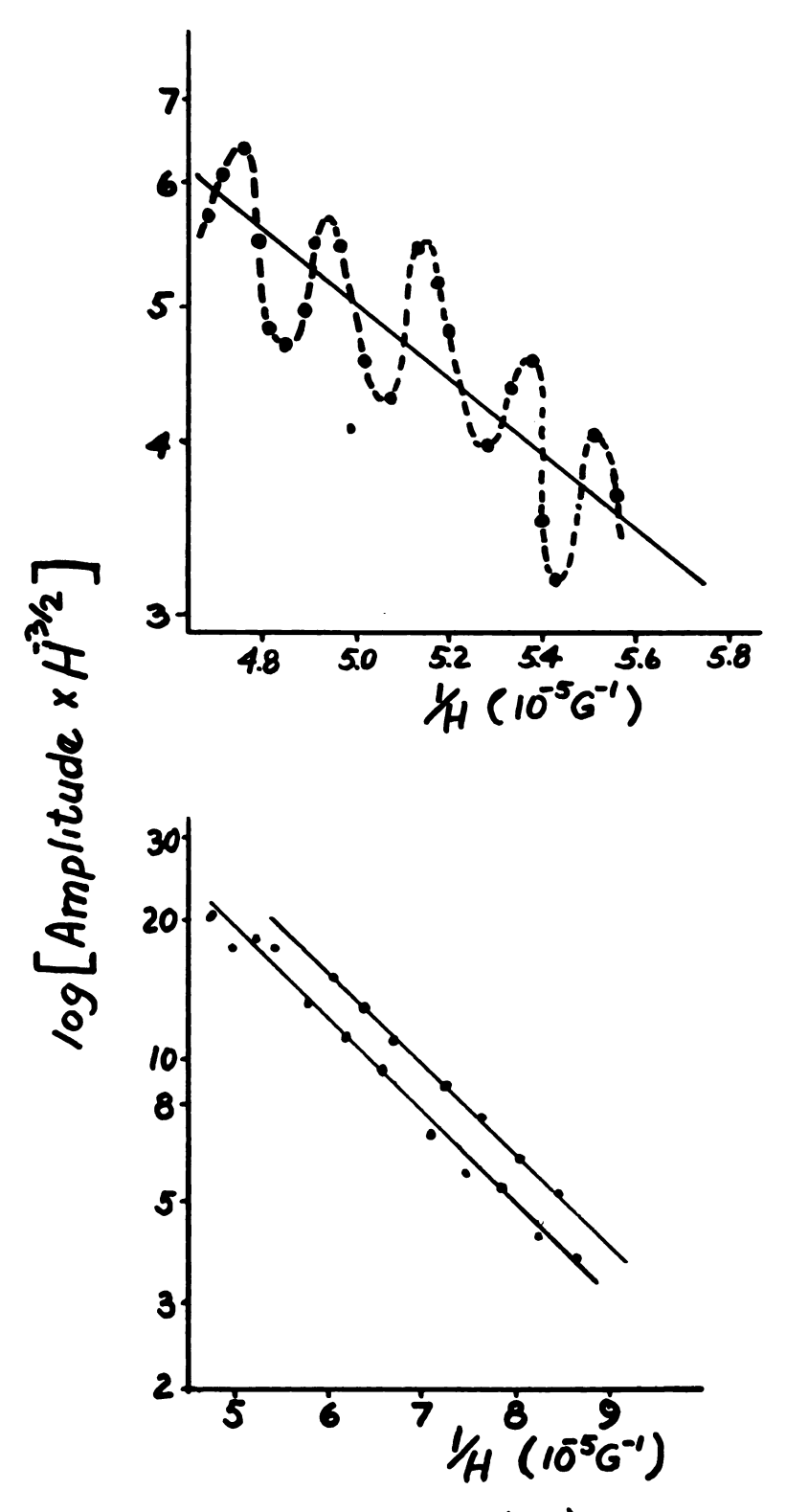


Fig. (7.7) Dingle Plots along (110)
upper: High Frequency (*) Oscillations
lower: Low Frequency Oscillations

Table (7.1) Dingle Temperature Results

alloy sample	· approximate frequency of oscillations and orientation	x _D (°K) *	temperature for measure- ment(^O K)
#1 .08 at.% Mg	5×10 ⁵ G 〈 110 〉	2.88	2.03
	(110)	2.62	1.73
		2.91	1.49
		2.80	1.41
		2.22	1.24
	3x10 ⁶ G ⟨ 110 ⟩	2.69	1.46
#2 .39 at.% Mg	5x10 ⁵ G ⟨ 110 ⟩	4.65	1.21
#7 .13 at.% Mg	5x10 ⁵ G	2.30	1.89
	〈 110 〉	2.37	1.72
		2.6	1.60
		2.5	1.45
	3x10 ⁶ (110)	3.2	1.89
		3.1	1.72
		3.8	1.61
		4.2	1.42

using m*/m = .118 for the $5 \times 10^5 \text{G}$ (110) osc. and .130 for the $3 \times 10^6 \text{G}$ (110) osc.

to an extremal orbit at the Fermi energy. Thus the ${\cal C}$ as measured gives very specific information about the scattering from one part of the Fermi surface. We can also calculate ${\cal T}_{\cal P}$ from the electrical resistivity ${\cal P}$.

$$\tau_{\rho} = m/ne^2 \rho \tag{7.2}$$

This is of course not the same \mathcal{T} as has been measured. \mathcal{T}_{ρ} of Eqn. (7.2) is the "average" lifetime of all the conduction electrons. It is composed not only of third zone states but also those states of the large second zone. The masses of these zones are respectively ~ 0.12 and ~ 1.3 free electron masses. Thus in considering an "average" m to use in Eqn. (7.2) it is probably not a bad approximation to use $m = m_0$, the free electron mass. Having measured the $\rho_{3000\text{K}}$ / $\rho_{4.20\text{K}}$ resistance ratio it is then a simple matter to calculate \mathcal{T}_{ρ} .

In the above-mentioned paper Brailsford calculated

$$\frac{\mathcal{T}}{\hat{\mathcal{I}}_{P}} = \frac{\int_{0}^{\pi} p(\theta) (1-\cos\theta) \sin\theta \, d\theta}{\int_{0}^{\pi} p(\theta) \sin\theta \, d\theta}.$$

 $P(\Theta)$ is the probability of scattering through an angle Θ . Considering a simple shielded coulomb potential

he obtained the result of Fig. (7.8).

The results of these calculations are compared with

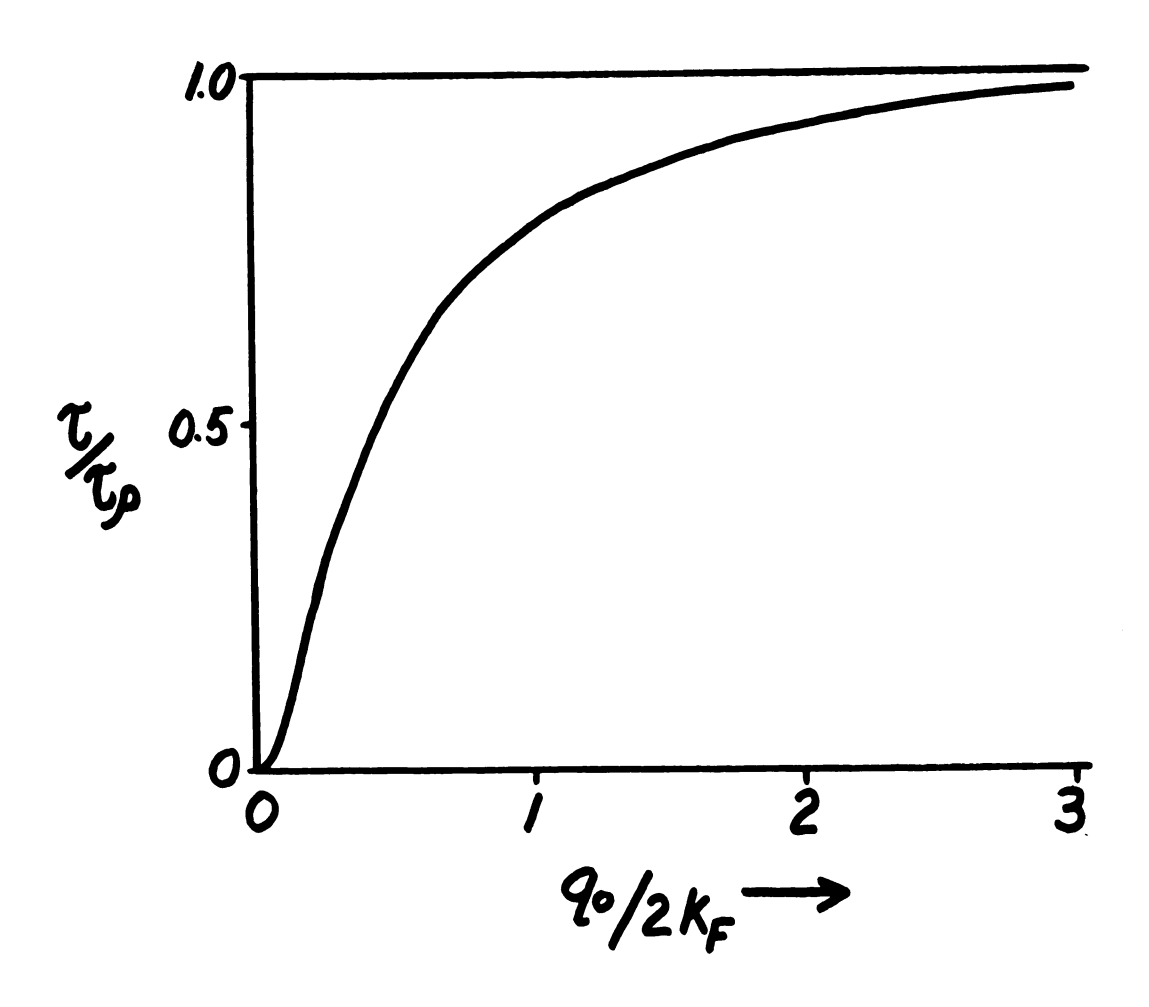


Fig. (7.8) Results of Brailsford's Scattering Calculation

the experimental values in Table (7.2). The increase of $\mathcal{T}/\mathcal{T}_{p}$ for high alloy concentrations shows that a more sophisticated scattering theory is probably necessary.*

By comparing the amplitude of the oscillations in a given field range at several temperatures we can study the temperature dependence of the amplitude. After correcting for the simple temperature dependence of the amplitude (i.e. $T/C_H\sqrt{1+(\frac{\tau \text{ osc}}{2\pi\tau_Q})^2}$) we would expect from Section (4.6) that

$$\Delta T_{\rm osc}$$
 amp $\frac{1-bT/H \coth bT/H}{\sinh bT/H}$ ($e^{\frac{-bX_D}{H}}$) $H^{3/2}$ (7.3)

Thus for fixed field we would expect the temperature to vary as

$$\frac{1-bT/H coth bT/H}{sinh bT/H}.$$

A family of constant field curves showing this temperature dependence of the amplitude is shown in Fig. (7.9) for the .08 at.% Mg sample. As we go successively to curves of higher field we would expect (from Eqn. (7.1)) the temperature of the maximum to increase proportionally. This behavior is seen in

^{*} If $\mathcal{T}/\mathcal{T}_{\mathcal{P}} <$.7 (the Thomas-Fermi value) then the 1% A1-Zn dHvA results of Gordon must have their amplitude at 17 KG reduced by a factor of \sim e⁻¹² relative to pure A1.

Table (7.2) Scattering Results <110>

at.%Mg	approximate frequency (10 ⁵ G)	(ok)	7 (10 ⁻¹³ sec)	RRR	ری (10 ⁻¹³ sec)	2/2/2
.08	5	2.8	4.3	106	7.4	.58
	30	2.7	4.5		7.4	.61
.13	5	2.5	4.8	66	4.6	1.07
	30	3.7	3.3		4.6	.72
.39	5	4.7	2.6	22	1.53	1.44

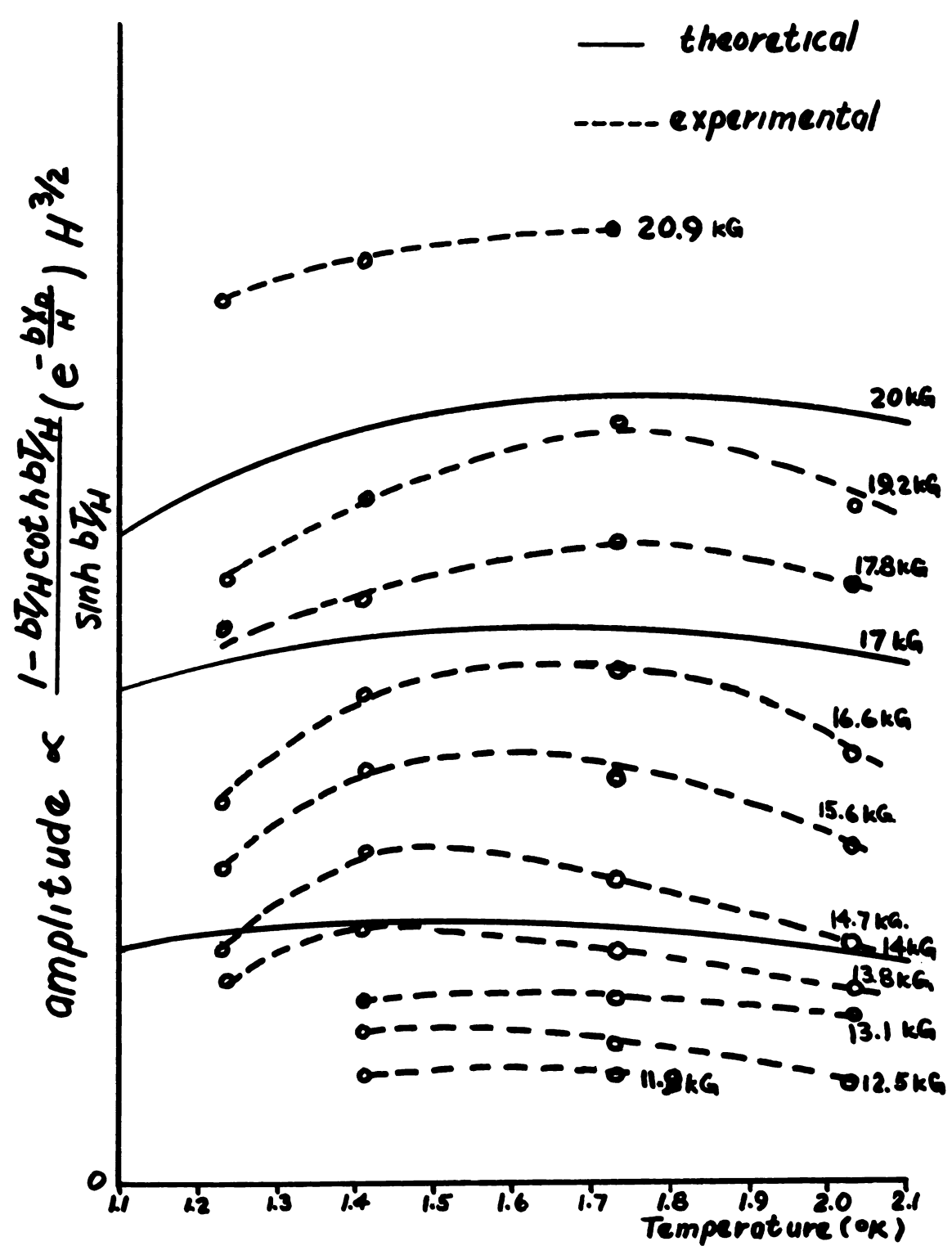


Fig. (7.9) Temperature Dependence of the MTO Amplitude

Fig. (7.9) although the maxima appear sharper than one would expect from the theory. Since the temperature of the amplitude maximum for a given field curve depends only upon the effective mass and fundamental constants we can obtain a value of m^*/m from each curve. m^*/m determined in this fashion varies from .104 to .121 with a mean of .113 . This value compares very favorably with $m^*/m \simeq .118$ calculated by Gordon⁶⁶ from the temperature dependence of the amplitudes (from dHvA data).

7.4 Amplitude Comparisons

From the theoretical expression for the MTO effect we can calculate the absolute amplitude of the fundamental oscillation.

$$\Delta T_{\rm OSC} = \frac{2K_{\rm B}T_{\rm O}H_{\rm O}^{3/2} (e/hc)^{3/2} e^{\frac{-bX_{\rm D}}{H}} (1 - \frac{bT}{H} \coth \frac{bT}{H})}{\left|\frac{\lambda^{2}A}{\partial k_{\rm Z}^{2}}\right|^{\frac{1}{2}} \exp \left(C_{\rm H} + \sqrt{1 + (\tau_{\rm OSC}/2\pi\tau_{\rm Q})^{2}} \sinh \frac{bT}{H}}$$
(7.4)

We make the initial assumptions:

 $C_{\rm H}$ is mainly electronic (i.e.~)T, 98% is in Al at $1^{\rm O}{\rm K}$),

$$\frac{1 - \frac{bT}{H} \coth \frac{bT}{H}}{\sinh \frac{bT}{H}}$$
 is in the constant region and therefore $=$.31,

Thus

$$\Delta T_{\text{osc}} = \frac{H^{3/2} e^{-bX_{\text{D}}}}{|Y|^{3/2} |X|^{\frac{1}{2}}} = 2.21 \times 10^{-14} \text{ o}_{\text{K}}$$

where H is in gauss

 δ is in ergs/mole deg²

 ρ is the mass density in gm/cm³

A is the atomic weight (e.g. \sim 27 for A1)

For Al using m*/m = .118 and H = 17KG,

$$\Delta T_{\rm osc} \simeq \frac{3.62 \times 10^{-4} \, \text{oK e}^{-X_{\rm D}}}{\left|\frac{\mathbf{d}}{\mathbf{d} k_{\rm Z}^2}\right|_{\rm ext}^{\frac{1}{2}}}$$
 (7.5)

To evaluate the denominator in Eqn. (7.5) we can use the angular variation of frequency data. Consider a piece of Fermi surface having cylindrical symmetry about some axis determined by the magnetic field. The radius of an orbit tipped at an angle Θ with respect to this axis is expanded as

$$r = r_0(1 + A \Theta^2)$$
.
The area $A(\Theta)_{ext} = \pi r_0^2(1 + A \Theta^2)$ (7.6)

At a distance $rsin \bullet$ along k_Z from the extremal orbit at $\bullet = 0$

$$A = \pi (r\cos \theta)^2 \simeq 1 - \theta^2 + 2 \triangleleft \theta^2.$$

It then follows that

$$\left|\frac{\frac{2}{3}A}{3k_Z^2}\right|_{\text{ext}}^{\frac{1}{2}} = \sqrt{4\pi} \left| \mathbf{x} - \frac{1}{2} \right|^{\frac{1}{2}} \tag{7.7}$$

Since for a cylinder \angle = $\frac{1}{2}$ we have

$$\frac{A(\Theta)-A_{\text{cylinder}}^{(\Theta)}}{A(\Theta=0)} = (A - \frac{1}{2})\Theta^{2}$$

from Eqn. (7.6).

For the Υ_1 orbits along $\langle 110 \rangle$ we can calculate $\angle -\frac{1}{2} \cong .097$. Thus from Eqn. (7.7) $\left| \frac{\partial 2_A}{\partial k_2^2} \right|^{\frac{1}{2}} = \sqrt{4\pi (.097)} = 1.10 .$

For these orbits there are two equivalent pieces of Fermi surface per Brillioun zone and thus

$$\Delta T_{\rm osc} \bigg|_{\Upsilon,(10)} = \frac{2(3.62 \times 10^{-4} \, {\rm o}_{\rm K}) \, {\rm e}^{-{\rm X}_{\rm D}}}{1.10} = 6.6 \times 10^{-4} \, {\rm o}_{\rm K} \, {\rm e}^{-{\rm X}_{\rm D}}$$
.

The corresponding measured amplitude for pure Al was $6.5 \pm 1 \times 10^{-40} \text{K}$.

The β and α orbits arise from regions of the Fermi surface near the junction of the arms. Since these pieces do not lie along $\langle 110 \rangle$ it is difficult to evaluate the shape factor

$$\left|\frac{\mathbf{\lambda}^{2}\mathbf{A}}{\mathbf{\delta}^{k}\mathbf{z}^{2}}\right|^{\frac{1}{2}} .$$

We would expect

$$\frac{1}{\left|\boldsymbol{\mathsf{J}}^2\mathbf{A}/\boldsymbol{\mathsf{J}}\,\mathbf{k_Z}^2\right|^{\frac{1}{2}}}$$

to be greater for these sections

than for a sphere where

$$\frac{1}{\left|\partial^2 A/\partial k_Z^2\right|^{\frac{1}{2}}} = \frac{1}{\sqrt{2\pi}} \approx .4$$

We thus find for the $5x10^5$ G frequency along $\langle 110 \rangle$

$$\Delta T_{\rm osc} > 1.75 \times 10^{-30} \text{K}$$
.

The corresponding measured amplitude is $4.35 \times 10^{-30} \text{K}$.

We can also compare the relative amplitudes of the alloys as determined from their measured Dingle temperatures. This comparison, made at fixed temperature and field, is shown in Table (7.3).

Table (7.3) Amplitude Comparison $\langle 110 \rangle$

at.%Mg	approximate frequency (10 ⁵ G)	measured $ \Delta T_{\rm osc} (^{\rm O}{\rm K}) $	(ok)	Dingle factor amplitude reduction	-
pure	5	4.35x10 ⁻³	0	1	1
	30	.65×10 ⁻³	0	1	1
.08	5	3.65x10 ⁻⁴	2.8	<u>1</u> 17	<u>1</u> 13
·	30	.4x10 ⁻⁴	2.7	<u>1</u> 21	<u>1</u> 16
.13	5	4.6x10 ⁻⁴	2.5	<u>1</u> 12	9.5
	30	1.5x10 ⁻⁵	3.7	<u>1</u> 64	$\frac{1}{45}$
.39	5	1.2x10 ⁻⁴	4.65	105	<u>1</u> 36

		;

CHAPTER VIII

GENERAL CONCLUSIONS

These measurements of the third zone Fermi surface of pure aluminum and dilute aluminum-magnesium alloys show that the extremal cross-sectional areas along (110) and (100) decrease as the concentration of magnesium is increased. The electron nature of this surface is thus verified. A simple free electron perturbation of the model proposed by Ashcroft can be used to explain these changes. In particular the cross-sectional areas corresponding to a frequency of about $5x10^5$ G where a fairly substantial decrease in area is observed (~10%) fit the model quite well. (Fig. (7.2)) The higher frequency oscillations appear to be more dependent upon the alloying than would be expected from the model. Uncertainties in the high frequency pure aluminum frequencies of about 2% could account for most of this discrepancy.

The MTO technique has been used to study the variation in both the amplitude and frequency as the magnetic field is rotated relative to the crystal.

Although the amplitude variation is difficult to

interpret it was possible to measure the angular variation of the % orbit very thoroughly.

The variation of the amplitude of the oscillations with both temperature and magnetic field was also studied. The different hyperbolic dependence of the MTO and dHvA oscillations enables one to determine the effective mass more directly with the dHvA measurement. A technique which enables the MTO effect to be used to measure Dingle temperatures has been developed. This technique takes advantage of the relatively small dependence of the MTO amplitude upon the hyperbolic T/H term. Dingle temperatures determined using this method agree qualitatively with those obtained from the electrical resistivity. The effective mass measured along $\langle 110 \rangle$ for the low frequency (5x10⁵G) was found to be $m*/m = .113 \pm .008$, in agreement with the value measured by Gordon of .118.

The absolute amplitude, which could be calculated quite accurately for the % oscillations, was found to agree with the measured value to within the experimental error of about 15%.

A crude amplitude calculation for the low frequency oscillations also agreed with experiment.

The latter comparison cannot be considered a rigorous test of the theory because of the difficulty involved in evaluating the shape factor for this part of the Fermi surface.

The absolute amplitude of the alloys was found to scale approximately as expected from the Dingle factor. The actual reduction in amplitude was in all cases less than would be expected from the Dingle theory. Effective Dingle temperatures determined from the scaling of the amplitudes of the alloys relative to pure Al are 10 to 20% less that the actual Dingle temperatures measured for each alloy.

BIBLIOGRAPHY

- 1. W.J. deHaas and P.M. van Alphen, Leiden Comm. 208d, 212a (1930), 220d (1933).
- 2. J.H. Condon and J.A. Marcus, Phys. Rev. <u>134</u>, A446 (1964).
- D. Shoenberg and P.J. Stiles, Proc. Roy. Soc. <u>281A</u>,
 62 (1964); Phys. Letters <u>4</u>, 274 (1963).
- 4. D. Shoenberg, Phil. Trans. Roy. Soc. (London) <u>A255</u>, 85 (1962).
- 5. L.R. Windmiller and M.G. Priestly, Solid State Comm. 3, 199 (1965).
- 6. R.W. Stark, The Simon Fraser University Lectures on Solid State Physics I, edited by J.F. Cochran, R.R. Haering (Gordon and Breach, New York, 1968).
- 7. A. Goldstein, S.J. Williamson, and S. Foner, Rev. Sci. Instr. 36, 1356 (1965).
- 8. J.E. Kunzler, F.S.L. Hsu, and W.S. Boyle, Phys. Rev. 128, 1084 (1962).
- 9. F.J. Blatt, M. Garber, J. LePage, Low Temperature Physics LT9B (Plenum Press, New York, 1965).
- 10. B. McCombe and G. Seidel, Phys. Rev. <u>155</u>, 633 (1967).
- 11. L. Shubnikov and W.J. deHaas, Comm. Phys. Lab. Univ. of Leiden, 207, 210 (1930).
- 12. R.N. Bhargava, Phys. Rev. <u>156</u>, 785 (1967.
- 13. J.A. Woollam, Dissertation, Michigan State University (1967).
- 14. C.G. Grenier, J.M. Reynolds, and N.H. Zebouni, Phys. Rev. 129, 1088 (1963); J.R. Long, C.G. Grenier, and J.M. Reynolds, Phys. Rev. 140, 187 (1965); C.G. Grenier, J.M. Reynolds, and J.R. Sybert, Phys. Rev. 132, 58 (1963).

- 15. Y. Shapira and B. Lax, Phys. Rev. 138, 1191 (1965).
- 16. V.F. Gantmakher, Soviet Phys.-JETP 15, 982 (1962);
 V.F. Gantmakher and E.A. Kaner, Soviet Phys.-JETP 18, 988 (1964); V.F. Gantmakher and I.P. Krylov, Soviet Phys.-JETP 22, 734 (1966).
- 17. A.B. Pippard, Phil. Mag. 2, 1147 (1957).
- 18. G.N. Kamm and H.V. Bohm, Phys. Rev. 131, 111 (1963).
- 19. M.H. Cohen, M.J. Harrison, and W.A. Harrison, Phys. Rev. 117, 937 (1960).
- 20. J.B. Ketterson and Y. Eckstein, Rev. Sci. Instr. 37, 44 (1960).
- 21. M. Ya. Azbel' and E.A. Kaner, Soviet Phys.-JETP 3, 772 (1956); Soviet Phys.-JETP 5, 730 (1957).
- 22. I.M. Lifshitz and V.G. Peschanskii, Soviet Phys.-JETP 8, 875 (1959); Soviet Phys.-JETP 11, 137 (1960).
- 23. E. Fawcett, Adv. Phys. 13, 139 (1964).
- 24. V. Heine, Proc. Phys. Soc. (London) 694, 505 (1956).
- 25. A.D. Brailsford, Phys. Rev. 149, 456 (1966).
- 26. J.E. Schirber, Physics of Solids at High Pressure, ed. C.T. Tomizuka and R.F. Emrick (Academic Press Inc., New York, 1965).
- 27. J.R. Anderson, W.J. O'Sullivan, J.E. Schirber, and D.E. Soule, Phys. Rev. <u>164</u>, 1038 (1967).
- 28. A.B. Pippard, Proc. Roy. Soc. (London) 270A, 1(1962).
- 29. R.W. Stark, Phys. Rev. Letters <u>9</u>, 482 (1962).
- 30. R.J. Higgins and J.A. Marcus, Phys. Rev. <u>141</u>, 553 (1966).
- 31. J.C. Slater, Advances in Quantum Chemistry I (Academic Press, New York, 1964) p. 35.
- 32. T.L. Loucks, Augmented Plane Wave Method (W.A.

- Benjamin, Inc., New York, 1967).
- 33. W.A. Harrison, Pseudo-potentials in the Theory of Metals (W.A. Benjamin, Inc., New York, 1966).
- 34. J.C. Slater, Phys. Rev. 145, 599 (1966).
- 35. J.M. Ziman, Proc. Phys. Soc. (London) 86, 337(1965).
- 36. Tanuma, Tshizawa, Nagasawa, Sugawara, Phys. Letters 25A, 669 (1967).
- 37. W.J. deHaas and P.M. Van Alphen, Proc. Amsterdam Acad. 33, 1106 (1930).
- 38. N. Bohr, Dissertation, Copenhagen (1911).
- 39. L. Landau, Zets. fur Phys. 64, 629 (1930).
- 40. D. Shoenberg, Proc. Roy. Soc. <u>170A</u>, 341 (1939).
- 41. L. Onsager, Phil. Mag. <u>43</u>, 1006 (1952).
- 42. I.M. Lifshitz and A. Kosevitch, Soviet Phys.-JETP 29, 730 (1955).
- 43. R.B. Dingle, Proc. Roy. Soc. (London) <u>A211</u>, 517 (1952).
- 44. S.J. Williamson, S. Forner and R.A. Smith, Phys. Rev. <u>136A</u>, 1065 (1964).
- 45. A.D. Brailsford, Phys. Rev. 149, 456 (1966).
- 46. R.B. Dingle, Proc. Roy. Soc. (London), <u>A211</u>, 500 (1952).
- 47. M.H. Cohen and E.I. Blount, Phil. Mag. <u>5</u>, 115 (1960).
- 48. M.H. Halloran, F.S.L. Hsu, and J.E. Kunzler, Bull. Am. Phys. Soc. 13, 59 (1968); and comment by L.R. Windmiller.
- 49. R.E. Prange and L.P. Kadanoff, Phys. Rev. <u>134</u>, 566 (1964).
- 50. D. Pines, Elementary Excitations in Solids (W.A. Benjamin, Inc., New York, 1964).

- 51. J.W. Wilkins and J.W.F. Woo, Phys. Letters <u>17</u>, 89 (1965).
- 52. A.B. Pippard, Proc. Roy. Soc. (London) <u>272A</u>, 192 (1963).
- 53. D. Shoenberg, Phil. Trans. Roy. Soc. (London) 255A, 85 (1962).
- 54. J.H. Condon, Phys. Rev. 145, 526 (1966).
- 55. J. LePage, Dissertation, Michigan State University (1965).
- 56. J.C. Abele and H.J. Trodahl (to be published).
- 57. W.L. Gordon, Phys. Rev. 126, 489 (1962).
- 58. G.A. Philbrick Researches, Inc., Applications Manual for Computing Amplifiers (Nimrod Press Inc., Boston, 1966).
- 59. W.G. Pfann, Zone Melting (John Wiley and Sons, Inc., New York, 1958).
- 60. W.A. Harrison, Pseudo-potentials in the Theory of Metals (W.A. Benjamin, Inc., New York, 1966)p. 150.
- 61. V. Heine, Proc. Roy. Soc. (London) 240A, 340 (1957).
- 62. A.V. Gold, Phil. Trans. Roy. Soc. (London) <u>A251</u>, 85 (1958).
- 63. W.A. Harrison, Phys. Rev. <u>116</u>, 555 (1959).
- 64. E.M. Gunnerson, Phil. Trans. Roy. Soc. (London) 249A, 299 (1957).
- 65. N.W. Ashcroft, Phil. Mag. 8, 2055 (1963).
- 66. private communication mentioned in Ashcroft (1963) and later published; C.O. Larson and W.L. Gordon, Phys. Rev. 156, 703 (1967); J.P.G. Sheperd, C.O. Larson, D. Roberts, and W.L. Gordon, Low Temperature Physics LT9B (Plenum Press, 1965).
- 67. E.P. Vol'skii, Soviet Phys.-JETP 19, 89 (1964).

68. G.N. Kamm and H.V. Bohm, Phys. Rev. <u>131</u>, 111 (1963).

APPENDIX A

Heat Input via the Rotating Gear Mechanism

The heat input to the sample holder via the rotating gear mechanism is the result of two different effects: heat conducted down the control rods and frictional heating during the turning of the gears. Because the sample holder is located in a vacuum chamber and thermally isolated from the helium bath these heating effects are particularly troublesome. The situation is shown in Fig. (A.1).

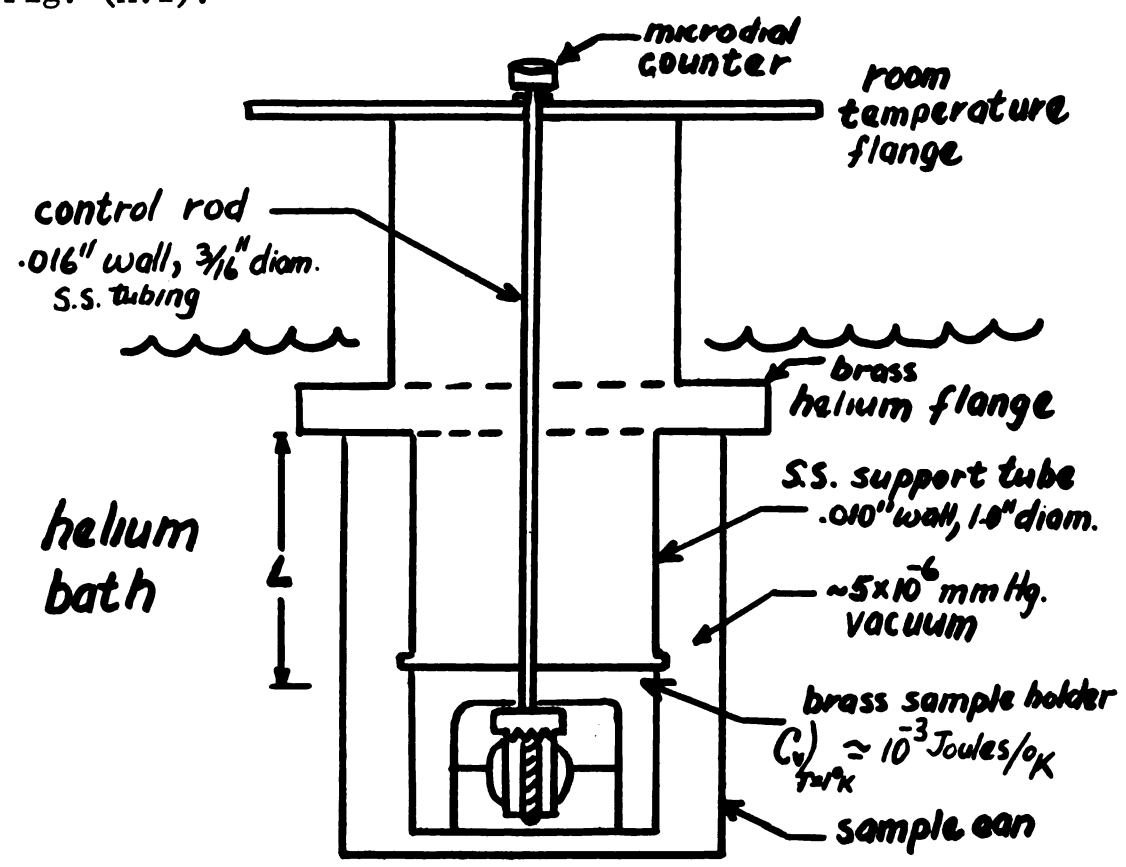


Fig. (A.1) Extraneous Heating Effects

For each of the control rods operating between 300° K and 4° K the heat flow per second is about 2.5×10^{-2} watts.

If we consider a copper wire thermal leak of length L, cross-sectional area A and conductivity K the temperature rise is about

$$\Delta T \simeq \frac{P_{\text{ower L}}}{R} \simeq 5 \times 10^{-3} \frac{L}{A} \text{ cm}^{\text{o}} \text{K}$$

To turn the control rods requires a torque of about 1 inch-ounce or $7x10^{-3}$ newton-meters. Thus for one complete revolution of these shafts, corresponding to a few degree change in the gears, about $4x10^{-2}$ joules of work must be done. If this energy all goes into frictional heating of the gears during a period of 15 seconds the temperature rise will be,

$$\Delta T_{rot} \simeq \frac{PL}{KA} \simeq .5 \times 10^{-2} \frac{L}{A} \text{ cm}^{O} \text{K}$$

where K \sim .5 joules/cm sec $^{\rm O}$ K . The time constant for returning to the equilibrium temperature is

$$rac{C_VL}{KA} \approx 2x10^{-3} \frac{L}{A} \text{ sec-cm}$$

Since the length L is about 30 cm and a reasonable A is about 1×10^{-2} cm² (i.e. #17 wire), L/A is about 3×10^{3} cm⁻¹, giving $\Delta T \sim 15^{\circ}$ K. It became obvious in

early experiments that another type of heat leak was necessary. A helium pillbox was soldered to the bottom of the sample holder thus reducing L to about 2 cm. Since glastic rod has a much lower thermal conductivity than stainless steel at room temperature ($\frac{1}{100}$) a 30 cm section of this was incorporated in the higher temperature regions of each control rod. The control rods were brought in thermal contact with the bath at the helium flange by wrapping copper wire around each and attaching this wire to the flange. With these modifications the conduction heating effect is less than 10⁻³oK as measured using the carbon resistors with either ~ 100 microns of helium exchange gas in the sample can or a good vacuum. The thermal time constant from rotating the gears is about 1 sec.

APPENDIX B

Crush-Type Lead O-Ring Seals

This particular type of lead seal was introduced to our laboratory by M. Garber. A possible seal is shown in Fig. (B.1).

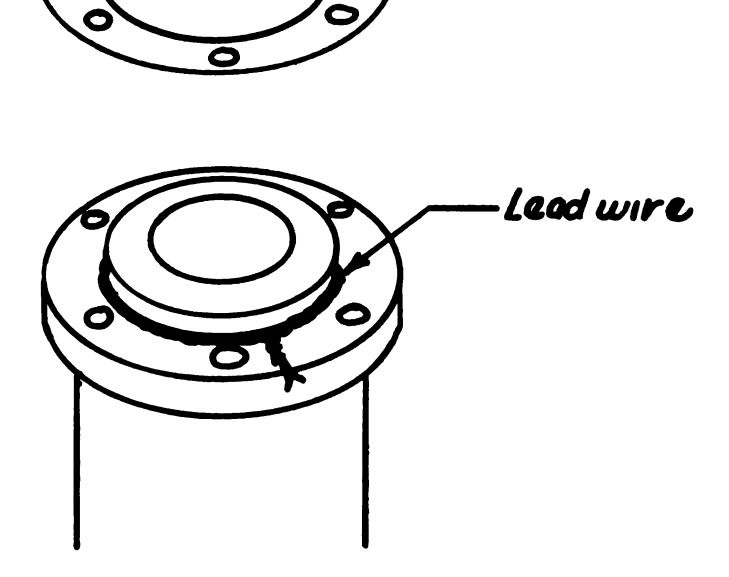


Fig. (B.1)

A lead wire of diameter ~.02 inches is greased lightly with Apiezon M lubricant, wrapped around the flange and twisted tightly. When the flanges are clamped together a simple but very reliable vacuum seal is formed. When these seals were used in the present

apparatus no failures were encountered even upon repeated thermal cycling between 1 and $300^{\rm o}{\rm K}$.

	1
	1
	1
	į
	, ,
•	
	1
	,
	,

 $\label{eq:APPENDIX C} \mbox{Differential Thermal Bridge Schematic}$

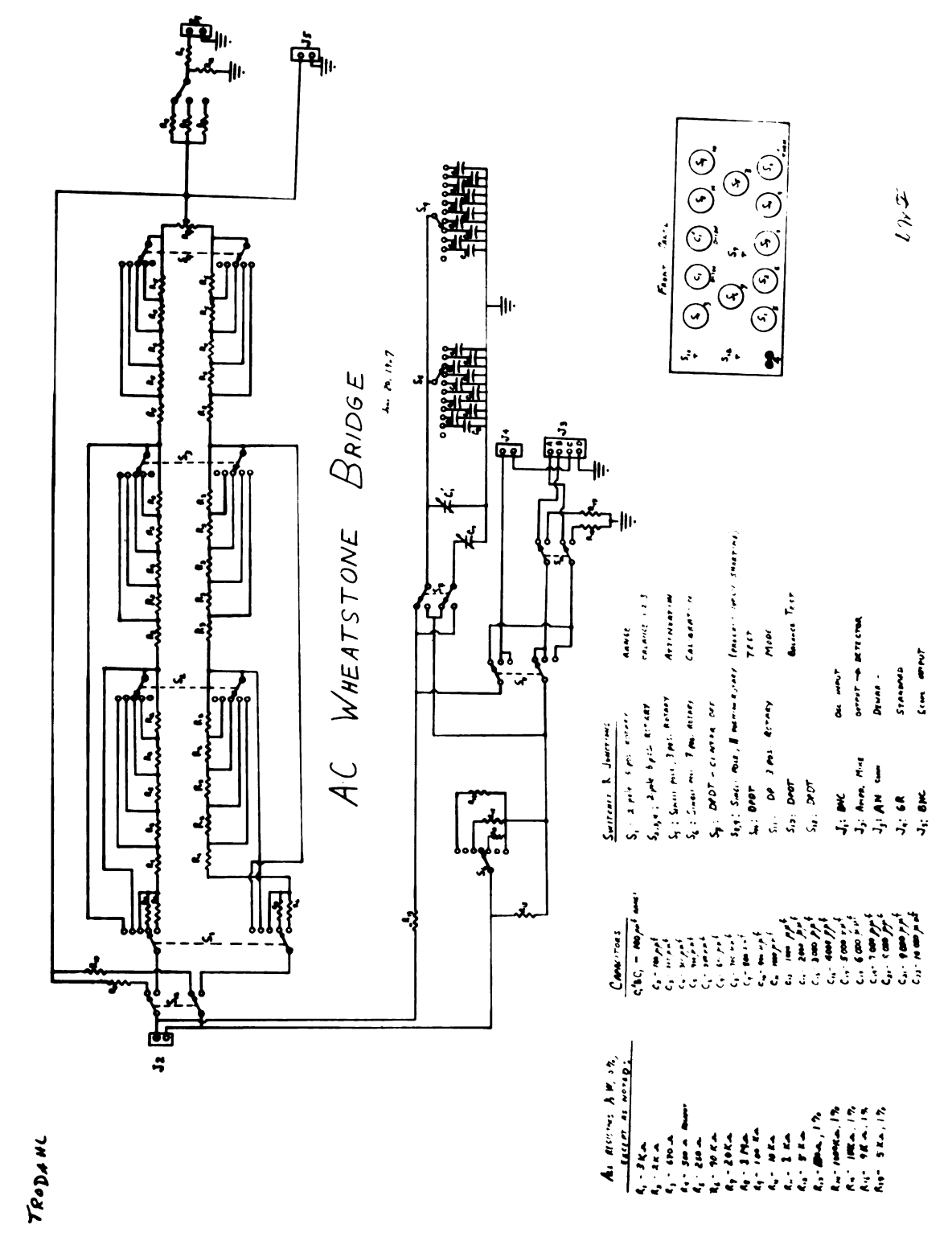


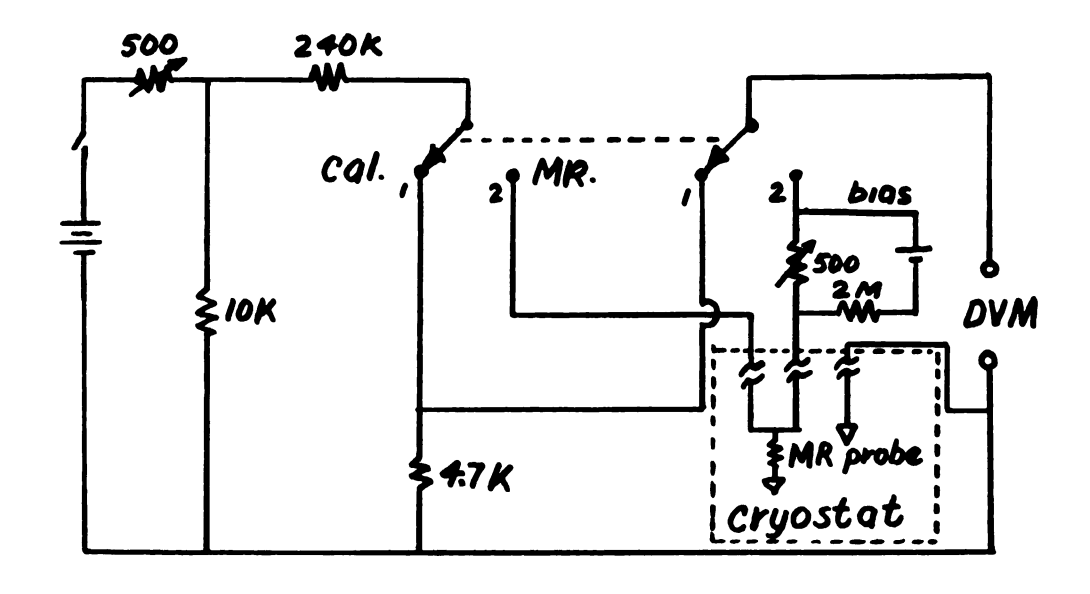
Fig. (C.1) Differential Thermal Bridge Schematic

APPENDIX D

Magneto-resistance Probe

The magneto-resistance probe which was referred to in Sec. (4.4) was examined as a means of monitoring the magnetic field. Since it is useful to have continuous measure of the field available a simple power supply to accomplish this was built. This circuit is shown in Fig. (D.1)A.

The current through the probe varies by up to 2% when the resistance of the probe changes from 100Ω to $5\kappa\Omega$. This is unimportant however, since the magneto-resistance is not linear anyway. Once a calibration has been made the circuit can be re-zeroed by maintaining the voltage across the 4.7K resistor constant. The drift in this voltage is only a few parts in 10^4 during an 8 hour period. The bias circuit is used to buck out thermal voltages which also amount to a few parts in 10^4 for the magnetic fields of interest. A calibration of this probe is shown in Fig. (D.1)B.



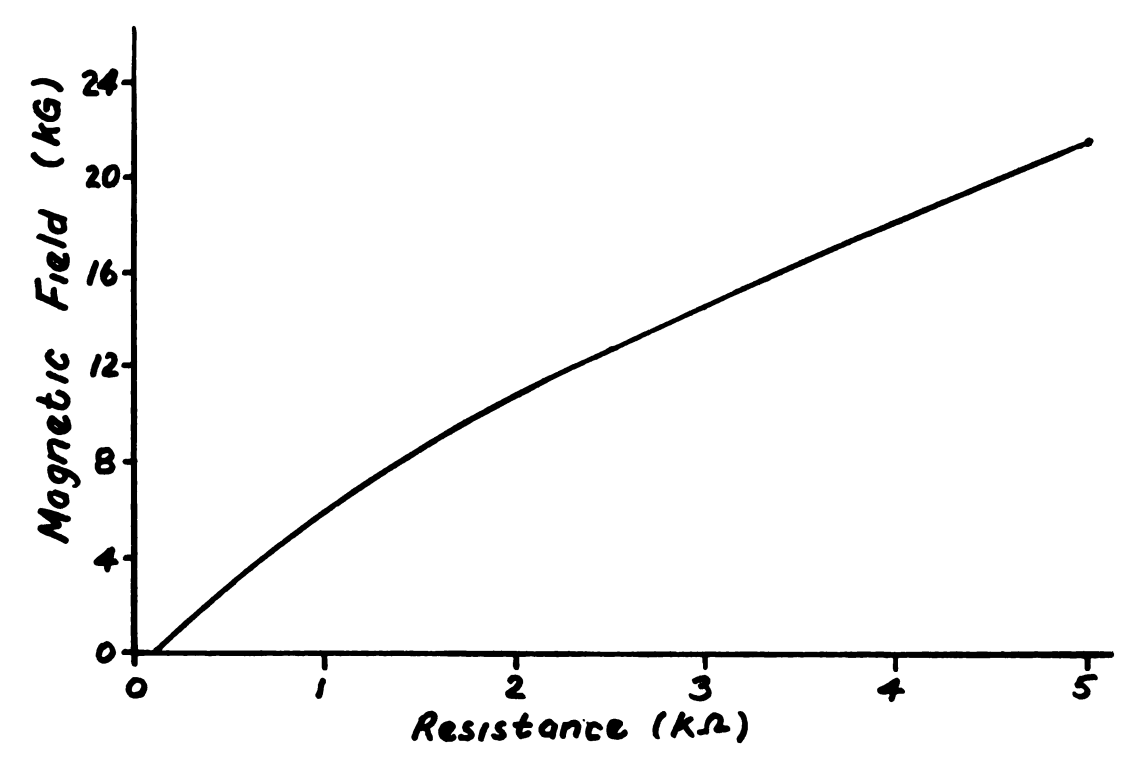


Fig. (D.1) Magneto-resistance Probe upper: Power Supply Circuit lower: Magnetic Field Calibration

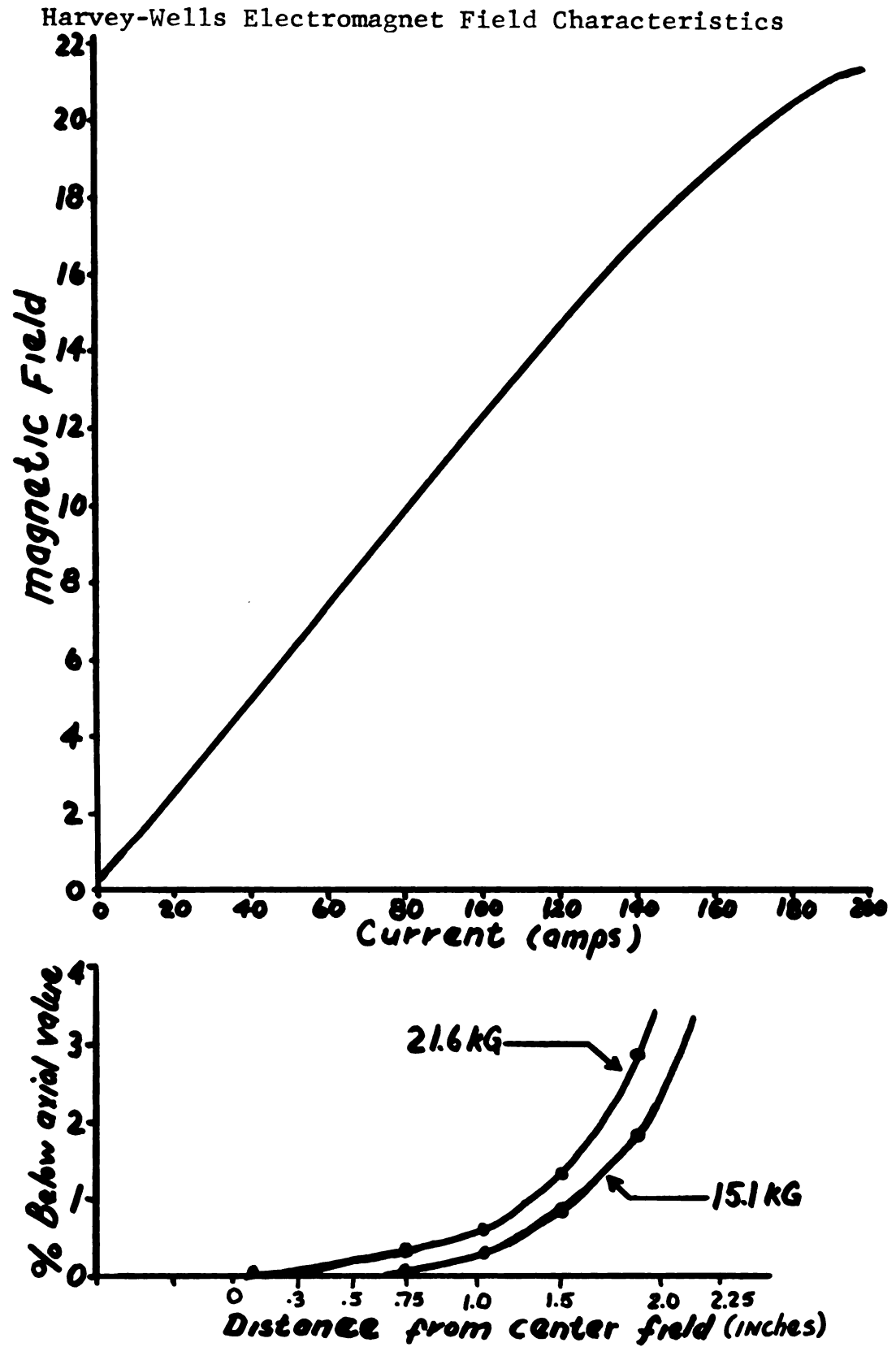


Fig. (E.1) Harvey-Wells Electromagnet Field Characteristics upper: Field versus Current Relationship lower: Field Profile Perpendicular to Field Axis and Equidistant from Pole Faces

APPENDIX F

Squaring Circuit for $\frac{1}{H}$ Sweep

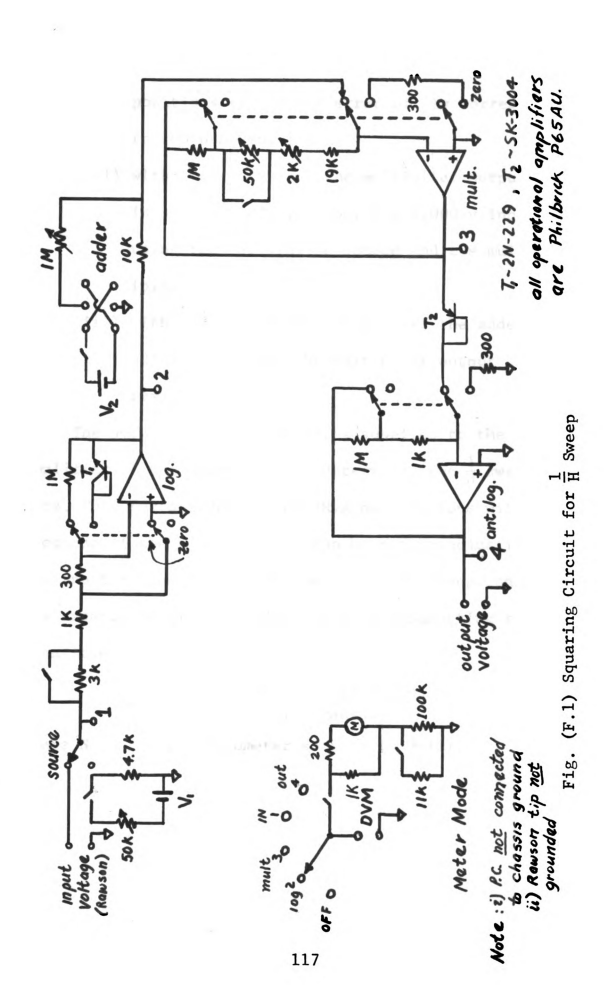
For the magnetic sweep control to maintain $\frac{1}{H} \ll t$ an external reference $\ll H^2$ is necessary. A circuit which provides arbitrary powers between about 1 and 5 of an input voltage over three decades of output is described. This circuit is shown in Fig. (F.1). Approximately thirty transistors were checked to determine their logarithmic properties.

For the present studies the field reference was obtained from a rotating coil gaussmeter*. Because the reference voltage for the sweep must be floating it is necessary to keep from grounding the tip of the gaussmeter on magnet pole faces or connecting the power common of the amplifiers and their power supply to any fixed grounds (e.g. racks or chassis).

For the transistors currently employed in the $\frac{1}{H} \ll$ t sweep circuit an error of less than 1/2% in $\frac{1}{H}$ was measured for sweeps between 9 and 22 KG. The circuit parameters were initially adjusted as follows:

i) using the meter mode switch all amplifiers

Rawson-Lush model 720



are zeroed and returned to their "operate" positions (a zeroing error of .1v corresponds to 100 nanoamps)

- ii) with the adder off, the multiplier output
 is set to 2.370 v output for 1.000 v input
 using the calibration source and the mult iplier potentiometer(s)
- iii) with the calibration source off the adder is adjusted so that the multiplier output reads -.190v

The amount of H^2 signal being supplied to the error amplifier of the sweep control determines the $\frac{1}{\mathrm{H}}$ sweep rate. Thus for a given set of dHvA oscillations with frequency f their time period can be set by adjusting the input attenuator potentiometer of the sweep control. The experimentally determined relation connecting these quantities is:

where N is the potentiometer setting (0 \Rightarrow 10).

APPENDIX G

Least Squares Program for Finding Frequencies

```
PROGRAM LINEIT
    LST SORS LIN REGRESS PERIOD UNCERT IS 95 0/0 CT
    DIMENSION A(80), B(80), H(3)
   TREAD 1000, KMAX, (H(J).J=1,3)
1000 FORMAT(110,348)
    PRINT 1001, (H(J), J=1,3)
1001 FOR 4AT(1H1.20X,3A8)
    DO 1170 J=1,KMAX
    READ 1002,K,N
1002 FORMAT (215)
    READ 1003, (A(I), I=1, N)
1003 FORMAT (8F10.))
     DO 1130 I=1.N
1130 R(1) = 1.0/A(1)
     AN = W
     XSJ1 = 0.
     YSJM = 0.
     XSOR = 0.
     YSOR = 0.
    DU 1140 1 = 1,N
    BI = 1
    XSUM = XSUM + BI
1140 YSJM = YSUM + B(I)
    XMEAN = (XSUM)/AN
    YMEAN = (YSUM)/AN
    XVARN = U.
     YVARN = 0.
     XYPRODV = n.
     D0 1150 I = 1.N
    8I = I
     XVARN = XVARN + (BI - XMEAN)**2
    YVARM = YVARN + ( B(1) - YMEAN ) ++2
1100 XYPRODN = XYPRODN + RI * B(I)
     XVAR = XVARN/AN
     YVAR = YVARNIAN
     XYPROD = XYPRODN/AN
     SLOPE = (XYPROD = XMFAN*YMEAN)/XVAR
    AREAG = 100000,7SLOPF
     PRINT 1004.K
1004 FURMAT (////10X.*FRFQ. IDENT, NO.*, 110)
     PRINT 1007
1007 FORMAT (/10X, +PEAK NO.+, 15X, +YERR+/)
     VARYN = 0.
    00 1160 1 = 1.N
     BI = [
     YERR = SLOPE+(BI-XMEAN) + YMEAN - B(I)
     VARYN = VARYN + YERR**2
    TVARY = VARYNIAN
```

Fig. (G.1) Program Listing

```
1150 PRINT 1008.I. YERR
1008 FORMAT (13Y, I2, 18X, E11.4)
PRINT 1005 , AREAG

1005 FORMAT (/10X, *FREQ. OF OSC. *.E11.4,* GAUSS*)
TCOEFF = SORTF((AN - 2.)*XVAR/VARY)
PERD = SLOPE/100000.
FRR = 2.1/( TCOEFF*100000.)
PRINT 1100, PERD, FRR

1100 FORMAT (/10X, *PERIOD OF OSC. *.E11.4,* * - *.E9.2,* G-1*)
PRINT 1006, VARY, N

1006 FORMAT(/10X, *VARIANCE = *, E11.4 , //.

1 10X, *NUMBER OF PEAKS = *, I5)

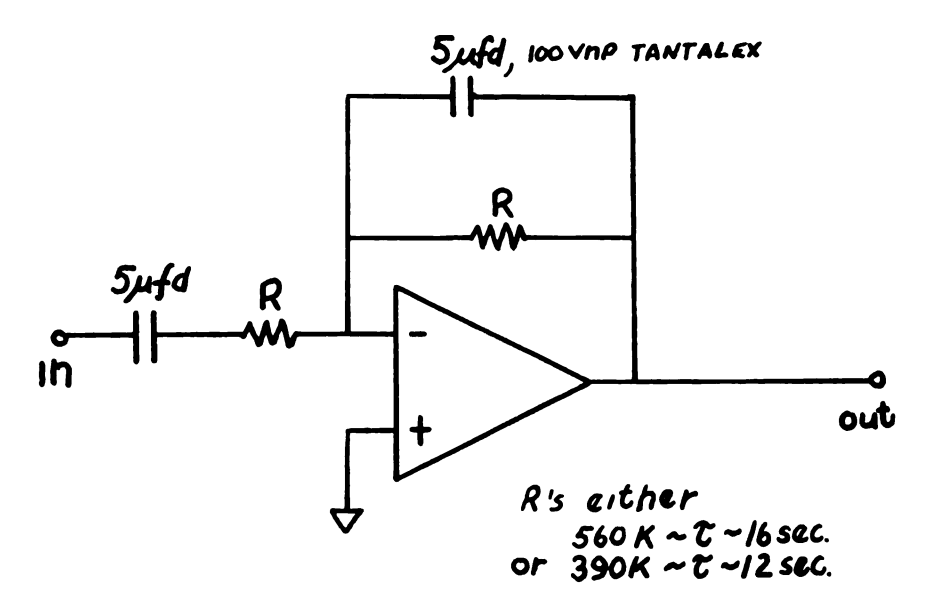
11/0 CONTINUE
END
```

Fig. (G.2) Program Listing, Continued

FREQ. IDENT. NO	1.0
PEAK NO.	YFRR
1	4,1554-003
2	2,8527-004
3	2.8808-003
4	
5	2.5532 - 005
6	1,2968-003
7	-1,1189-003
8	-7.0539-004
9	-7,2902-004
10	-1,1818-003
12	-2.0558-003 -3.3434-003
13	-2.0330-003
7.0	
1 4	4 4 0 4 4 2 0 0 7
15	-1,1964-003 2,0990-003
16	-9.0811-004
17	-1,4386-003
18	-2,4075-003
19	-3,8063-003
20	-2,8845-003
21	2,5505 - 004
22	-2.4864-003
23	-3,5958-004
24	1,2385-003
25 26	2,3191-003 2,8932-003
27	2,9713-003
28	2.5637-003
<u>2</u> 9	1,6806-003
30	2,7146-003
31	3,2255-003
32	9.0982-004
33	4,4114-004
34	-2.7698-003
35	-4,1781-003
FREQ. OF OSC.	-2.8606+006 GAUSS
PERIOD OF OSC.	-3.4957-007 + - 8.08-010 G-1
TARTANCETETT	4:9829•00A
NUMBER OF PEAKS	35

Fig. (G.3) Typical Output

Filter Circuits



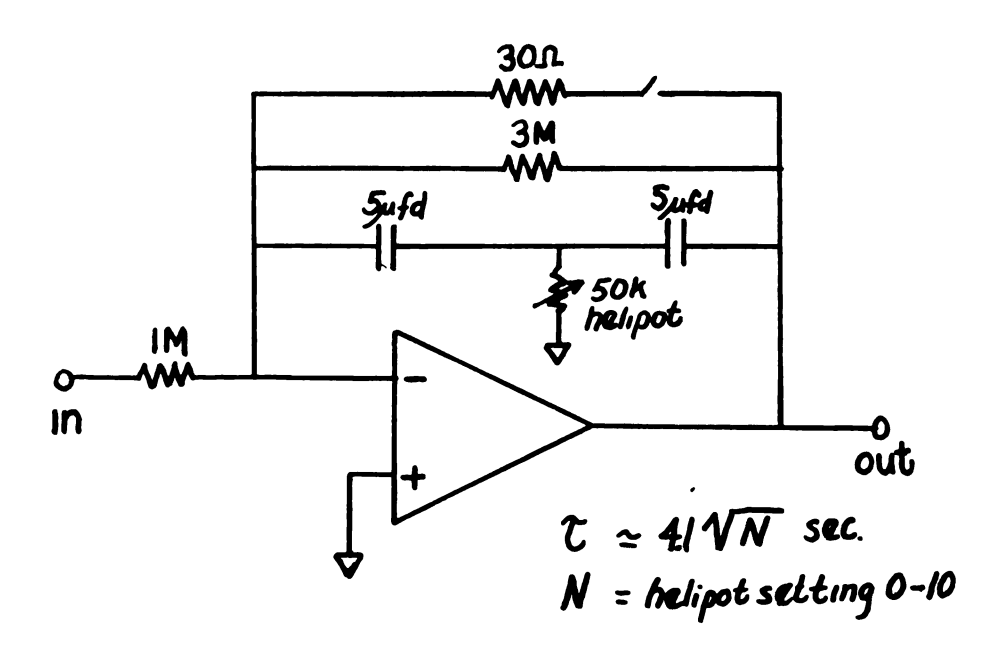


Fig. (H.1) Filter Circuits

upper: Wide Band Integrator-Differentiator

Filter

lower: Narrow Band Bridged-tee Filter

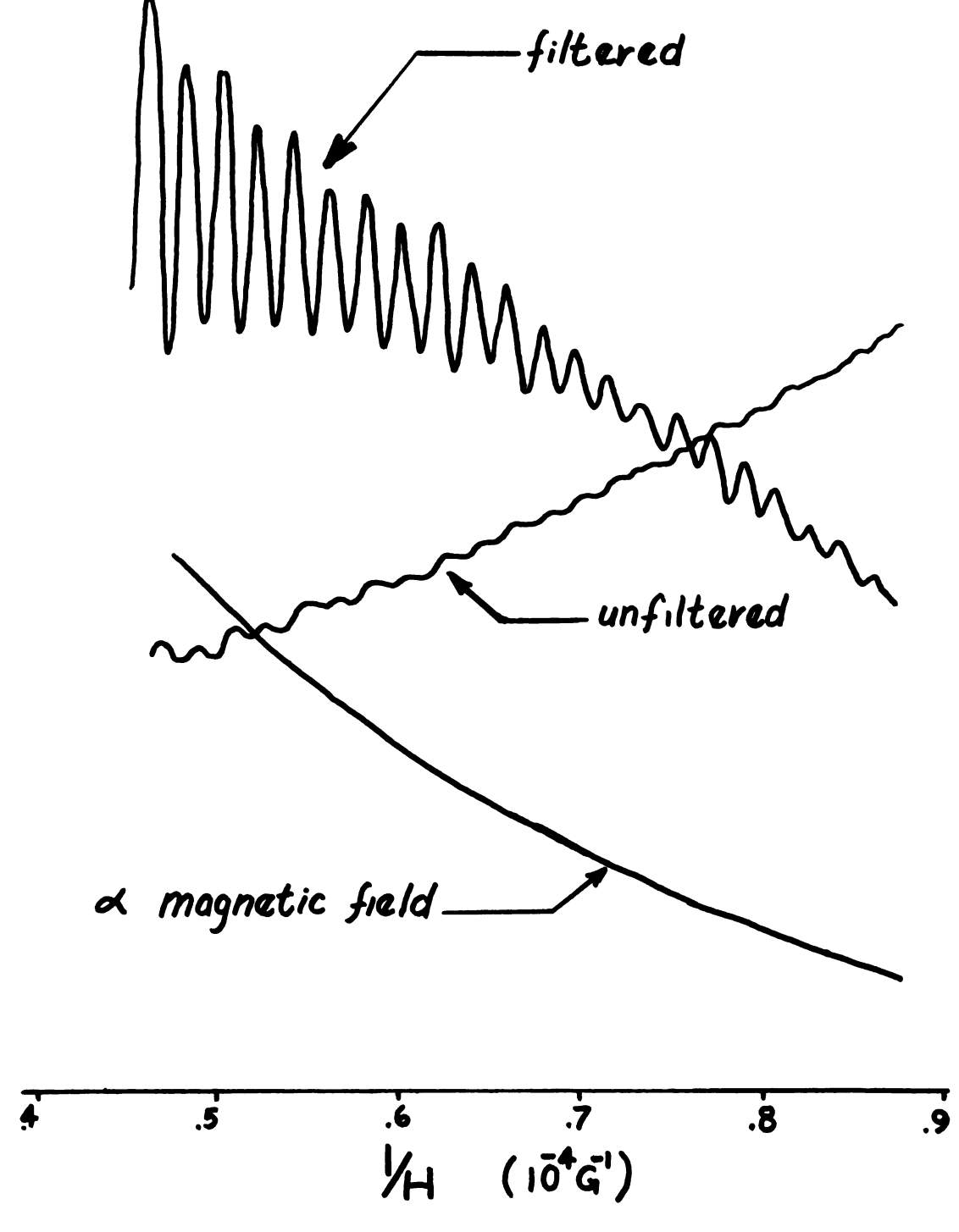


Fig. (H.2) Example of Application of Narrow Band Filter using 1/H Sweep

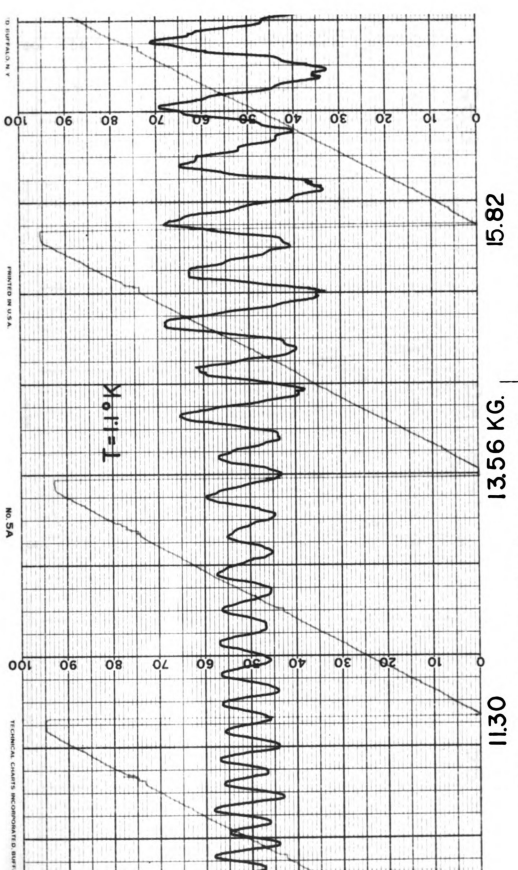


Fig. (H.3) Low Frequency Data . 700G/min %weep rate. Note the presence of the higher frequency at higher fields.

